

Washington University in St. Louis

Washington University Open Scholarship

All Theses and Dissertations (ETDs)

January 2009

A Framework for Temperature Imaging using the Change in Backscattered Ultrasonic Signals

Yuzheng Guo

Washington University in St. Louis

Follow this and additional works at: <https://openscholarship.wustl.edu/etd>

Recommended Citation

Guo, Yuzheng, "A Framework for Temperature Imaging using the Change in Backscattered Ultrasonic Signals" (2009). *All Theses and Dissertations (ETDs)*. 138.

<https://openscholarship.wustl.edu/etd/138>

This Dissertation is brought to you for free and open access by Washington University Open Scholarship. It has been accepted for inclusion in All Theses and Dissertations (ETDs) by an authorized administrator of Washington University Open Scholarship. For more information, please contact digital@wumail.wustl.edu.

WASHINGTON UNIVERSITY IN ST. LOUIS
School of Engineering and Applied Science
Department of Electrical and System Engineering

Thesis Examination Committee:
R. Martin Arthur, Chair
Jr-Shin Li
James G. Miller
Eduardo G. Moros
Joseph A. O'Sullivan
William L. Straube
Jason W. Trobaugh

A FRAMEWORK FOR TEMPERATURE IMAGING USING THE CHANGE IN
BACKSCATTERED ULTRASONIC SIGNALS

by

Yuzheng Guo

A dissertation presented to the School of Engineering
of Washington University in partial fulfillment of the
requirements for the degree of

DOCTOR OF PHILOSOPHY

December 2009
Saint Louis, Missouri

copyright by

Yuzheng Guo

2009

ABSTRACT OF THE THESIS

A Framework for Temperature Imaging using the Change in Backscattered
Ultrasonic Signals

by

Yuzheng Guo

Doctor of Philosophy in Electrical Engineering

Washington University in St. Louis, 2009

Research Advisor: Professor R. Martin Arthur

Background Hyperthermia is a cancer treatment that elevates tissue temperature to 40 to 44°C. It would benefit from a non-invasive, safe, inexpensive and convenient thermometry to monitor heating patterns. Ultrasound is a modality that meets these requirements. In our initial work, we proposed an approach to temperature imaging (TI) using the change in the backscattered energy (CBE). The agreement between predicted and measured CBE from *in-vitro* experiments showed that CBE is a potential parameter for TI. To date, CBE has been computed in a straightforward, but *ad hoc manner*. We developed and explored a mathematical representation for our approaches to TI to optimize temperature accuracy and spatial resolution.

Methods Non-thermal effects of noise and motion confound the use of CBE. Assuming additive white Gaussian noise, we looked at the dependence of CBE on SNR and applied signal averaging and thresholding to images from both simulations and experiments. Our motion compensation algorithms were also applied to simulated

images and images obtained in null experiments with known motion. The effects of interpolation methods and signal sampling rate on motion compensation were investigated. In the development of the framework, temperature imaging was modeled as a problem of estimating temperature from the random processes resulting from thermal changes in signals. CBE calculated as the ratio of energies was formalized as a ratio between two random variables. Mutual information (MI) was studied as an example of the parameters for temperature imaging based on the joint distribution of the two random variables in the ratio. Furthermore, a maximum likelihood estimator (MLE) was developed. The MI and MLE approaches were applied both to simulated images and to experimental data.

Results Results from both simulations and experiments showed that noise effects were reduced by signal averaging. The motion compensation algorithms proved to be able to compensate for motion in images and were improved by choosing appropriate interpolation methods and sample rates. For images of uniformly distributed scatterers, CBE and MI can be computed independent of SNR to improve the accuracy of temperature estimates. The application of MLE also showed improvements in temperature accuracy compared to the energy ratio from the signal mean in simulations. Their application to experimental data requires more work to implement noise reduction approaches in 3D heating experiments with current imaging instrumentation.

Conclusions The framework identified ways in which we were able to reduce the effects of both noise and motion. The framework formalized our approaches to temperature imaging, improved temperature accuracy in simulations, and can be applied to experimental data if the noise reduction approaches can be implemented for 3D experiments.

Acknowledgments

I'd like to take this opportunity to express my heartfelt gratitude to my advisor, Dr. R. Martin Arthur, for his guide toward the understanding of my study and research work, for his constant support throughout these years with great patience and consistent encouragement. I believe these will not only benefit to my current study but also my future career. I'd also like to express special thanks to Dr. Jason W. Trobaugh, who, like a brother and friend, gave me many important suggestions for my research. Additionally, thanks to Professor William L. Straube from the Department of Radiation Oncology in medical school who helped us a lot in the experiments.

It's lucky for me to study in the department of Electrical and Systems Engineering. The faculties, staffs and students are always helpful. I gratefully thank Dr. Joseph A. O'Sullivan for his valuable advices to broaden my view. I would also appreciate Dr. Heinz Michael Schaettler's great help on the mathematical work in my study.

Debomita Basu and Shuli Wang are very kind lab mates and friends of mine. I really enjoyed every moment of study with them here.

Finally, no words can express the appreciation to my parents and my wife, who are always there with me, keeping me calm down and confident all the time. Additionally, many thanks to my family members and my friends for their supports.

Yuzheng Guo

*Washington University in Saint Louis
December 2009*

Dedicated to my wife, Yiwen!
Dedicated to my parents!
Dedicated to all people that supported me!

Contents

Abstract	ii
Acknowledgments	iv
List of Tables	ix
List of Figures	x
1 Introduction	1
1.1 Non-invasive Thermometry for Hyperthermia	1
1.2 Objectives of the Dissertation	3
1.3 Organization of the Dissertation	4
2 Ultrasonic Thermometry	5
2.1 Ultrasound-Based Methods	6
2.2 Methods Based on Change in Backscattered Energy	7
2.3 Motion in Images	10
2.4 Statistic Models of Ultrasonic Signals	11
2.5 Significance	13
3 Improvement of CBE-based Temperature Imaging	14
3.1 Use of the Discrete-Scatterer-Model Simulation Tool for Ultrasonic Thermometry	15
3.2 Reduction of Spurious CBE due to Noise	16
3.2.1 CBE with SNR	16
3.2.2 Reduction of Noise via Signal Averaging and Thresholding	19
3.3 Reduction of Motion-induced Spurious CBE	22
3.3.1 Use of Motion Estimation Algorithms	22
3.3.2 Motion-induced CBE	23
3.3.3 Reduction of Motion-induced CBE	27
3.4 Summary and Conclusions	38
4 System for <i>In-vitro</i> 3D Image Acquisition	39
4.1 Specimen and Thermocouple Fixture	39
4.2 Uniform Heating of Tissue	40
4.3 Temperature Measurement	41
4.4 Image Acquisition	42

4.5	Transducer Positioning	44
4.6	Configuration of Heating Experiments	46
4.7	Null Experiments	46
5	Verification of Reduction in Spurious CBE Induced by Noise and Motion	47
5.1	Verification of Noise Reduction Method	47
5.1.1	Noise in Images of Real Tissue	47
5.1.2	Reduction of Noise-Induced Spurious CBE	50
5.2	Experimental Verification of Motion Compensation	60
5.2.1	Null Experiments with Motion	61
5.2.2	Motion Compensation and Spurious CBE Reduction	61
5.3	Summary and Conclusions	75
6	Framework for Temperature Imaging with CBE	77
6.1	Modeling the Problem of Temperature Imaging	78
6.1.1	Random Phasor Sum Model for Temperature Dependent Signals	78
6.1.2	Marginal and Joint Distributions of Ultrasonic Signals	80
6.2	Formalization of CBE Computation	90
6.2.1	CBE as a Ratio of Random Variables	90
6.2.2	Calculation of PCBE and NCBE using Backscattered Signals from Uniformly Distributed Scatterers	91
6.2.3	Temperature Imaging using CBE	95
6.3	Summary and Conclusions	103
7	Examples of Temperature Imaging Beyond the Energy Ratio	104
7.1	Temperature Imaging based on the Joint Distribution of Signals at Reference and Current Temperatures	105
7.1.1	Temperature Imaging using Mutual Information (MI)	105
7.1.2	Temperature Imaging using Cross Correlation	109
7.2	A Maximum Likelihood Estimator for Tissue Temperature	111
7.2.1	Envelope of the Image Difference	112
7.2.2	Maximum Likelihood Estimator	113
7.2.3	Factors Affecting the Performance of MLE	116
7.2.4	Temperature Imaging using MLE – Simulation Results	120
7.3	Summary and Conclusions	125
8	Investigation of Experimental Applications of the Framework	126
8.1	Computation of Mutual Information from the Data Histogram	127
8.2	Application of the Maximum Likelihood Estimator to Experimental Data	130
8.3	Summary and Conclusions	134
9	Conclusions and Future Work	136

9.1	Conclusions	136
9.2	Further Work on Noise and Motion Reduction	139
9.3	Further Development of the Framework	140
9.4	Dynamic Model	141
Appendix A Matlab Control Functions for the Terason 3000 Ultra- sonic Imaging System 144		
A.1	Matlab Control Functions using AutoIt	144
A.2	Matlab Control Functions using the Terason Software Developer's Kit (SDK)	145
Appendix B Distribution of the Ratio of Dependent Rayleigh Ran- dom Variables 149		
Appendix C Estimation of Correlation Parameter in the Joint Rayleigh Distribution 155		
Appendix D Dependence of the Ratio PDF on SNR 159		
Appendix E CBE Due to Motion-Induced De-correlation 162		
References 164		
Vita 174		

List of Tables

9.1 SNR for Temperature Accuracy of $\pm 0.5^{\circ}C$ 138

List of Figures

2.1	Predicted and measured CBE in initial works.	9
3.1	CBE with SNR from simulations	17
3.2	CBE with SNR from simulations with and without thresholding	18
3.3	B-mode image of turkey breast from the Terason 3000 system.	19
3.4	Increase of SNR with number of frames used in signal averaging.	20
3.5	CBE with SNR when known noise is added to the image.	21
3.6	Weak signals selected by different thresholds	21
3.7	Frames at various temperatures from TC111 before motion compensation	24
3.8	3D motion detected in experiment TC111	25
3.9	Frames at various temperatures from TC111 after motion compensation	26
3.10	CBE with rigid motion	27
3.11	CBE variation with correlation computed from the ratio distribution.	28
3.12	CBE with non-rigid motion	29
3.13	Motion detected in heating experiment TC111.	29
3.14	Error in motion estimation in simulations based on motion from TC111.	30
3.15	CBE before and after motion compensation with cubic interpolation .	30
3.16	residual spurious CBE with cubic interpolation	31
3.17	CBE before and after motion compensation with cubic interpolation without implementing temperature change	32
3.18	Effect of interpolation on image transformation	33
3.19	Effect of interpolation on image transformation with double the sample rate	33
3.20	residual spurious CBE with spline interpolation	34
3.21	Residual spurious CBE with double the axial sampling rate	35
3.22	residual spurious CBE with cubic interpolation axial up-sampling . .	36
3.23	residual spurious CBE with cubic interpolation and up-sampling in both directions	36
3.24	Error in motion estimation with cubic interpolation at SNR=23dB . .	37
3.25	residual spurious CBE at SNR=23 and 43dB	37
4.1	3D image acquisition system.	40
4.2	Calibration of the thermocouples	42
5.1	RF images of turkey breast	48
5.2	Histogram of an RF image of turkey breast	49

5.3	Difference between two RF images of turkey breast and its histogram	49
5.4	Temperature variation in NL002	51
5.5	Intra-loop CBE from single frames of NL002	51
5.6	SNR with frame averaging from NL002	53
5.7	CBE with frame averaging from NL002	53
5.8	CBE with SNR from NL002	54
5.9	Regions of tissue for CBE computation from NL002	55
5.10	CBE from strong signal region from NL002	55
5.11	CBE with SNR with thresholding from NL002	56
5.12	Inter-loop CBE from NL002	57
5.13	Difference of images within and between loops from NL002	58
5.14	Inter-loop CBE from NL004	59
5.15	Inter-loop CBE from null experiment with phantom	59
5.16	Images with motion from experiment NL012	62
5.17	Reference CBE in experiment NL012	63
5.18	Error in motion estimation from NL012 with cubic interpolation	64
5.19	Motion compensated images from NL012	65
5.20	CBE from NL012 with cubic interpolation	66
5.21	Error in motion estimation from NL012 with spline interpolation	66
5.22	CBE from NL012 with spline interpolation	67
5.23	Error in motion estimation from NL012 with axial up-sampling	68
5.24	CBE from NL012 with axial up-sampling	68
5.25	Error in motion estimation from NL012 with up-sampling in both directions	69
5.26	CBE from NL012 with up-sampling in both directions	69
5.27	Error in motion estimation from averaged frames of NL012 with cubic interpolation	70
5.28	Residual spurious CBE from averaged frames of NL012 with cubic interpolation.	71
5.29	Residual spurious CBE from averaged frames of NL012 with spline interpolation.	71
5.30	Residual spurious CBE from averaged frames of NL012 with axial up-sampling.	72
5.31	Residual spurious CBE from averaged frames of NL012 with up-sampling in both directions.	72
5.32	Error in motion estimation from NL012 with cubic interpolation at $37^{\circ}C$	73
5.33	CBE from NL012 with cubic interpolation at $37^{\circ}C$	74
5.34	Error in motion estimation for NL012 with up-sampling in both directions at $37^{\circ}C$	74
5.35	CBE in experiment NL012 with spline interpolation at $37^{\circ}C$	75
5.36	CBE in experiment NL012 with up-sampling in axial at $37^{\circ}C$	76
5.37	CBE in experiment NL012 with up-sampling in both directions at $37^{\circ}C$	76

6.1	Histogram and fitted Gaussian for RF image of tissue	84
6.2	Histogram and fitted Laplace for RF image of tissue	84
6.3	Histogram and fitted distributions for B-scans of tissue	86
6.4	Simulated B-scans of non-uniformly distributed scatterers	87
6.5	Distributions of a simulated RF image of non-uniformly distributed scatterers	87
6.6	Distributions of simulated B-scans of non-uniformly distributed scatterers	88
6.7	Distribution of non-identical Gaussian RV's	89
6.8	Distribution of non-identical Rayleigh RV's	89
6.9	CBE with SNR from simulations	93
6.10	CBE from simulated images at SNR = 17dB	94
6.11	CBE from simulated images at SNR = 29dB	95
6.12	Error in temperature estimation using PCBE at SNR of 17dB.	96
6.13	Error in temperature estimation using PCBE at SNR of 29dB.	97
6.14	Error in temperature estimation using NCBE at SNR of 17dB.	97
6.15	Error in temperature estimation using NCBE at SNR of 29dB.	98
6.16	Temperature estimation using PCBE with varied SNR in calibration and estimation	99
6.17	Temperature estimation using NCBE with varied SNR in calibration and estimation	99
6.18	CBE curves with different reference temperatures	100
6.19	Standard deviation of CBE from simulations at SNR of 29dB	101
6.20	Standard deviation of CBE from simulations at SNR of 17dB	101
6.21	Temperature estimation using CBE STD at SNR of 17dB	102
6.22	Temperature estimation using CBE STD at SNR of 29dB	102
7.1	Ratio PDF and joint distribution of Simulated B-scans	106
7.2	MI of simulated RF images at various SNRs	108
7.3	Error in temperature estimation using MI	109
7.4	Correlation coefficients of simulated RF images at various SNRs.	110
7.5	Error in temperature estimation using correlation coefficient	110
7.6	Correlation coefficient of squared B-scans	111
7.7	Envelopes of simulated difference RF images at various temperatures	121
7.8	Error in temperature estimation using MLE at various SNRs	122
7.9	Error in temperature estimation using MLE at two scatterer proportions	123
7.10	Error in temperature estimation using MLE at two image sizes	123
7.11	Error in temperature estimation using MLE with calibration for bias	124
8.1	Mutual information computed from experimental data.	128
8.2	Mutual information computed from simulated B-scans at various SNRs	129
8.3	Mutual information with different bin widths of histograms from sim- ulations	130

8.4	Temperature estimation error in simulations at various SNRs using GG based MLE	132
8.5	Error in temperature estimation for 3D experiments using MLE . . .	133

Chapter 1

Introduction

1.1 Non-invasive Thermometry for Hyperthermia

The interest in thermal therapies, such as hyperthermia and high intensity focused ultrasound (HIFU), is growing in recent years. Hyperthermia is a treatment for tumor which increases tissue temperature to 40 to 43°C [107]. It was also employed as an adjunct treatment with traditional therapies, such as chemotherapy and radiotherapy, to improve their performance [72, 68, 104]. During the hyperthermia treatment, it is desired to deliver adequate heat to the target and keep normal tissue intact. It is, however, difficult to control the heat delivery without enough information of tissue temperature, because of the variation of the tissue properties and the diffusion [63, 28]. Temperature is currently measured invasively at sparse locations using thermocouples, which does not provide continuous thermal distribution in tissue volumes [103].

In order to guide the delivery of the heat to the tumors, an accurate, non-invasive, convenient, economical and safe thermometry is desired. Various non-invasive thermometries have been developed based on electrical impedance tomography (EIT), microwave, magnetic resonance imaging (MRI) and ultrasound. Among these modalities, EIT based method is able to detect high temperature change, but is not accurate enough in the hyperthermia range [78, 73]. Microwave radiometry type of methods do not have good spatial resolution when applied to deep targets [78, 64]. MRI based method is popular due to its good temperature accuracy and spatial resolution [63, 28]. It is however constrained by its high cost[78], and the difficulty in cooperation with heating instruments. Comparing to other methods, ultrasound is a safe, cheap and convenient modality.

Heating tissue leads to changes in the backscattered signals because of the temperature dependence of speed of sound (SOS), attenuation, and backscatter properties of the tissue [4]. Several parameters have been used in ultrasound based thermometries including attenuation, echo shift due to the change in SOS and the tissue thermal expansion, and the change in backscattered energy (CBE). It is found that attenuation does not change significantly in the hyperthermia range [4]. Estimating temperature from echo shift requires prior knowledge of the temperature dependence on the change in SOS and tissue thermal expansion [93, 87, 74, 108, 47]. In addition, tissue motion may lead to loss of the tracking of the echo shift [93]. Our group developed a method using the change in backscattered energy.

Our long term goal is to develop a method to measure 3D temperature distribution within 0.5°C in 1 cm^3 volumes using backscattered ultrasonic signals [4]. In an initial investigation, Straube and Arthur developed a theoretical CBE model for single scatterers by normalizing the backscattered power relative to the power reflected at the reference temperature [85, 92]. It approximated the CBE for single scatters as ratio between the backscatter coefficients at current and reference temperatures. Using this model, Arthur etc predicted that CBE may increase or decrease monotonically with temperature depending on scatterer type, denoted by positive CBE (PCBE) and negative CBE (NCBE), respectively [92]. In later 1D and 2D experimental studies with various types of tissue, CBE was computed as a ratio between images at current and reference images [3, 7]. Monotonic variation of the measured PCBE and NCBE with temperature confirmed the theoretical predictions [3, 7]. These initial results demonstrated the temperature dependence of CBE and supported our idea of developing CBE based non-invasive thermometry for hyperthermia.

Although the results in our initial work showed that CBE is a potential parameter for temperature imaging, our approach is not formalized. To date, computation and characterization of CBE are straight forward, but somewhat ad hoc. It is desired to develop and exploit a mathematical representation for our approaches to temperature imaging to optimize temperature accuracy and spatial resolution. We would also pursue other possible approaches than estimating temperature directly from the energy ratio. These works may form a framework for temperature imaging using the change in backscattered signals. For simplicity, this first framework for TI considered only thermal changes in the signals. To apply it to experimental data, non-thermal

effects in signals, such as that caused by noise and motion in the images, should be reduced.

In our initial work, it was found that noise and motion in images led to spurious CBE, which caused estimation error. A study using the simulation tool showed that the slope of the CBE curves changed with noise level in the images [103]. We, however, do not know how spurious CBE depends on signal to noise ratio (SNR) and if SNR in images can be increased with current experimental setup. Similarly, we had no information of how much spurious CBE may be caused by motion. Previously, the apparent motion in images has been tracked and compensated for 2D images [7]. However, without the knowledge of the true motion and true CBE, we were not able to evaluate how well the motion was compensated, how much spurious CBE was left, and what are factors affecting spurious CBE reduction. Noise and motion are common problems in temperature imaging. Application of the framework could also be affected by noise and motion. We investigated, in this work, the approaches to reducing the effects of noise and motion.

Our long term goal of measuring 3D temperature distribution within 0.5°C in 1 cm^3 requires us to be able to acquire 3D images. This capability is also necessary for 3D motion compensation. In this study, we will build a 3D imaging system for heating experiments.

1.2 Objectives of the Dissertation

To our knowledge, there is no framework exists for temperature imaging using the change in backscattered signals. The work in this dissertation is the first step of developing such a framework, and may be an important step towards the systematization of temperature imaging using CBE. The objectives of this study are listed below.

1) To create a framework for temperature estimation with CBE. Here we 1) model temperature imaging via a probabilistic framework, 2) formalize computational methods for CBE, 3) develop procedures for precise computation of CBE and accurate estimation of temperature, and 4) employ approaches using changes in the backscattered signals other than the energy ratio.

2) To Construct a 3D imaging platform for measuring CBE in heating experiments. The capability of acquiring 3D data is important, since our goal is to develop temperature estimator for 1cm^3 volumes, and it would enable us to correct for out-of-plane motion in the images. We will build the platform to: a) keep temperature drifting $< \pm 0.1^\circ\text{C}$ and maintain thermo-equilibrium within the tissue during data acquisition, b) reduce physical motion of the tissue and the thermocouples.

3) To Improve the CBE based temperature imaging by

a) Investigating the dependence of spurious CBE on SNR and approaches to noise reduction by signal averaging using simulation tool,

b) Investigating the dependence of spurious CBE on motion, evaluating the motion compensation algorithms, and studying factors affecting motion compensation.

4) To Verify the methods developed in Aim 3 for experimental data. a) Verify the dependence of spurious CBE on SNR and noise reduction using loops of tissue images acquired in null experiments (no temperature change). b) Conduct null experiments and add known motion in images. Evaluate the performance of the motion compensation algorithms and the factors affecting the performance as in Aim 3.

1.3 Organization of the Dissertation

Chapter 2 introduces the background of this work. Chapter 3 presents approaches to reducing noise and motion effects for improving CBE based temperature imaging. Chapter 4 introduce the development of our 3D heating experiment system. Then, the approaches proposed in chapter 3 are verified using experimental data in Chapter 5. In Chapter 6, we model the temperature imaging problem and develop mathematical representation for our CBE based approaches to temperature imaging. Applications of the mutual information and a maximum likelihood estimator for temperature imagin are investigated in Chapter 7. Feasibility of applying the framework to experimental data is discussed in Chapter 8. Chapter 9 concludes the work.

Chapter 2

Ultrasonic Thermometry

Thermal therapies, such as hyperthermia and high intensity focused ultrasound (HIFU), have attracted more interests in recent years. Hyperthermia is a tumor treatment which increases tissue temperature to 40 to 43°C, which is cytotoxic to tumor cells due to the lack of blood perfusion [107]. It also improved, when combined with chemotherapy and radiotherapy, the performance of traditional treatments [72, 68, 104]. Tumor temperature and treatment time are two important factors affecting the therapy performance[68]. Therefore, a precise feedback of temperature distribution in tissue is important for therapy control, such that enough heat can be delivered to tumor while normal tissue is protected.

Tissue temperature is, however, currently measured invasively at sparse locations. Practical clinic application of hyperthermia requires non-invasive, accurate, safe and convenient thermometry. Researchers have proposed techniques using MRI [43, 19, 42], electrical impedance tomography (EIT)[73], microwave radiometry[64] and ultrasound. Although MRI based method has been proven to meet required temperature accuracy and spatial resolution [28, 63], it is limited by its high cost and the difficulty of being compatible with the heating equipments [78, 1, 65]. EIT method does not have enough for temperature resolution[78]. Microwave radiometry type of methods does not have good spatial resolution when applied to deep target[78].

2.1 Ultrasound-Based Methods

Comparing to other approaches, ultrasound based methods are low-cost, portable and safe with required temperature accuracy and spatial resolution and simple signal processing [87, 1]. The ultrasound based thermometry can be ranged into three types [4]: (1) those based on the acoustic attenuation, (2) those based on echo shift due to the change in the speed of sound (SOS) and the thermal expansion in tissue, (3) those based on the change in the backscattered energy (CBE). These methods make use of the change in the backscattered signals caused by the thermal effect on attenuation, SOS and the backscatter properties of the tissue [4].

Ultrasonic attenuation was reported to change with temperature. Damianou et al studied the temperature dependence of ultrasonic attenuation in dog tissue over the range from room temperature to 70°C [25]. Their result showed a significant change in attenuation when temperature was above 50°C and reached the maximum at 65°C. Similar results were found for human prostate at discrete temperature levels [113]. It was also found that ultrasonic attenuation, measured at room temperature, changed obviously before and after heating [23, 96]. Some researchers reported significant changes in attenuation coefficient during 22 to 37°C [66, 98]. The change in attenuation also varied with treatment duration and tissue type [106]. Straube and Arthur found that the attenuation had little effect on backscattered energy over the hyperthermia range [4].

The speed of sound has been studied as a primary temperature dependent ultrasound parameter [4, 11, 37, 65, 46, 70]. It was found to vary monotonically with temperature depending on the tissue type [18, 76, 9]. Methods for measuring SOS can be categorized as transmission based and pulse-echo based approaches [71]. They required complicated implementation to achieve adequate accuracy [71, 58], such as a good access from wide angles, or an identifiable target in the tissue, or usage of cross-beam [71]. In addition, the change in SOS in some medium are not significant for temperature estimation [65]. These difficulties might be the reasons for SOS not being used for temperature estimation in clinics.

Thermal effects, such as the change in SOS and tissue thermal expansion, lead to displacement between the backscattered signals [4, 61, 77]. Seip and Ebbini introduced a frequency domain technique to estimate temperature using the change in the resonance frequency, which was assumed to be proportional to the average scatterer spacing and vary linearly with temperature [77]. The power spectrum density (PSD) was estimated by an auto-regressive (AR) model, whose order is difficult to be determined [87]. Amini et al improved the estimation of the resonance shift using a high-resolution spectral analysis technique [1].

Seip et al, then, proposed a time domain approach, which assumed that the echo shift depends on the change in temperature nearly linearly [78, 79]. In a study of temperature estimation for HIFU, Maass-Moreno and coworkers considered both the change in SOS and the thermal expansion in tissue and modeled the echo shift as an approximate linear function of the temperature [61, 62, 60]. They found that the effect of thermal expansion is small. It may be ignored in the range of hyperthermia [2, 22]. The feasibility of echo shift based method was demonstrated in experiments with gel phantom and *in-vitro* bovine liver in two-dimension [87, 86, 74], and with phantom in three dimensions [2]. Temperature was also estimated during *in-vivo* radiofrequency ablation (AFR) [108]. Sun and Ying pointed out that echo shift based methods required prior knowledge of the temperature dependence of the change in SOS and of the thermal expansion coefficients in tissue [93]. For accurate measurement of temperature distribution, these parameters need to be estimated from calibrations [87, 74, 108, 47]. Another difficulty was caused by the tissue motion during the heating, which may lead to the loss of the tracks of echoes [93].

Our method belongs to the third type, which makes use of the temperature dependence of the backscatter properties of the tissue. Details will be presented below.

2.2 Methods Based on Change in Backscattered Energy

Our approach for temperature estimation uses the change in the backscattered energy. Straube and Arthur developed a theoretical model for the CBE from individual

scatterers [92]. They normalized the backscattered power [85] from tissue with respect to the power at a reference temperature and thus eliminated parameters that do not depend on temperature. The backscattered power can be expressed as [85]

$$P_r(T) = \frac{2H^2\delta}{8R^4\alpha(T)}\eta(T)S(1 - e^{-2\alpha(T)c(T)\tau}) \times \left[\frac{e^{\alpha(T)c(T)\delta} - e^{-\alpha(T)c(T)\delta}}{2\alpha(T)c(T)\delta} \right] , \quad (2.1)$$

where H/R and δ are the amplitude and duration of the insonifying sinusoidal burst, respectively [92]; R is the distance between the tissue and the transducer; α is the attenuation; $c(T)$ is the speed of the sound and $\eta(T)$ is the backscattered coefficient.

The normalized backscattered power, i.e., the change in the backscattered power was approximated as a ratio between backscatter coefficients at current temperature, T , and a reference temperature, T_0 . Since we usually compute the energy of a signal, the change in the backscattered power, i.e., the energy per unit time, is denoted as the change in backscattered energy, the CBE. The backscatter coefficient was assumed to be proportional to the scattering cross section of a subwavelength scatterer. According to this model, the temperature dependence of CBE is approximately due to the change in SOS and the change in the density of the scatterers and the medium [92]

$$\begin{aligned} CBE(T) &= [\alpha(T_0)/\alpha(T)][\eta(T)/\eta(T_0)] \frac{1 - e^{-2\alpha(T)x}}{1 - e^{-2\alpha(T_0)x}} \\ &\cong \eta(T)/\eta(T_0) \\ &= \frac{\left(\frac{\rho_m c(T)_m^2 - \rho_s c(T)_s^2}{\rho_s c(T)_s^2}\right)^2 + \frac{1}{3}\left(\frac{3\rho_s - 3\rho_m}{2\rho_s + \rho_m}\right)^2}{\left(\frac{\rho_m c(T_0)_m^2 - \rho_s c(T_0)_s^2}{\rho_s c(T_0)_s^2}\right)^2 + \frac{1}{3}\left(\frac{3\rho_s - 3\rho_m}{2\rho_s + \rho_m}\right)^2} , \end{aligned} \quad (2.2)$$

where ρ_m and ρ_s are density of the medium and scatter respectively, x the the length of the tissue. Using this model, we predicted that CBE may increase or decrease with temperature, depending on the type of scatterers. The increase and decrease in CBE, denoted by positive and negative CBE, respectively, are shown in the left plot of Fig.2.1.

In their 1D study, Arthur and coworkers measured CBE with temperature from specimens of bovine liver, turkey breast, and pork muscle [3]. Measured CBE varied almost monotonically with temperature as predicted by the above model. In a subsequent study, Arthur et al made 2D measurements of CBE from the same types of tissue

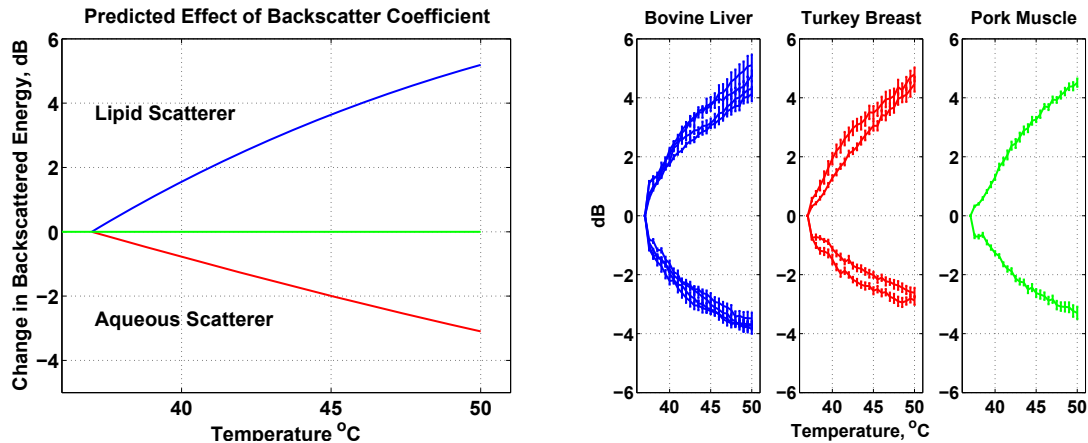


Figure 2.1: (Left) Predicted CBE for single sub-wavelength lipid and aqueous scatterers in an aqueous medium. (Right) Means of measured CBE in positive and negative regions of images in four specimens of bovine liver, two of turkey breast, and one of pork muscle.

specimens during *in-vitro* heating experiments [7]. CBE was calculated by taking ratio at each pixel between images at each temperature and the reference. Positive CBE (PCBE) was computed as mean of ratios larger than 1 and negative CBE (NCBE) as mean of ratios less than 1. Variation of PCBE and NCBE were consistent with the results of the prediction and the 1D study. These results confirmed the temperature dependence of CBE and supported the idea of using CBE as a parameter for temperature imaging.

Although there is no need for prior knowledge of tissue property and the change in SOS with temperature [3], CBE needs to be calibrated to infer temperature [4]. This calibration and thus CBE based temperature imaging are, however, limited by the dependence of CBE on non-thermal factors, such as the noise and the motion in the images [4, 103]. In a study using simulation tool, Trobaugh et al found that the slope of CBE curves varied with signal to noise ratio (SNR). The variation of CBE slope with SNR may impose difficulty in calibrating CBE. In this work, we studied the dependence of the spurious CBE on SNR and motion.

2.3 Motion in Images

The dependence of CBE on motion, is a limitation of CBE based method [4]. It is also a common problem in other temperature imaging approaches [5, 41, 30, 44, 94, 27].

Various techniques have been developed for tracking motion in ultrasonic images. Doppler based technique was popular in assessing tissue motion, especially for the blood flow measurement [41]. Kasai et al estimated the mean Doppler frequency shift using the autocorrelation method for measuring blood flow velocity [48]. Loupas et al improved this method by evaluating both mean Doppler frequency and RF center frequency[57]. Doppler based methods, however, require the tissue in motion during data acquisition [41] and has difficulty in measuring lateral velocity due to its angle dependence [111, 12, 95].

Time domain cross correlation based methods started to be widely used around mid 1980's to early 1990's [34, 36, 33, 15, 39, 40]. Underlining principle of cross correlation based methods lies in the fact that, the echo shift or time delay can be determined by the peak location of the cross correlation function between two successively received signals. The peak usually falls between the grid due to sub-sample motion. Location of true peak can be found by up-sampling the signal with intensive computation load [30, 59], or fitting the curve near the peak of the discrete cross correlation function [41, 36, 54, 56]. Motion in axial direction can also be estimated by examining the phase information of the complex cross correlation between two analytical signals [57, 59]. Chen et.al extended this approach for lateral motion estimation by introducing a synthetic phase in lateral [21]. Ferrara et al proposed a maximum likelihood estimator for blood velocity considering the shifts in both time and frequency domain[35].

Non-rigid motion leads to signal de-correlation [114, 55]. Kybic and Unser modeled non-rigid motion using B-spline functions [53]. Motion in the images was then detected by finding the optimal estimation of the B-spline parameters that minimized the sum of squared difference (SSD) between two images. Ledesma-Carbayo et al used this method for estimating motion in 2D echo-cardiography images [55].

As introduced above, motion, or echo shift, was used for temperature inference. However, when tissue motion occurred, we may loss the track of thermal induced echo

shift. Therefore, in our study, instead of estimating temperature from echo shift, we compensated the motion in images such that CBE can be computed at each pixel over the whole image. This enabled us to use statistical properties of CBE and improve the temperature accuracy.

In our 1D study, strong scattering regions were manually isolated and CBE were measured from the selected scattering sites [3]. In the 2D study, the apparent motion was tracked and compensated by a block-matching approach. For each region, 2D motion was estimated by maximizing the cross correlation between RF signals at successive temperatures [7] and was accumulated relative to the reference image. Shifted images were then transformed by the estimated motion [7]. This method was successful for rigid motion in small regions. Later on, our group developed an algorithm for estimating and compensating non-rigid motion over large regions. The motion field was modeled to vary linearly over the region of interest and represented as a linear function of the motion at the control points chosen as the points at the corners of the region. Motion was estimated by searching the displacements at the control points that maximizes the cross correlation of two images. For a sequence of images obtained in experiments, motion was estimated for adjacent images using the optimization functions in MATLAB and accumulated to the reference. We, however, were not able to evaluate the performance of the motion compensation, since the true motion and true CBE were unknown. We also had no information about the motion dependence of CBE. More studies are desired and rely on the simulation platform.

2.4 Statistic Models of Ultrasonic Signals

To our knowledge, no work has been done for temperature imaging based on statistical models of ultrasound images. We believe that thermal change in backscattered ultrasonic signals must lead to changes in their statistical model. These models may enable us to describe our problem in a mathematical form and to create a framework for temperature imaging using the change in backscattered signals.

Various statistic models of ultrasound B-scans have been developed for tissue characterization. These models made use of the complex representation the backscattered

ultrasonic signals [110]. When the scatterers are uniformly distributed with high concentration, the backscattered signals contain fully-developed speckles [110]. Under this situation, the number of phasors in the complex representation is large and the phases of the element phasors are uniformly distributed between 0 and 2π . According to the central limit theorem, the real and imaginary components of the complex model can be represented, approximately, by independent Gaussian random variables with zero mean and the same variance. The envelope of the complex representation follows Rayleigh distribution [110, 10].

When the backscattered signals contain specular echoes from periodically distributed scatterers or isolated strong scatterers, the real and imaginary components of the complex representation can be modeled as Gaussian random variables with different means [109, 105]. Then, B-scan signals are known as post-Rayleigh and can be described by Rician or generalized Rician distribution which encompasses Rayleigh distribution [109, 105, 81].

The Gaussian assumption does not hold when: 1) the scattering cross sections vary widely or scatterers are not uniformly distributed although the scatterers number is large [69, 84, 80, 67]; 2) the scatterer population is low such that the resolution cell of the transducer contains limited number of scatterers [69, 112, 84, 29]. Signal under these conditions were modeled by the K distribution. It was generalized to more complicated Homodyned K distribution to handle more general scattering situation including periodically distributed scatterers [80, 29].

Shankar proposed a model based on Nakagami distribution for ultrasound B-scans to account for more general scattering conditions [81, 82, 83]. Comparing to the K distribution, parameters of Nakagami distribution can be easily estimated from the moments of the envelope signals. A generalized Nakagami model was then proposed including an additional parameter to Nakagami distribution for better fit to observed data histograms [82]. It was in fact equivalent to the generalized Gamma distribution [82, 90]. Recently, Eltoft proposed a Rician inverse Gaussian (RiIG) distribution for envelope-detected images based on similar physical motivation to that of the K distribution [31, 32]. The real and imaginary components of the complex representation were considered to be normal inverse Gaussian(NIG). The RiIG model has four parameters which provides more flexibility to fit the data histograms.

2.5 Significance

Our initial work has confirmed temperature dependence of CBE, which encouraged the usage of CBE for temperature imaging. Our approaches may, however, be limited by CBE dependence on non-thermal changes in the signals, e.g., those caused by noise and motion. Reduction of non-thermal effects in signals, i.e., spurious CBE, is significant for accurate temperature imaging. Furthermore, ultrasonic backscattered signals are random signals, whose statistical properties are affected by thermal change in the signals. Therefore, modeling temperature imaging via a probabilistic framework will make us be able to investigate our problem using more developed tools in signal processing. These tools could help us not only pursuing approaches for estimating temperature but also see the insight of the problem. We could also benefit from the framework in handling non-thermal effects, e.g., computing CBE independent of SNR. On the other hand, when the effects of noise and motion can be handled, we can assume that only thermal changes exist in signals. This assumption makes the development of the framework easier, during which only thermal effects are considered. In other words, the reduction of noise and motion effects and the framework can benefit each other. In addition, estimating temperature using CBE as a ratio suggested by Eq.2.2 is only one attempt to temperature imaging, which may not be the optimal one. We believe building a framework could help us to seek approaches other than the energy ratio and finally find an optimal thermometry for hyperthermia.

Chapter 3

Improvement of CBE-based Temperature Imaging

As claimed in the first chapter, the main objective of this work was to create a framework for temperature imaging using change in the backscattered signals. For temperature imaging using CBE, it is desired that changes in backscattered signals depend only on temperature. The framework developed in this work was based on this assumption. Hence, before starting this framework, we will first evaluate the reduction of non-thermal signal changes, such as that caused by noise or motion, in backscattered ultrasonic signals, which was found to impact CBE measurement and may impact the framework. CBE based temperature imaging can be improved by limiting these non-thermal effects. In addition, reduction of these non-thermal effects will also make our further development of the framework easier. For example, if signal change due to motion after compensation is much less than the thermal effect, we may ignore the impact of motion in the development of the framework.

In our initial work, it was found that the slope of CBE curves changed with noise level, i.e. signal to noise ratio (SNR) [103]. We also observed a "jump" at $37.5^{\circ}C$ in CBE curves computed from experiment data [7]. In this chapter, we investigate how CBE varies with SNR and approaches to reducing noise by signal averaging and thresholding. Noise reduction was performed on simulated images and real tissue image corrupted by known noise.

Motion in images, due to the change in speed of sound or tissue movement, also leads to spurious CBE [3, 7]. Dr. Trobaugh in our group developed a correlation based algorithm to correct the apparent motion in the images, which was extended

for 3D images. In this chapter, using the simulation tools, we also investigate how large the spurious CBE may be caused by motion and what factors may influence the performance of our motion compensation algorithm.

3.1 Use of the Discrete-Scatterer-Model Simulation Tool for Ultrasonic Thermometry

To study the effect of noise and motion on CBE, it is necessary to have knowledge of noise level and true motion. This information can not be obtained easily from experimental data. In this study, we rely on the simulation tool described in [103], which is based on a linear physical model for image formation and a discrete tissue model. The image formation was represented as a convolution of the imaging system point spread function (PSF) and the tissue model [103]

$$|i(\mathbf{r}, T)| = |h(\mathbf{r}) * q(\mathbf{r}, T)| \quad (3.1)$$

where $i(\mathbf{r}, T)$ is the complex representation of the temperature dependent RF image, $h(\mathbf{r})$ is the PSF of the imaging system, and $q(\mathbf{r}, T)$ is the reflectivity of the tissue, which was represented as a discrete model

$$q(\mathbf{r}, T) = \sum_{k=1}^{N_r} q_i(T) \delta(\mathbf{r} - \mathbf{r}_i) \quad , \quad (3.2)$$

where $q_i(T)$ is the reflectivity and \mathbf{r}_i is the position of the i^{th} scatterer.

Simulations follow the approach as described in [101, 102]. The system point-spread function (PSF) is assumed to be a spatially-invariant Gaussian pulse with 7M Hz center frequency, 0.2mm and 1mm full-width half-maximum beam width in axial and lateral respectively. Scatterers were uniformly distributed unless noted otherwise.

Baseline values of SNR, image size and population were 29dB, $1 \times 3cm^2$ and 2:1 N_a/N_l ratio, where N_a and N_l are the numbers of aqueous and lipid scatterers, respectively. The scatterers were uniformly distributed over the image region. Images at various SNR's were generated by adding Gaussian noise at different levels to simulated tissue

image. Motion in images was implemented by changing the location of the scatterers. Rigid motion was implemented by moving all scatterers in the same direction by the same distance. Non-rigid motion was implemented by changing scatterer position by a distance linearly dependent on the scatterer's initial positions.

3.2 Reduction of Spurious CBE due to Noise

3.2.1 CBE with SNR

In this work, noise was assumed to be Gaussian with zero mean additive to the RF images. Suppose s_1 and s_2 are acquired RF images of the same tissue sample with noise in two captures, then they can be represented as

$$s_1 = i_{rf} + n_1 \quad , \quad (3.3)$$

$$s_2 = i_{rf} + n_2 \quad , \quad (3.4)$$

where i_{rf} is the RF signal backscattered from the tissue, n_1 and n_2 are the noise in the signals.

To illustrate variation of CBE with SNR, images of uniformly distributed scatterers were simulated at SNR's ranging from $15dB$ to $45dB$ at $1dB$ intervals, covering the observed SNRs of experimental data. At each SNR, a tissue image without noise was first created, then two noise images were generated at same level and added to the tissue image. Ratio of the two resulting noisy images was computed and PCBE & NCBE were calculated as the mean of ratio values larger than and less than one, respectively. Twenty five trials were generated for all SNR's. CBE curves from both methods are plotted in Fig.3.1.

In the following chapters, the signal ratio is considered as the ratio between random variables. The ratio distribution can be computed analytically for signals from uniformly distributed scatterers, which was assumed in the simulations. In this case, we can show the dependence of the ratio distribution and thus CBE on SNR theoretically,

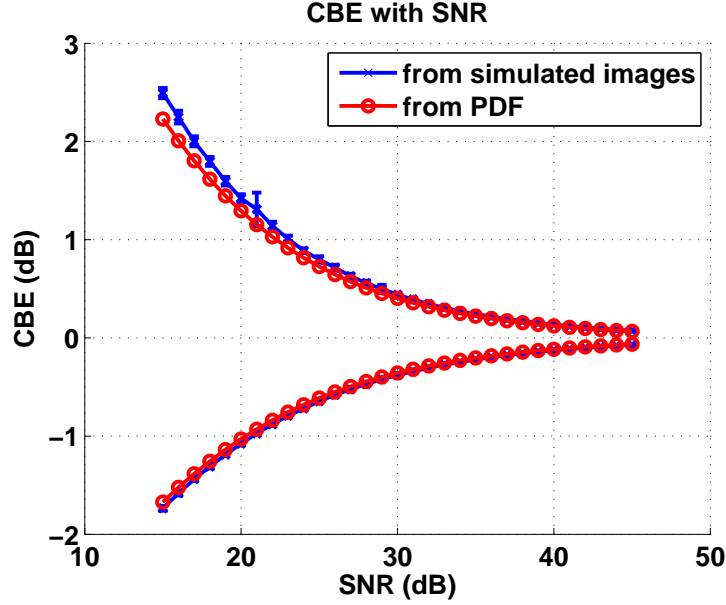


Figure 3.1: CBE computed using the ratio PDF and from simulated images at various SNRs.

when signal change is caused only by noise:

$$f_Z(z) = \frac{2 \frac{(\mu_1+1)(\mu_2+1)}{\mu_1\mu_2} \left(1 - \frac{\mu_1\mu_2}{(\mu_1+1)(\mu_2+1)}\right) \left(\frac{\mu_2+1}{\mu_2} + \frac{\mu_1+1}{\mu_1} z^2\right) z}{\left[\left(\frac{\mu_2+1}{\mu_2} + \frac{\mu_1+1}{\mu_1} z^2\right)^2 - 4z^2\right]^{\frac{3}{2}}}, \quad (3.5)$$

where z represents the ratio, $f_Z(z)$ is the probability density function of z , μ_1 and μ_2 represent signal to noise ratio of s_1 and s_2 , respectively. Details of the derivation of this result can be found in Appendix D. CBE with SNR was predicted using the above equation and plotted in Fig.3.1. It can be seen that CBE curves from simulated images and the prediction are close to each other. Both curves decrease monotonically to $0.1 \sim 0.15dB$ for an SNR of $45dB$.

Removal of Outliers in the Ratio

In Fig.3.1, PCBE from simulated images is slightly larger than the theoretical result from PDF when SNR is less than $25dB$. This outcome occurs because the influence of noise is greater on weak signals and produces "outliers" in the ratio computation. In order to remove the "outliers", we developed a thresholding strategy. In the reference

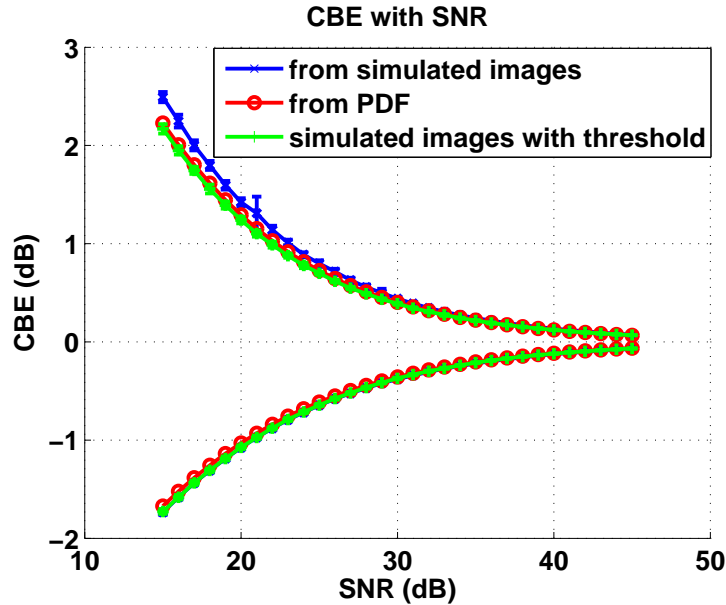


Figure 3.2: CBE with SNR computed using the ratio PDF and from simulated images with and without thresholding.

envelope image, pixels with value below given threshold are regarded as weak signals and ignored in the ratio computation. The threshold is determined according to the mode of the image histogram, the value which occurs most frequently. Here, the threshold was chosen to be $21dB$ below the mode. At this threshold value, CBE curves from simulated images match the CBE curves based on the theoretical prediction as seen in Fig. 3.2.

When "weak signals" are removed by thresholding, CBE curves from simulated images are consistent with the theoretical result. It is worth noting that "thresholding" is an *ad hoc* method because the determination of the threshold was done by trial and error. From the above figures, we see that the "outlier" effect is small when SNR is large. Since noise is assumed to be additive white Gaussian noise, SNR can be increased by signal averaging. Signal averaging and thresholding are discussed further in the following sections.

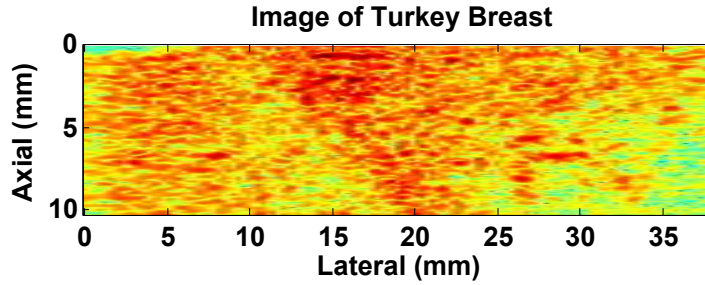


Figure 3.3: B-mode image of turkey breast from the Terason 3000 system.

3.2.2 Reduction of Noise via Signal Averaging and Thresholding

In order to demonstrate the increase of SNR and thus decrease of spurious CBE by signal averaging, we added known noise to an image of turkey breast, which was considered as the "true signal", i.e., the signal without noise. Fig.3.3 shows an image of the tissue sample.

In Chapter 5, noise effects are reduced by averaging frames in a loop obtained by the Terason 3000 ultrasonic imaging system, described in Chapter 4. The typical number of frames in a Terason loop is 156 for our experiments. To be consistent with our experiments, the procedure for adding noise was repeated 156 times to generate 156 images with SNRs of $25dB$, which were then averaged. It is expected that SNR would increase and thus CBE would decrease with the number of frames used in the average. Fig.3.4 shows SNR with the number of frames in the average, which can be predicted by "initial SNR + $10 \cdot \log_{10}(\text{number of frames})$ ", as the noise is independent. Measured SNR matched the prediction very well.

The corresponding decrease in CBE is illustrated in Fig. 3.5. Because of weak signals, both positive and negative CBE are larger than the prediction in Fig.3.1. In addition, the PCBE curve is not smooth. We removed the weak signals with the thresholding procedure. Resulting CBE curves are smooth and closer to the prediction. We would point out that the CBE computed with the thresholding procedure was not expected to be the same as the prediction in Fig.3.1, because the prediction was made with the

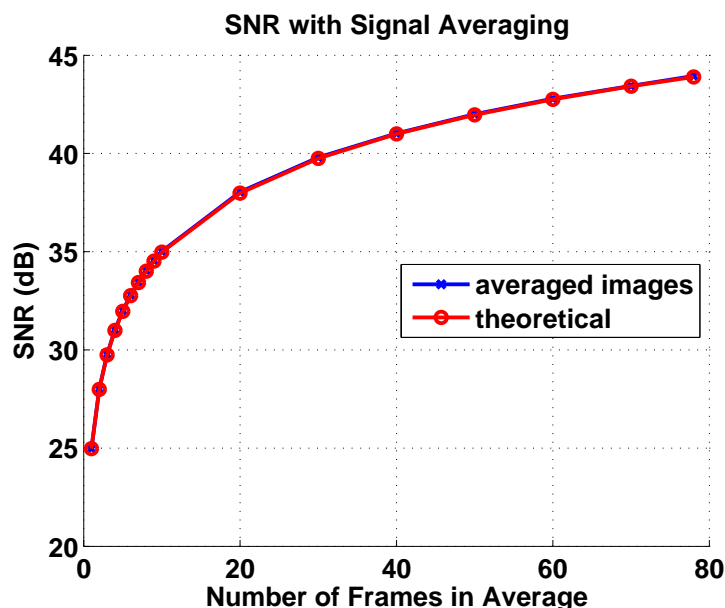


Figure 3.4: Increase of SNR with number of frames used in signal averaging.

assumption of uniformly distributed scatterers while the image of turkey breast was from non-uniformly distributed scatterers. It is difficult to find the ratio distribution of signals from non-uniformly distributed scatterers, which is necessary for predicting CBE with SNR. Details are discussed in Chapters 6 and 8.

In the above result, instead of $21dB$, the threshold was set to $6dB$ below the histogram mode. That is, the threshold is higher than the results from simulated images. This change was necessary because in the true image of a tissue sample, scatterers are not uniformly distributed, so that local SNR varies over the tissue region. As shown in Fig. 3.3, top left and bottom right region contain large amount of weak signals that need to be removed. In Fig. 3.6, a few of the weak signals can be identified when the threshold was $21dB$, while most of weak signals were found when threshold was $6dB$.

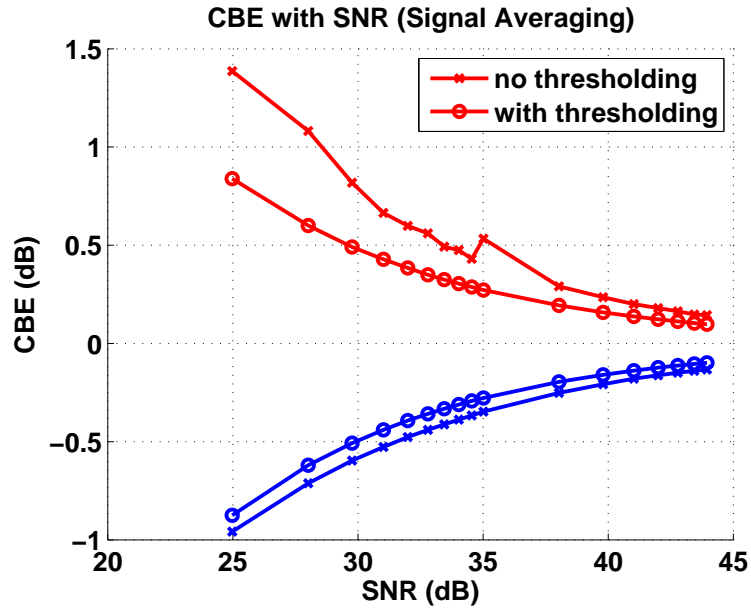


Figure 3.5: CBE with SNR when known noise is added to the image.

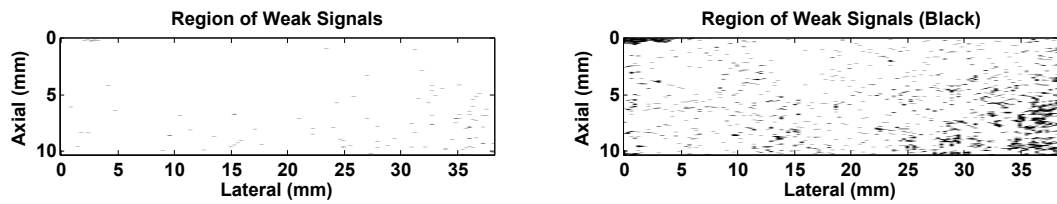


Figure 3.6: Weak signals selected by different thresholds. Left: threshold is $21dB$. Right: threshold is $6dB$.

3.3 Reduction of Motion-induced Spurious CBE

Motion is a common confounding issue in non-invasive tissue temperature imaging [5, 41, 30, 44, 94, 27]. In our group’s initial work, apparent motion in the 1D and 2D images was corrected manually and by a block-matching method, respectively [3, 7]. These results are encouraging for reducing motion-induced spurious CBE. Dr. Trobaugh developed a cross correlation based algorithm for tracking non-rigid motion in 2D images which was extended for 3D motion estimation in this work. We were, however, not able to evaluate the performance of motion compensation without the knowledge of true motion and actual CBE in experiments. In this study, we relied on the simulation tool developed by Dr. Trobaugh [100, 103] to examine the motion correction algorithm. First, effects of motion on CBE, i.e. spurious CBE induced by motion, was inspected. Performance of algorithms to reduce motion-induced CBE was evaluated for simulated images with temperature change and using motion observed in experiments.

3.3.1 Use of Motion Estimation Algorithms

The non-rigid motion compensation algorithm developed by Dr. Trobaugh is briefly described below.

Let $f_1(\mathbf{x})$ and $f_2(\mathbf{x}) = f_1(\mathbf{x} + \Delta\mathbf{x})$ be the reference and shifted images respectively, where $\mathbf{x}, \Delta\mathbf{x} \in R^2$ or R^3 are the coordinate and the motion in it. Our goal is to find an estimate of the motion, $\hat{\Delta\mathbf{x}}$, such that $f_1(\mathbf{x} + \hat{\Delta\mathbf{x}})$ is as close to $f_2(\mathbf{x})$ as possible. The similarity between the two images is measured by their correlation:
$$C(f_1(\mathbf{x}), f_2(\mathbf{x})) = \frac{\sum_{\mathbf{x}} f_1(\mathbf{x})f_2(\mathbf{x})}{\sqrt{(\sum_{\mathbf{x}} f_1^2(\mathbf{x}))(\sum_{\mathbf{x}} f_2^2(\mathbf{x}))}}.$$

$\hat{\Delta\mathbf{x}}$ was modeled to vary linearly over the image region, such that it is a linear function of the motion at the control points, which were chosen as the points at the corners of the image: $\hat{\Delta\mathbf{x}} = g(\Delta\mathbf{x}_1, \dots, \Delta\mathbf{x}_n)$, where n is the number of control points. Then, our goal of finding $\hat{\Delta\mathbf{x}}$ is equivalent to searching for the best estimate of $\Delta\mathbf{x}_1, \dots, \Delta\mathbf{x}_n$ to maximize correlation. This procedure is a multi-variable optimization problem with

the correlation as the cost function:

$$(\hat{\Delta \mathbf{x}}_1, \dots, \hat{\Delta \mathbf{x}}_n) = \underset{(\Delta \mathbf{x}_1, \dots, \Delta \mathbf{x}_n)}{\operatorname{argmax}} C(f_1(\mathbf{x} + \hat{\Delta \mathbf{x}}), f_2(\mathbf{x}))$$

We used the build-in function in Matlab to solve it.

The above algorithm was used to correct for the motion in the images from 3D heating experiments. In each experiment, a sequence of ultrasound RF images was obtained at various temperatures, and motion between adjacent pair of images was estimated and accumulated relative to the reference image. Fig. 3.7 shows 2D frames at various temperatures from experiment TC111 before motion compensation. Apparent motion can be seen between images. Fig. 3.8 shows the motion field in 3D by the arrows at the control points of the tissue volume. The direction of the arrows represents the direction of motion, the length of the arrows represents the magnitude of the motion. It is clear that the motion was non-rigid and increased with temperature. Fig. 3.9 shows the same frames of Fig. 3.7 after motion compensation. The motion in the images is seen to be compensated. These results visually proved that our motion estimation is correct and can be used as true motion in simulations.

3.3.2 Motion-induced CBE

In this subsection, we investigate the effect of motion on CBE. In other words, how much spurious CBE may be produced by motion. Rigid and non-rigid motion in both axial and lateral directions were implemented in simulated images without temperature change. Motion-induced spurious CBE was then computed without compensating for the motion in these images. As shown in Fig.3.10, both PCBE and NCBE increased to a limit with the rigid motion.

For signals from uniformly distributed scatterers such as those in the simulations, work in following chapters shows that CBE is a function of the correlation between two signals in the ratio. When changes in signals are caused only by motion, CBE with motion can be studied as CBE with signal correlation that decreases with motion. Fig. 3.11 shows the prediction of CBE with correlation. When motion is large enough such that the two signals are completely uncorrelated, PCBE and NCBE can be shown to

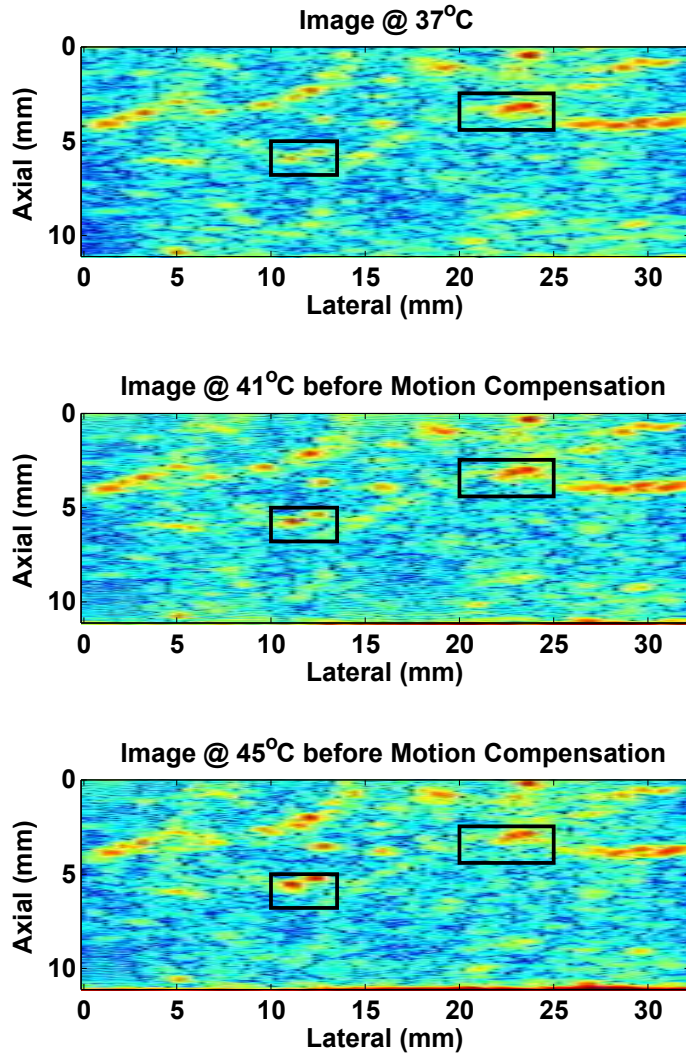


Figure 3.7: Frames at various temperatures from TC111 before motion compensation. Apparent motion can be seen clearly in the boxes.

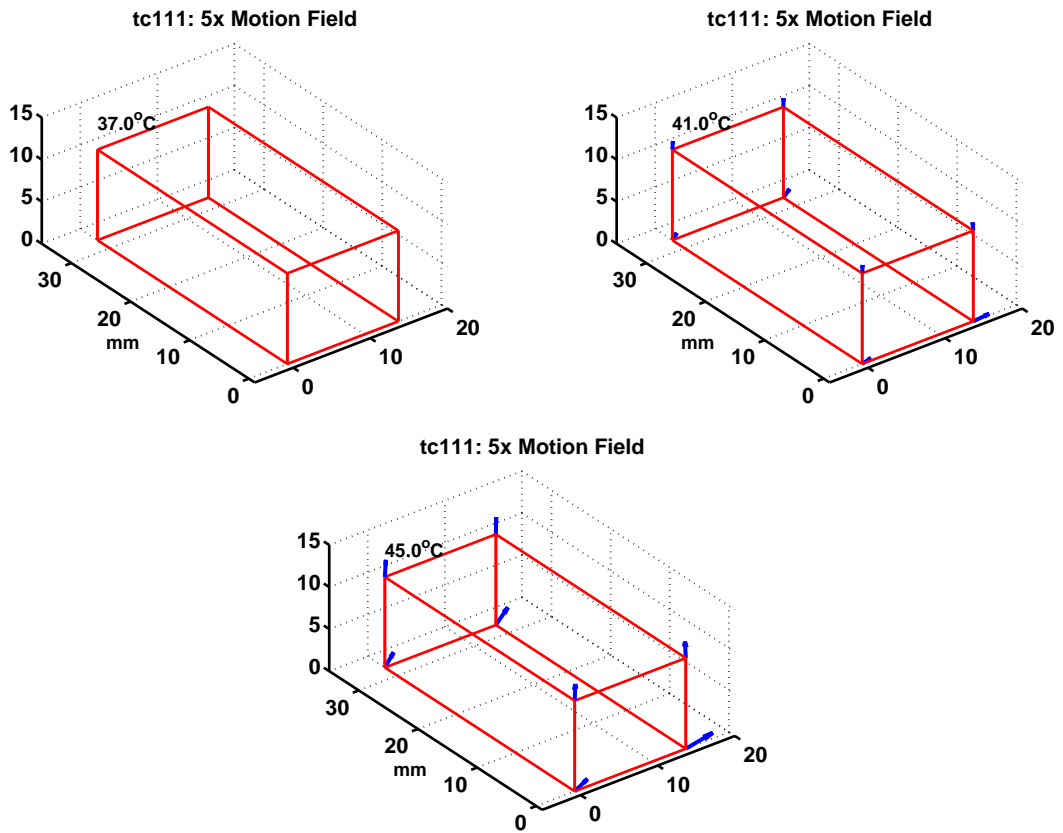


Figure 3.8: 3D motion detected in experiment TC111. The direction and length of arrows represent the direction and amount of motion, respectively. Motion over the 3D region is obviously non-rigid.

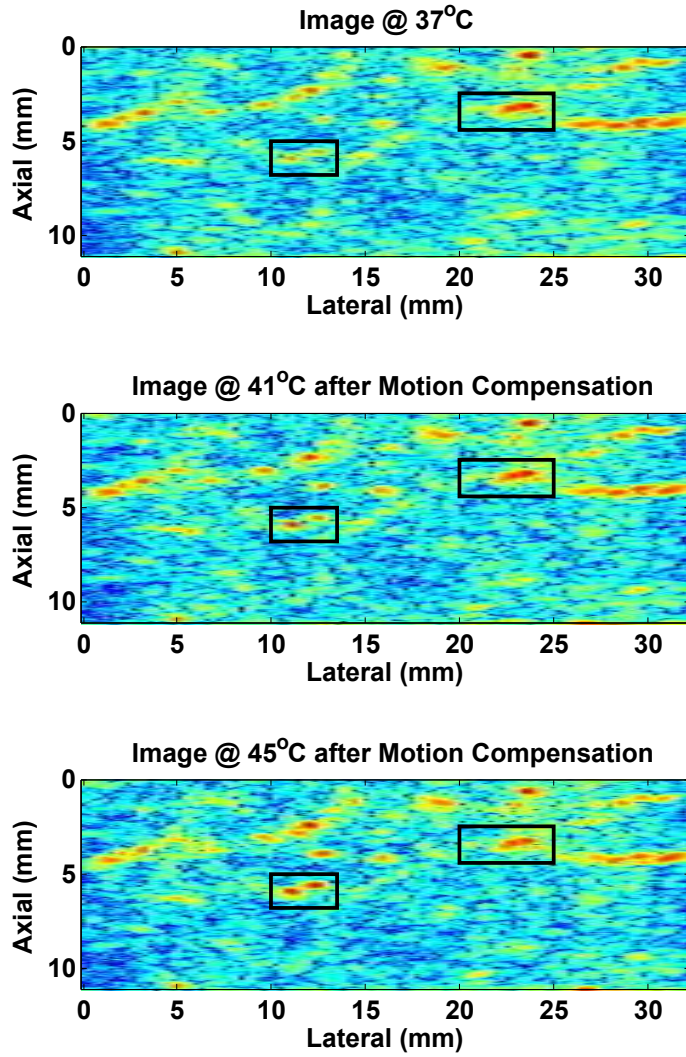


Figure 3.9: Frames at various temperatures from TC111 after motion compensation. The patterns in the boxes show that motion was compensated correctly.

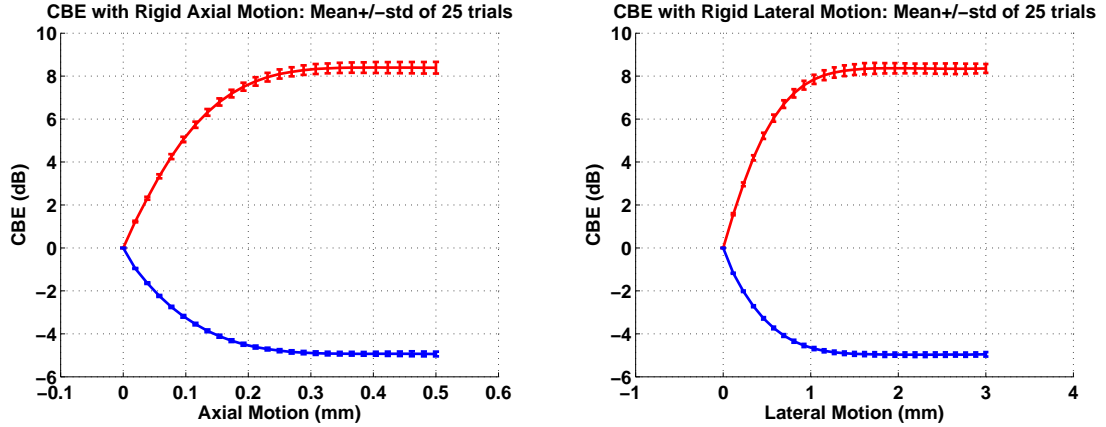


Figure 3.10: Left: CBE increases to a limit with rigid axial motion. Right: CBE increases to a limit with rigid lateral motion.

be $PCBE = 1 + \frac{\pi}{2}$ or 8.2dB and $NCBE = \frac{\pi}{2} - 1$ or -4.87dB. Details can be found in Appendix E. This prediction is consistent with simulation and shows that the CBE is caused by de-correlation due to motion.

As in Fig. 3.12, CBE also increased with the non-rigid motion. When the signals are uncorrelated due to large motion, PCBE and NCBE keep changing slightly. This is because non-rigid motion causes changes in the signal variance of the shifted image, σ_{rf2}^2 , that is, the Rayleigh parameter y_2 varies with motion.

3.3.3 Reduction of Motion-induced CBE

We have seen that motion may cause large spurious CBE since the signals are de-correlated. In this section, we see that spurious CBE can be reduced after compensating for motion. In order to investigate the performance of spurious CBE reduction, we simulated images with temperature change, along with non-rigid motion values seen in heating experiments. As an example, Fig.3.13 shows non-rigid motion detected in heating experiment TC111, which is the "true" motion implemented in simulations. Motion in both axial and lateral direction increased with temperature and varied with location. Motion detected from other experiments was also simulated as true motion.

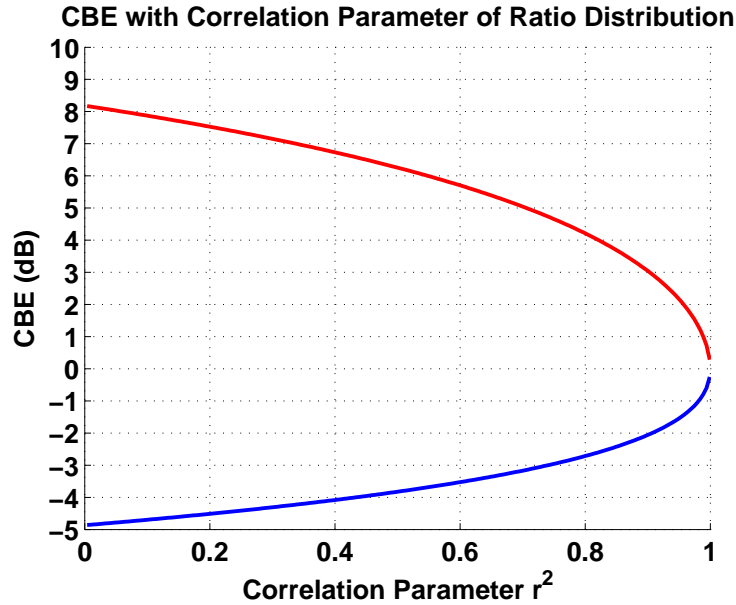


Figure 3.11: CBE variation with correlation computed from the ratio distribution.

Simulations used the baseline settings from experiments as described above, except for SNR which was set to $43dB$ so that we can ignore spurious CBE caused by noise. Fig.3.14 shows the error in motion estimation from simulations based on TC111. CBE computed before and after motion compensation was compared to the CBE without motion, i.e., to CBE due to temperature change. This result is plotted in Fig.3.15. Mean and standard deviation of the residual spurious CBE after motion correction of all simulations is plotted in Fig.3.16.

As shown in the above figures, large spurious CBE was reduced to the level of CBE without motion, after motion was compensated, although there was still residual spurious CBE. An impression from Figs. 3.15 and 3.16 is that residual spurious CBE was reduced with temperature, with its accompanying additional motion. The increasing error in motion estimation shown in Fig. 3.14, however, implies an increase in residual spurious CBE.

This conflict can be explained by thermal change in the signals, which overwhelms other changes in the signals when temperature change is large, and thus CBE without motion dominates spurious CBE. When temperature change is small, change in signals mostly resulted from uncompensated motion effects, so that spurious CBE dominates.

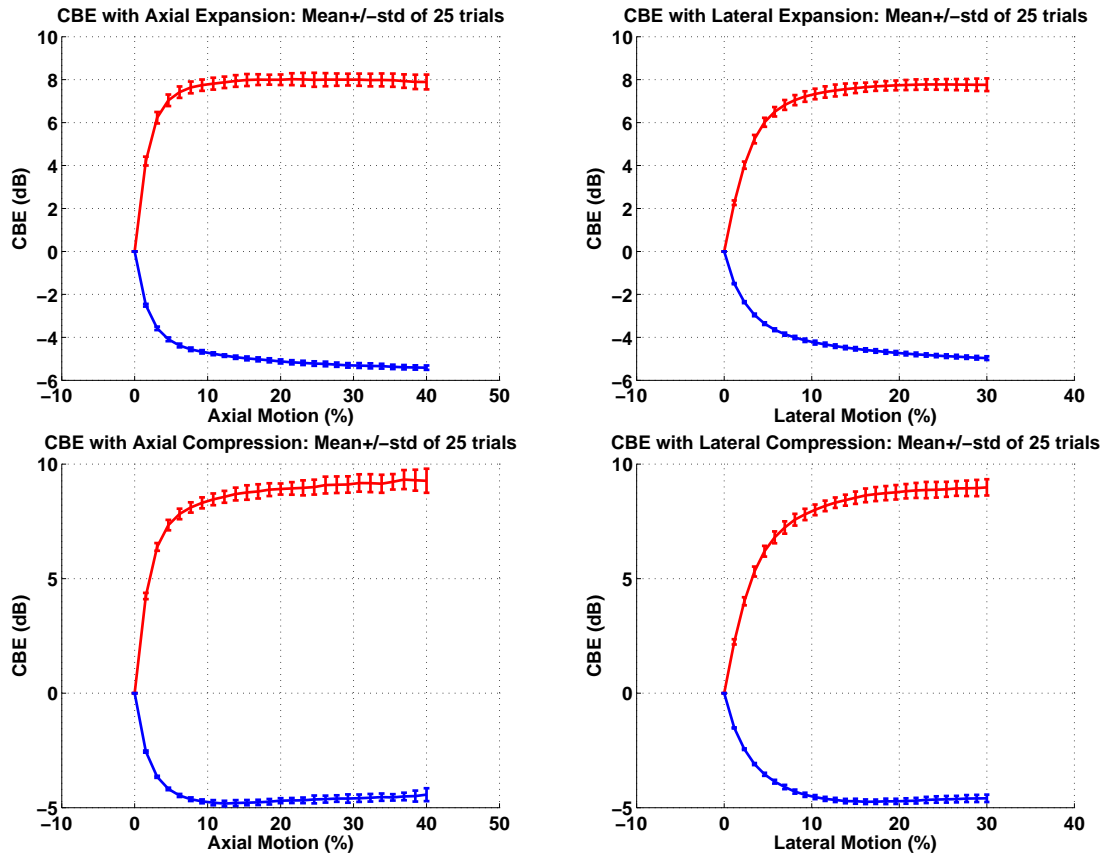


Figure 3.12: Top left: CBE increases with tissue expansion in the axial direction. Top right: CBE increases with tissue expansion in the lateral direction. Bottom left: CBE increases with tissue compression in the axial direction. Bottom right: CBE increases with tissue compression in the lateral direction.

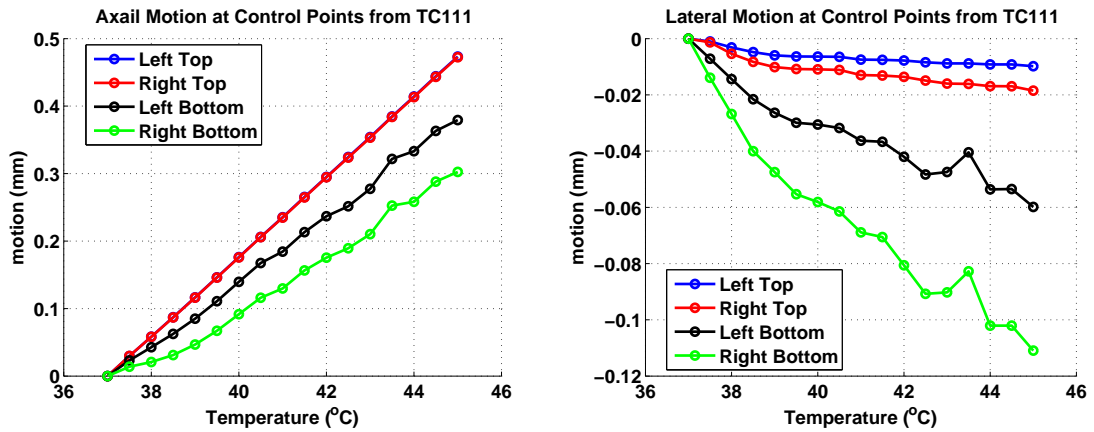


Figure 3.13: Motion detected in heating experiment TC111.

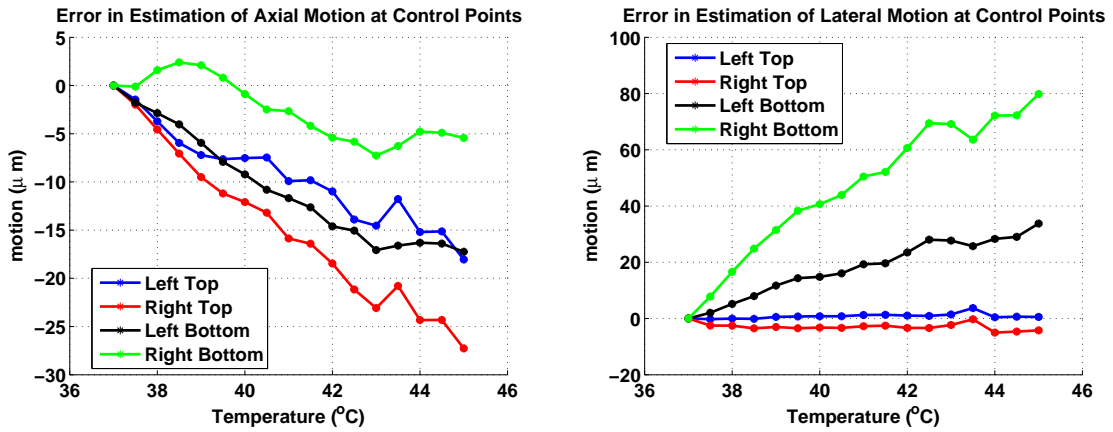


Figure 3.14: Error in motion estimation in simulations based on motion from TC111.

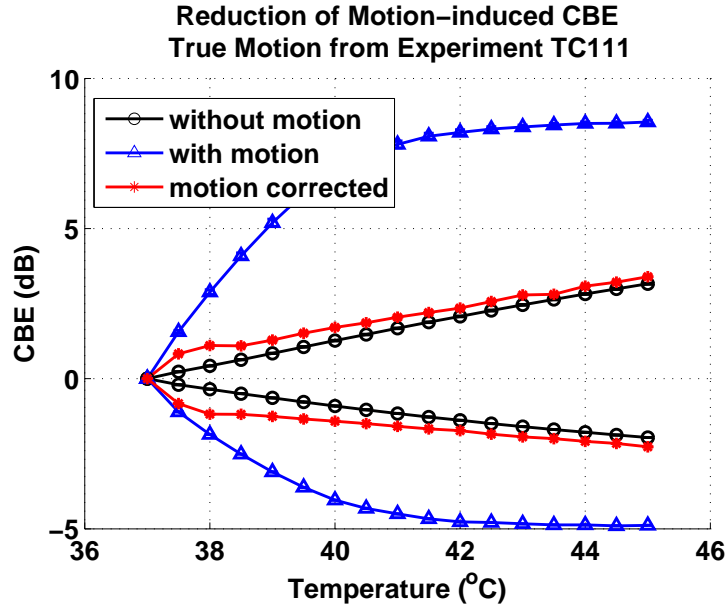


Figure 3.15: CBE computed before and after motion compensation compared to CBE without motion. The amount of motion introduced was based on TC111

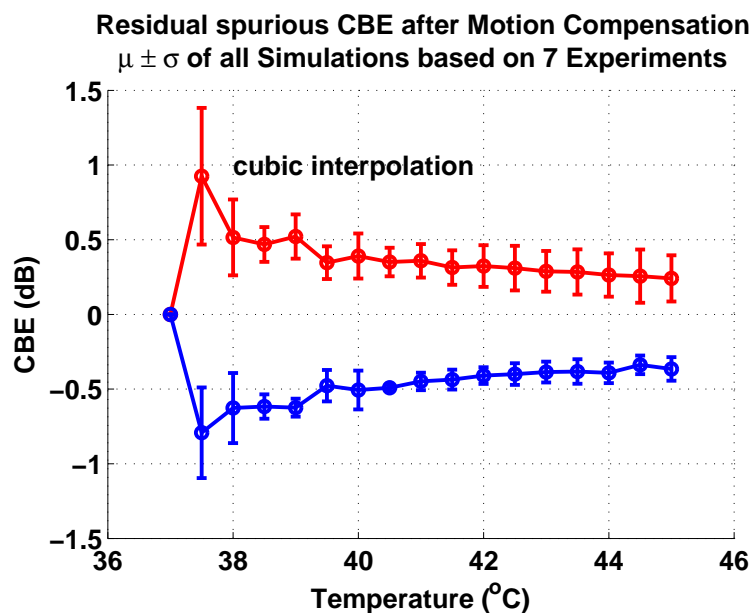


Figure 3.16: residual spurious CBE with cubic interpolation. Mean \pm standard deviation of all simulations.

To illustrate this interpretation, we simulated images with motion based on TC111 but without temperature change. CBE computed before and after motion compensation is plotted in Fig. 3.17. Notice that the x axis is "pseudo" temperature since we did not implement temperature change, but implemented the motion with temperatures as detected in TC111 and shown in Fig.3.13. Residual spurious CBE after motion compensation slightly increased with motion error as expected.

Effect of Interpolation and Sampling Rate on Motion Compensation

The above results show that motion-induced spurious CBE can be reduced by compensating for motion. Residual spurious CBE after motion correction, however, may still be as large as $1 - 1.5dB$ as shown in Fig. 3.16. Residual spurious CBE may result from: 1) error in motion estimation and 2) inaccuracies in image transformation for motion compensation. Previously, we have shown visually that motion in the images can be estimated correctly. Here we consider another cause of residual spurious CBE, the inaccuracy in image transformations.

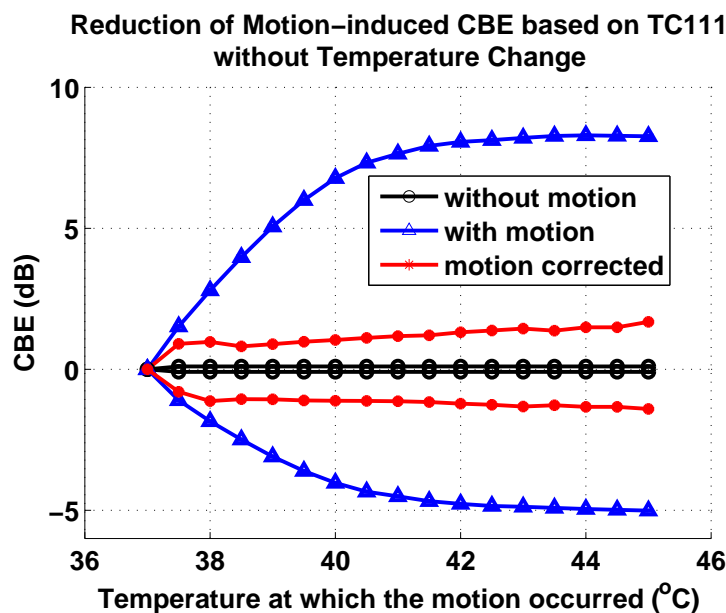


Figure 3.17: CBE before and after motion compensation with cubic interpolation compared to CBE without motion. No temperature change was implemented. The X-axis is the temperature at which the motion occurred.

Motion in the images is not measured in multiples of pixels but of sub-pixels. Therefore, motion in images was compensated by transforming shifted images using interpolation. Interpolation yields an approximation of the true image, and different approaches vary in performance. In the above studies, cubic interpolation built into Matlab was used for image transformation. Below, we compare performance of cubic and spline interpolation of a sine wave in a simple test. In the left part of Fig. 3.18 shows a sine wave and the same wave shifted by half a sample. We interpolated the shifted sine wave to restore it to the original one using both cubic and spline interpolations. The error in the restored signal is shown in the right part of Fig. 3.18. Clearly, transformation with splines has better performance in this case.

Performance of interpolation methods is affected by the sampling rate of the signal. If the sampling rate is high enough, even simple methods, such as linear interpolation may have good performance. In Fig. 3.19, we doubled the sampling rate of the original and shifted signals. Performance of both cubic and spline interpolations was improved and their difference was reduced.

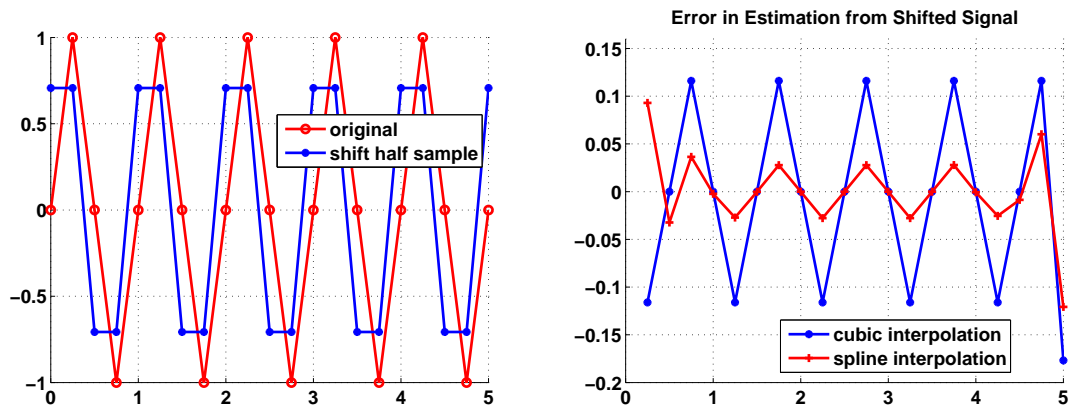


Figure 3.18: Effect of interpolation on image transformation. Left: Original and shifted sine waves. Right: Error in estimation of the original wave from the shifted one using cubic and spline interpolations.

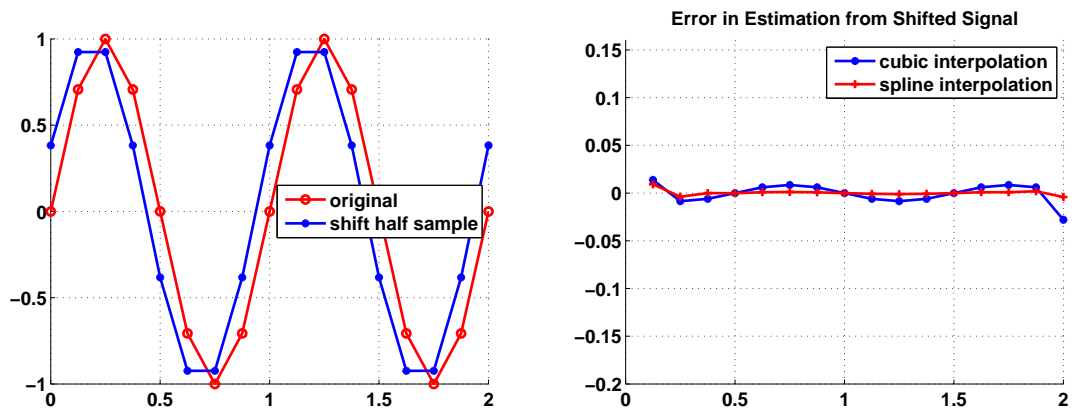


Figure 3.19: Effect of interpolation on image transformation with double the sample rate. Left: Original and shifted sine waves. Right: Error in estimation of the original wave from the shifted one using cubic and spline interpolations.

The above discussion implies that reduction of spurious CBE may be improved by employing appropriate transformation methods, such as spline interpolation, or by increasing the sampling rate. We repeated the simulations with motion and temperature change and used spline interpolation in motion compensation. Mean \pm standard deviation of residual spurious CBE after motion compensation is plotted in Fig.3.20. As expected, residual spurious CBE with spline interpolation is much smaller than that with the cubic method in Fig. 3.16.

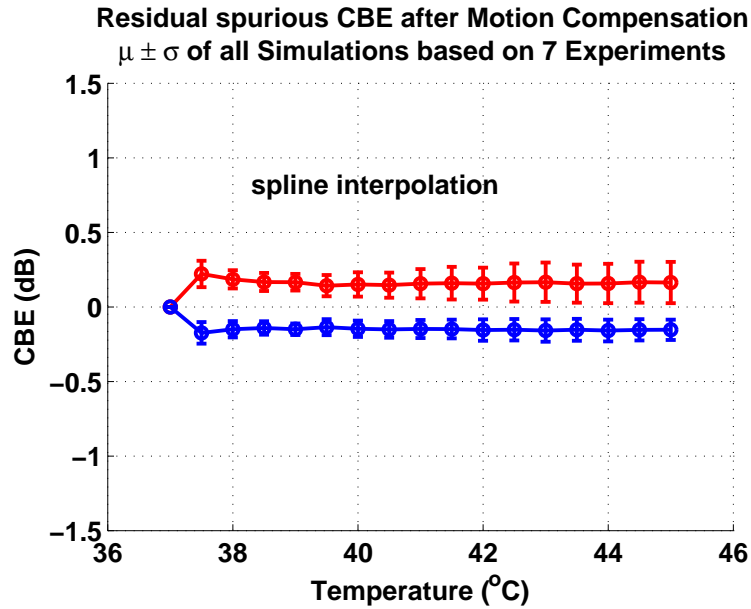


Figure 3.20: residual spurious CBE with spline interpolation. Mean \pm standard deviation of all simulations.

In order to examine whether or not increasing the sampling rate reduces spurious CBE, the above simulations were repeated with doubled sampling rate in the axial direction. Residual spurious CBE is plotted using both cubic and spline interpolation in Fig. 3.21.

As shown in Fig. 3.21, when the axial sampling rate is doubled, cubic interpolation has similar performance as spline interpolation. Both of them produce less residue spurious CBE, about $0.1dB$, at lower temperatures than spline interpolation at the original sampling rate. Of course, higher the sampling rate implies more computational load. A problem of increasing sampling rate, however, is that it may require a change in hardware.

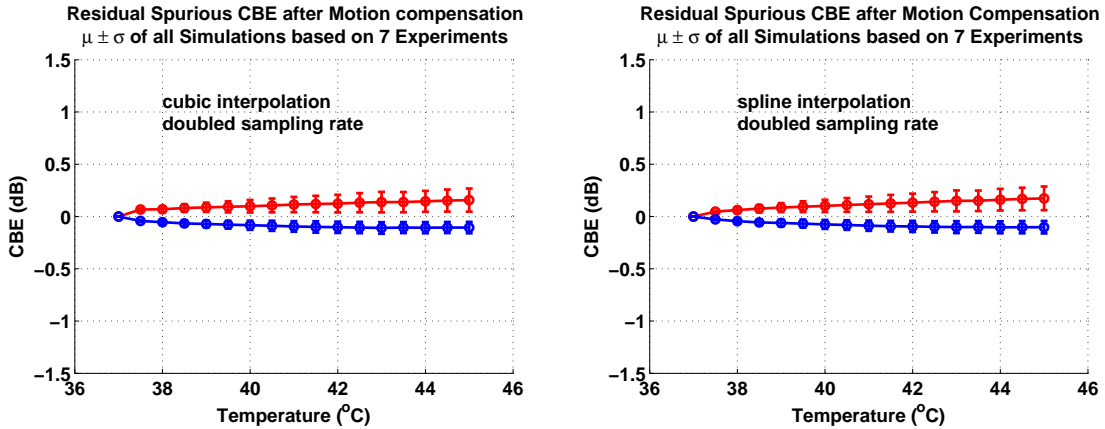


Figure 3.21: Residual spurious CBE with double the axial sampling rate. Mean \pm standard deviation of all simulations. Left: Cubic interpolation. Right: Spline interpolation.

Alternatively, we may up-sample the image taken with the original sampling rate instead of increasing the sampling rate during image formation. We simulated images with motion and temperature change at the original sampling rate and for images up-sampled in the axial direction for motion estimation and compensation. Fig.3.22 shows residual spurious CBE with up-sampling in the axial direction, which is similar to the results with doubled axial sampling rate.

We also repeated the simulations with up-sampling in both axial and lateral directions. The result shown in Fig. 3.23 also shows less residual spurious CBE than the result with spline interpolation at the original sampling rate.

Effect of Signal to Noise Ratio

In the above simulation study, signal-to-noise ratio (SNR) was set at $43dB$, so that noise effects could be ignored. In contrast, to see the effect of noise on motion detection, we simulated images with motion at $23dB$ of SNR and estimated motion with cubic interpolation. Error in motion detection is shown in Fig. 3.24.

Comparing Fig. 3.24 to Fig. 3.14, it can be seen that motion detection at SNR= $23dB$ is almost the same as that at SNR= $43dB$. This result implies that our motion detection algorithm is robust to noise. This may be because we use cross correlation as the cost function, for which noise may change the magnitude of its peak but not its

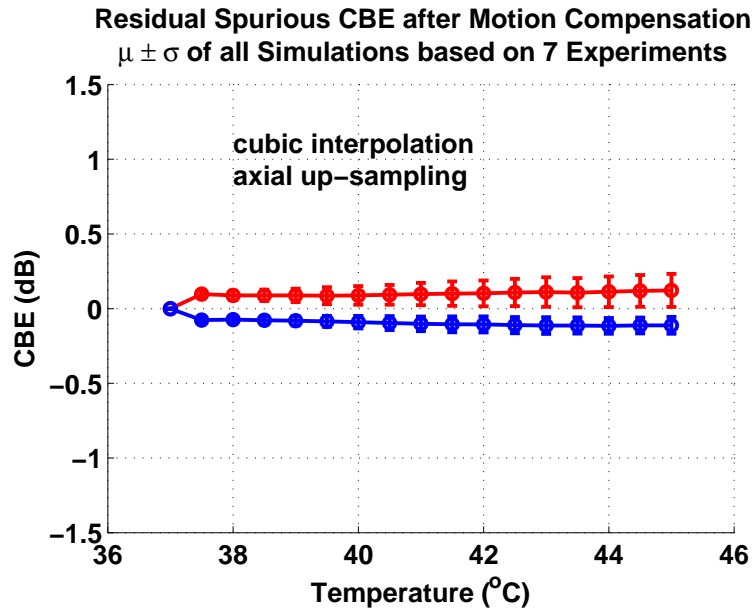


Figure 3.22: residual spurious CBE with cubic interpolation axial up-sampling. Mean \pm standard deviation of all simulations.

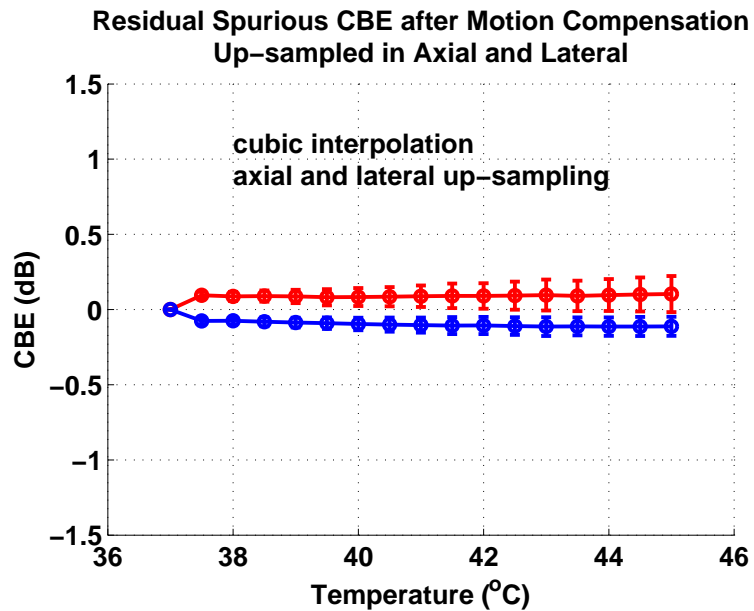


Figure 3.23: residual spurious CBE with cubic interpolation and up-sampling in both directions. Mean \pm standard deviation of all simulations.

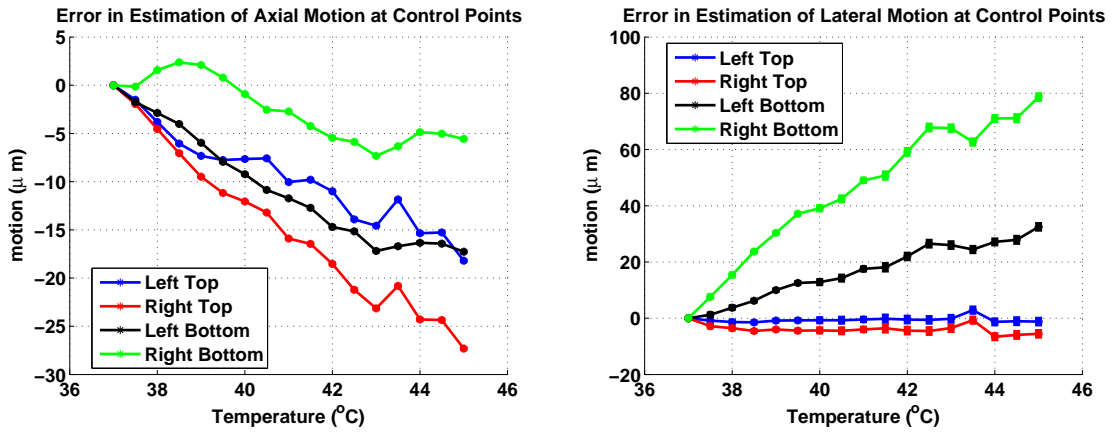


Figure 3.24: Error in motion estimation in simulations based on motion from TC111 at $23dB$ of SNR.

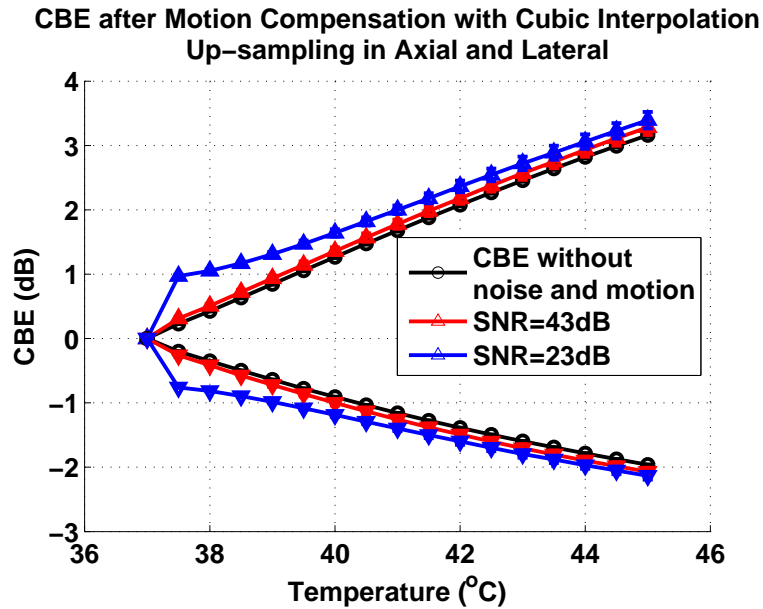


Figure 3.25: CBE after motion compensation at SNR = 23 and 43dB. Mean \pm standard deviation of simulations for all experiments. Cubic interpolation with up-sampling in both axial and lateral directions.

peak location. CBE after motion compensation with up-sampling in both directions is plotted in Fig. ???. Obviously, CBE after motion compensation at $43dB$ of SNR is much closer to the CBE without noise. This comparison is unfair since most of the residual spurious CBE at $23dB$ of SNR was caused by noise. Nevertheless, this result reminds us that effects of noise and motion need to be handled together.

3.4 Summary and Conclusions

In this section, we showed that motion in the images can produce large spurious CBE. Spurious CBE, however, can be reduced by our motion compensation algorithm. Interpolation approaches and sampling rates have a big impact on image transform and are important to the performance of motion compensation algorithms. In addition, we showed that motion compensation is more important at small temperature deviations from the reference temperature, because CBE due to thermal change in signals dominates when the temperature change is large. These observations will be verified in experiments described in the following chapters.

Chapter 4

System for *In-vitro* 3D Image Acquisition

In order to validate our CBE based thermometry, we constructed an imaging system for 2D&3D *in-vitro* experiments. In this study, 2D images were acquired in null experiments, during which the temperature was consistent. For heating experiments, the capability of acquiring 3D images is significant since: 1) our ultimate goal is to measure temperature in a 1cm^3 volume; 2) apparent motion should be corrected in 3D.

As shown in left of Fig.4.1, our imaging system consists several components: a specimen and thermocouple holder, a heating and circulating device, temperature sensors, an image formation system, and a transducer positioning device. These components are connected, through serial ports, to a dedicated laptop. A Matlab program is used for control of the components.

4.1 Specimen and Thermocouple Fixture

Fig.?? shows the arrangement of tissue specimen and the thermocouples. For uniform heating experiments and null experiments, tissue specimen is in a tank filling with deionized and degassed water, which is used as coupling media. A metal plate is fixed in a slot at the bottom of the tank by a screw. Position of tissue specimen is kept by four pins on the plate and an plastic holder. There are two thermocouple positioning

4.3 Temperature Measurement

Tissue temperature was monitored by thermocouples (OMEGA Industrial Hypodermic Probe, Hyp-3, OMEGA Engineering INC., Stamford, Connecticut) connected to computer through Dataq DI-1000TC data acquisition box (DATAQ Instruments Inc. Akron, OH). Installation information can be found in its manual [26].

Dataq DI-1000TC has 8 channels (inputs) for 8 thermocouples and allows high accuracy of $\pm 0.2\%$ of the span and resolution of $0.08^\circ C$. It is connected to PC through USB to RS-422 adapter. Temperature readings from thermocouples can be acquired by either Windaq Data Acquisition Software provided by DATAQ Instruments Inc or Active X Control which is installed when Windaq is installed. In order to read temperature measurement into Matlab program, we use Active X control to access data stream being acquired by WinDaq Data Acquisition software, which should run in the background. The control is created in Matlab by:

```
windaqhdl = actxcontrol('WINDAQ.WindaqCtrl.1');
```

where "WINDAQ.WindaqCtrl.1" is program ID of the control and windaqhdl is the handle of the control. Access of data can be started by execute "windaqhdl.Start". Temperature of *n*th channel is read calling the function below:

```
temperature = GetScaledData(windaqhdl, channel number);
```

where sample rate is fixed at 5 samples/second/channel. The control is ended and removed by executing "windaqhdl.Stop" and "windaqhdl.delete"

The thermocouples were calibrated with respect to the internal thermistor of Haake circulator. Fig.4.2 shows the the difference between thermocouple readings and thermistor readings with temperature from three calibration heating experiment. It is seen that, for each thermocouple, the slopes of the difference curves from the three experiments are consistent, but the offsets are different. Therefore, we adjust thermocouple reading by a linear model determined by the slope and offset of the difference curve. The slope is measured in the calibration experiments and stored for later use. The offset will be measured at the beginning of each experiment.

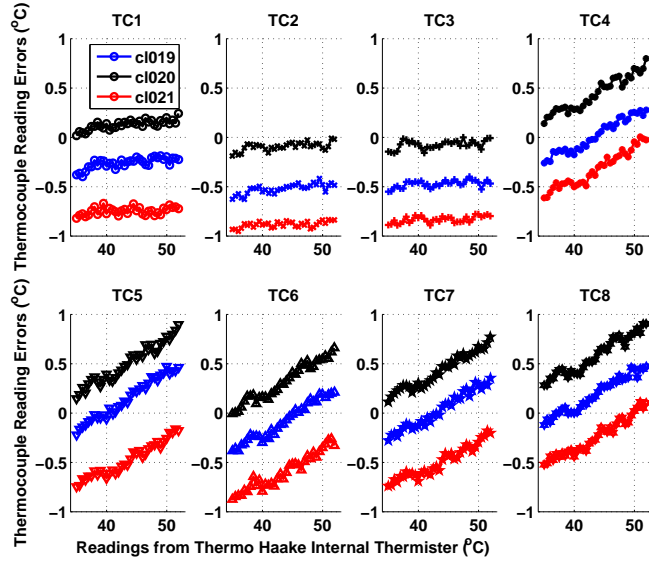


Figure 4.2: Errors between thermocouple and ThermoHakke thermistor readings. Errors had the same slope, but different offsets over the set of calibration experiments.

4.4 Image Acquisition

Ultrasonic RF images of specimen are acquired using Terason 3000 system (Teratech Corp., Burlington, MA) with a 128-element, 7MHz linear array transducer(12L5). Terason 3000 (T3000) can work in 4 mode: B-mode, M-mode, color Doppler and power Doppler. In this study, we monitored specimen in B-mode from Terason GUI interface during experiments.

In general, an exam is loaded after T3000 starts, which defines parameters such as mode, gain, depth, and focus distance. When image is ready for acquisition, it is frozen and saved as either a 2D image or a loop (an array of 2D images). By default RF images are saved in T3000 format with extension ".ult", which can be converted to Matlab data file (".mat") using program "ult2matlab.exe" provided by Teratech. Images can also be saved in BMP, JPEG and TIFF format.

In order to acquire images automatically during experiments, the above acquisition procedure should be performed in our Matlab control program. It was first done using AutoIt 3 which is a language for automating Windows GUI. AutoIt commands

can be executed in Matlab by running an AutoIt script named with extension ".au3" or directly calling AutoIt functions defined in a shared library "AutoItX3.dll". We created an AutoIt script, "OpenTerason.au3", to start T3000 GUI and load an exam denoted by "cbe", as described in Appendix A.

Although automatic image saving was achieved by using AutoIt, we have to wait between commands to ensure they are finished. It also happened, although only occasionally, that T3000 can not return to live image for new scans. This may be because there is delay or error in the communication between AutoIt and Windows operation system . In addition, we found that, after saving a set of images, T3000 has to be closed and saved images have to be moved from default folder to other folders. Otherwise, further image saving will be slowed down. In order to make more reliable imaging, we recently implement control of Terason imaging using the software development kit (SDK) from TeraTech.

The SDK allows us to access Terason image stream via ActiveX control in our Matlab control program. Before create ActiveX control, 3 .ocx files should be registered:

```
Regsvr32 TTFrameReceiver.ocx Regsvr32 TTAutomate.ocx Regsvr32 TTSimpleImageWnd.ocx
```

We created 3 functions for acquiring images using the SDK:

1. hTTauto = StartTerasonActx(exam)

This function starts Terason Imaging system, creates TTAUTOMATE control, attaches the control to a running instance of Terason and load the exam defined by "exam" which is a character string of exam name. It returns a handle of the ActiveX control.

2. savesglimage_ttauto(hTTauto,filename)

This function freezes current Terason scan, save a 2D image to the folder and file name defined in "filename", and then unfreeze the image. Since images can be saved to assigned folder, we do not have to remove saved file from default folders.

3. saveloop_ttauto(hTTauto,filename)

This function freezes current Terason scan, save a loop of images to the folder and file name defined in "filename", and then unfreeze the image. Unfortunately, number of frames in a loop can not be changed by control program. It is determined by the image size and the frame rate, which depends on computer OS.

The scripts of these function can be found in appendix A. By using the ActiveX control to access the image stream, acquisition procedure is more reliable and faster. The above 3 functions are simple applications only for our current experiments. The SDK provides many other functions for more complicated applications. For example, we can change depth or focus distance after loading the exam. It gives us more flexibility in future experiments. More capability of data processing, such as online signal averaging, is desired. But this requires cooperation with TeraTech Inc and more resource.

4.5 Transducer Positioning

To position the transducer, we use 3 Newport IMS300PP stages, for 3 axes in axial, lateral and elevation directions, controlled by ESP300 controller (Newport Co., Irvine CA). IMS300PP stages can reach maximum speed of 100mm/s and resolution of $1.25\mu\text{m}$. ESP300 controller integrates both controller and motor driver for up to 3 axes. It can work in 3 operation modes: 1) local mode: use front panel 2) remote mode: execute command from computer 3) program execution mode: execute stored program. In our study, it works in remote mode and is connected to computer via serial port with parameters: baud rate 19200, data bits 8, stop bit 1, terminator 'CR'.

The commands are in format of:

xxAAnn

where "AA" is 2-character command, "xx" is preceding parameters and "nn" is following parameter. For example, "1VA20" set speed of axis 1 to be 100unit/second. Each command should end with a carriage return. For the purpose of moving transducer in 3 directions, following commands are used:

xxSNnn or xxSN? – set or report current unit for axis xx
xxVUnn or xxVU? – set or report maximum speed for axis xx
xxVAnn or xxVA? – set or report speed for axis xx
xxMO or xxMO? – turn motor on or report if motor is on for axis xx
xxMF or xxMF? – turn motor off or report if motor is off for axis xx
xxPRnn – move axis xx by nn units from current position
xxMD? – report if move of axis xx is done

Functions for initializing serial port and sending command are built in a shared library: ESP232.dll. It can be loaded into Matlab by executing "loadlibrary('ESP232.dll')". Three functions in the library are called in our Matlab control program:

```
calllib('ESP232','esp_232_open', command)
calllib('ESP232','esp_232_send_ascii', command)
calllib('ESP232','esp_232_read_ascii', command)
```

For convenience, we constructed several Matlab functions for moving the axes:

newport_sendcmd(axNum,cmd,varargin) – send command "cmd" for axis "axNum" with optional parameter. e.g. `newport_sendcmd(1,'PR',10)`

output = newport_read(axNum,cmd) – read information of axis "axNum" according to command "cmd". e.g. `newport_read(1,'MD?')`

newport_motorOn(axNum) – turn on motor for axis "axNum"

newport_initial(axNum,unit,speed,spdMax,serialport) – open serial port, set unit, speed and maximum speed for axes defined in array "axNum". Notice that unit change requires changing configuration file and downloading the controlling in ESP utility provided with Newport software.

newport_mv(axNum,dir,dist,wait,varargin) – move axis "axNum" for "dist" units in "dir" direction. Do not execute next command until motion done if "wait" is "1". "varargin" defines speed other than that set in `newport_initial()`.

newport_motorOff(axNum) – turn axis "axNum" off.

4.6 Configuration of Heating Experiments

In homogenous heating experiment, specimen is placed in deionized and degassed water heated by Haake circulator. Images are acquired at each of the preset temperatures, usually $37 - 45^{\circ}C$ with $0.5^{\circ}C$ intervals. Water temperature is measured by Haake internal thermistor and specimen temperature is measured by 4 calibrated thermocouples. When water temperature reaches current preset temperature, heating stops while circulating continues until the specimen reaches thermal equilibrium. Specimen is regarded in thermal equilibrium when difference between all 4 thermocouple measurements and water temperature is less than $0.3^{\circ}C$.

Transducer is usually focused at $4.5cm$ in axial, around the center of the specimen. In 3D heating experiment, at each temperature, a set of 30 frames are captured with $0.6mm$ in elevation. These images are acquired in a "stop and shoot" manner. The control program first freeze the Terason scan, then starts to move the transducer in elevation direction for $0.6mm$ using Newport stage 1. Newport stage 1,2and 3 correspond to elevation, lateral and axial direction respectively. During the motion of transducer, a 2D image is saved and Terason scan is unfrozen. When transducer motion is finished, image of specimen at new position is frozen and the above procedure is repeated until all 30 frames are acquired.

4.7 Null Experiments

To study non-thermal change in backscattered signals, we need to conduct null experiments, during which tissue temperature does not change. Basic experiment setup is same as above. Changes are made according to the purpose of the study. For example, when studying effect of noise, we acquire loops of images at same position instead of 30 frames at different positions. Details will be described in the following chapter.

Chapter 5

Verification of Reduction in Spurious CBE Induced by Noise and Motion

In chapter 3, we evaluated approaches to reducing spurious CBE caused by noise and motion in the images using simulation tools. In this chapter, we verify the results of chapter 3 using experimental data.

5.1 Verification of Noise Reduction Method

In order to verify the approaches to reducing noise effects developed in Chapter 3, signal averaging and thresholding are applied to loops of images acquired in null experiments. CBE was computed for frames within and between loops. Variations of SNR and CBE with frame averaging and thresholding are compared to the results in Chapter 3.

5.1.1 Noise in Images of Real Tissue

We assumed noise is additive to the RF images as before: $s = i_{rf} + n$. If two images are acquired successively for the same target, $s_1 = i_{rf} + n_1$ and $s_2 = i_{rf} + n_2$, their difference contains only the difference of the noise. Furthermore, if n_1 and n_2 are

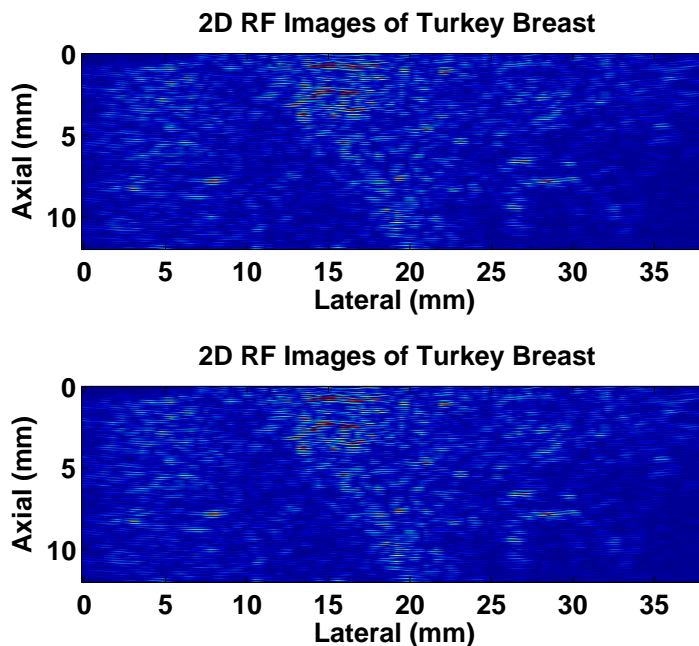


Figure 5.1: RF images of turkey breast acquired in loop 1 of a null experiment. Top: frame 1 of loop 1. Bottom: frame 2 of loop 1.

independent, identically distributed Gaussian, $n_1, n_2 \sim N(0, \sigma_n^2)$, their difference is also Gaussian, $\Delta s = n_1 - n_2 \sim N(0, 2\sigma_n^2)$.

We acquired a set of 2D images (frames) of the same piece of turkey breast sample using "save loop" function of Terason 3000 imaging system. Because a loop was captured in a couple of seconds, true signal i_{rf} can be regarded unchanged within the loop. Fig. 5.1 shows two frames in a loop. They can not be distinguished by eye inspection. Fig. 5.2 shows the histogram and fitted Gaussian distribution for frame one. The mismatch of signal histogram and Gaussian distribution may be due to the scatterers in real tissue do not distribute uniformly. Signal distribution is discussed in detail in following chapters.

To obtain noise information, we subtracted the second frame from the first one assuming the noise is additive. As shown in left part of Fig. 5.3, the difference of two RF images behaves as random noise. The histogram of the difference image and fitted Gaussian distribution are plotted in right part Fig. 5.3. This histogram matches a Gaussian distribution very well since the backscattered signal from tissue was nearly

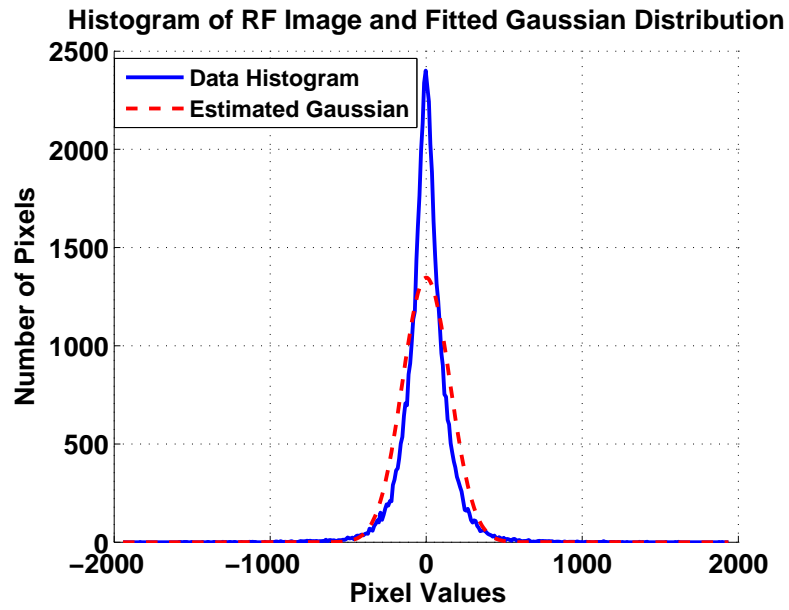


Figure 5.2: Histogram and fitted Gaussian distribution for an RF image of turkey breast.

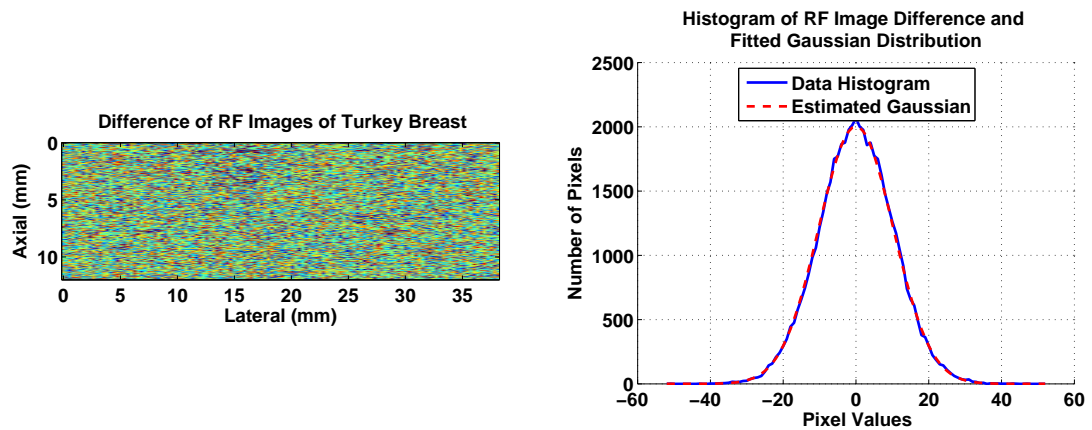


Figure 5.3: Left: Image of the difference between two RF images in a loop. Right: Histogram and fitted Gaussian distribution for the difference of RF images of turkey breast.

eliminated and the difference image contained only the difference between noise. According to this result, it is reasonable to assume, as in Chapter 3, that the noise in RF images of real tissue is additive Gaussian noise with zero mean.

5.1.2 Reduction of Noise-Induced Spurious CBE

We have demonstrated that noise causes spurious CBE which can be reduced by increasing SNR. Here, we study the feasibility of increasing SNR and thus reducing noise-induced spurious CBE in experimental data by signal averaging and thresholding. Experimental data were collected from null experiments during which tissue sample was kept at room temperature and desired CBE was $0dB$.

Null experiment

In the null experiments, Terason 3000 imaging system, with a 128-element, 7MHz transducer(12L5), was used to acquire "loops" of 2D frames of turkey breast. The number of frames in each loop was determined automatically by the Terason 3000 according to frame size and frame rate. Tissue sample was fixed in a holder and left in de-ironized, de-gased water for 3 hours, so that both water and tissue reached room temperature which was then assumed invariant during the experiment.

Tissue temperature was monitored by four thermocouples. Fig. 5.4 shows variation of tissue temperature during null experiment NL002 measured by 4 thermocouples. Tissue temperature dropped with time for less than $0.2^{\circ}C$, whose effect on CBE was ignored. It was also assumed that all possible tissue movements, such as swelling, was absent during the 3 hours so that no motion induced CBE appeared in our computation. In a heating experiment, data sets are typically acquired at 17 temperatures. To mimic this procedure, 17 loops, with 156 frames in each loop, were acquired with 2 minute intervals in the null experiments.

Intra-loop CBE

Since it took only 2-3 seconds to acquire a loop depending on the frame rate, we assumed that there was no change in tissue temperature, backscattered signals and noise variance within a loop. CBE was computed between frames within each loop,

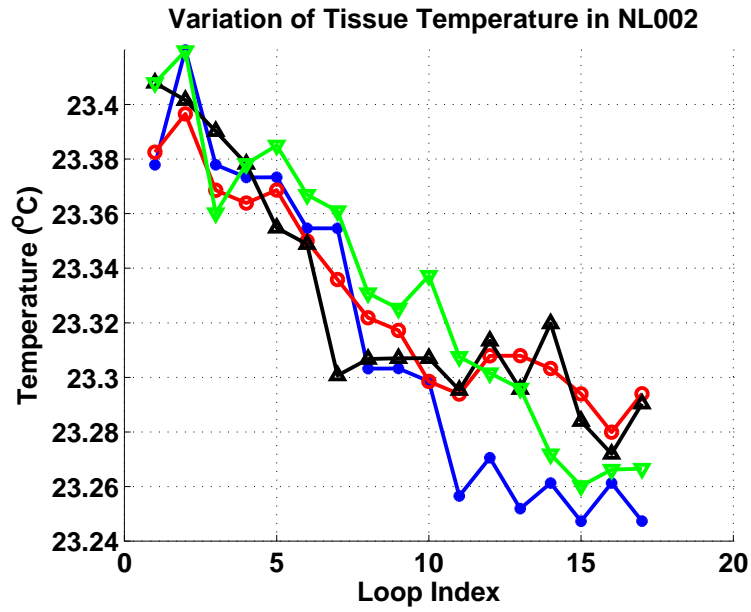


Figure 5.4: Variation of tissue temperature during null experiment NL002.

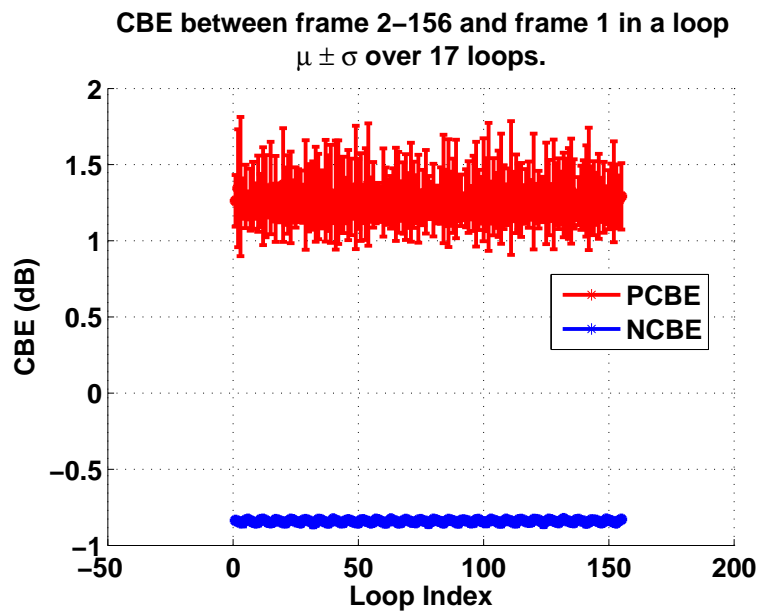


Figure 5.5: Intra-loop CBE: CBE between each frame and the first frame in a loop of NL002. $\mu \pm \sigma$ over 17 loops.

denoted as intra-loop CBE, by comparing each frame to the first frame in the loop. In experiment NL002, a loop contained 156 frame and therefore 155 CBE values can be calculated for each loop. The mean and standard deviation of intra-loop CBE over 17 loops are shown in Fig. 5.5. As expected, both PCBE and NCBE are non-zero due to noise, but are consistent within a loop. PCBE has larger variation among loops, because, as discussed in Chapter 3, "weak" signals were affected by the noise significantly and generated "outliers" in the ratio computation. The "outliers" in the ratio region less than 1 are constrained to be larger than zero, while those larger than 1 could be arbitrary large, so that PCBE varied more than NCBE.

In order to see how SNR and CBE changes with signal averaging, we computed SNR and CBE when averaging 1,2,...,10,20,30,40,50,60, and 70 frames for each loop. Notice that, to obtain information of noise in averaged images, at most seventy eight frames can be used in averaging for each loop. Noise variance was computed as described in the beginning of this section. Fig. 5.6 shows that SNR increasing with number of frames in averaging by about 20dB ($25 \sim 45dB$), which is close to, but a little higher than theoretical prediction. The corresponding reduction of CBE with signal averaging is plotted in Fig. 5.7. Magnitudes of both PCBE and NCBE decreased to $0.1 \sim 0.15dB$ when 70 frames were averaged.

The above results illustrate that SNR can be increased and thus spurious CBE can be decreased by averaging frames in a loop. We wish to see how CBE changes with SNR, which is shown in Fig. 5.8. PCBE reduced from $1.25dB$ to $0.15dB$ and NCBE increased from $-0.8dB$ to $-0.15dB$ when SNR was increased from $25dB$ to $45dB$.

Comparing Fig. 5.8 to Fig. 3.1, CBE computed from experimental data is close to prediction when SNR is high. CBE from experimental data is, however, larger than the prediction when SNR is low. As found in Chapter 3, larger CBE from experimental data was resulted from corruption of small signals by noise. In addition, signal backscattered from tissue varied largely. In regions of small signals, SNR was extremely low such that spurious CBE was very high as shown in the previous subsections. The black rectangle in Fig. 5.9 shows the region from which above CBE was computed. The right bottom part of this region looks more like noise. At the left top corner, even a small portion of noise signal was involved in CBE computation. As a rough selection of "strong" signals, we computed CBE again from a region with

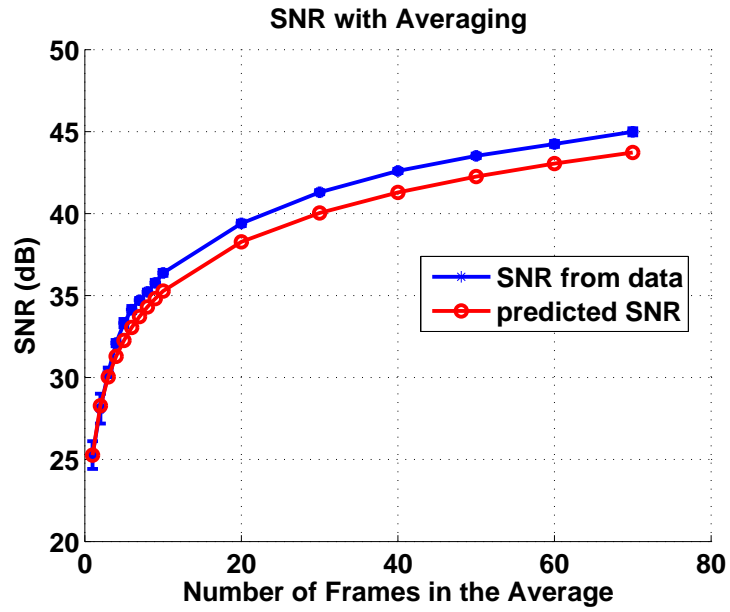


Figure 5.6: Variation of SNR with number of frames in the average for all 17 loops in null experiment NL002.

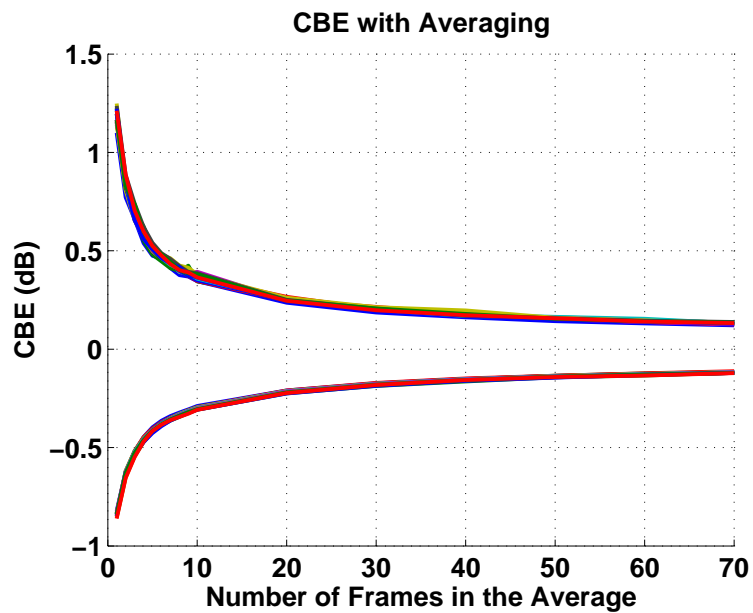


Figure 5.7: Variation of CBE with number of frames in the average for all 17 loops in null experiment NL002.

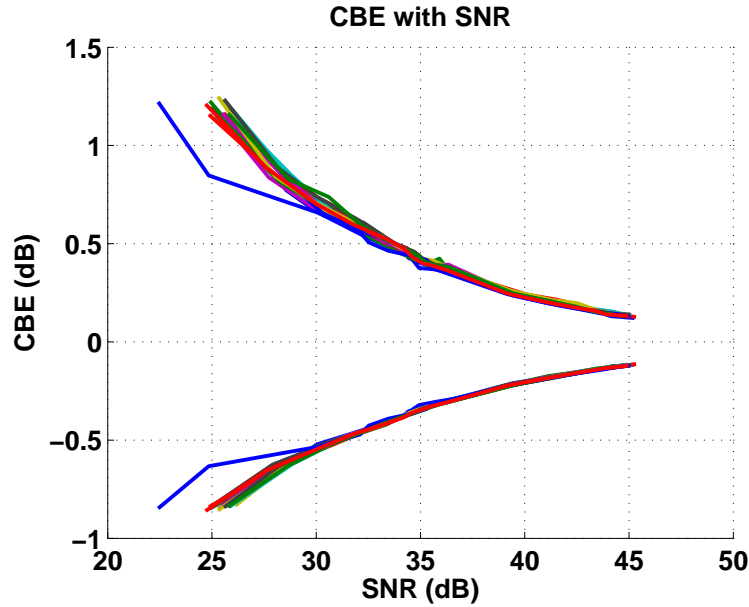


Figure 5.8: Variation of CBE with SNR for all 17 loops in null experiment NL002.

less noise and weak signals as shown by the blue rectangle in Fig. 5.9. The CBE from this "strong" signal region, shown in the Fig. 5.10, is closer to the predictions than previous result.

Although the CBE computed from the strong-signal region is closer to the prediction, weak signals still exists in this region which may be the cause of the spike in Fig. 5.10. Previously, we have eliminated weak signals by thresholding. We followed the same procedure to choose strong signals for computing CBE, which is shown in Fig. 5.11.

CBE from selected signals in Fig. 5.11 is close to prediction. Again, the threshold, which was $10dB$ less than histogram mode, was chosen by try and error. Although thresholding helps to reduce effect of "outliers", it is not the optimal way to do so. It reduces the number of samples in the calculation and may throw away samples that are not outliers. Robust reduction of noise-induced spurious CBE depends on increasing SNR. In fact, as shown in Fig. 5.8, CBE computed from experiment NL002 is close to the prediction when SNR is higher than $40dB$. Therefore, the capability of increasing SNR, as illustrated in this section, is significant for reducing spurious CBE caused by noise.

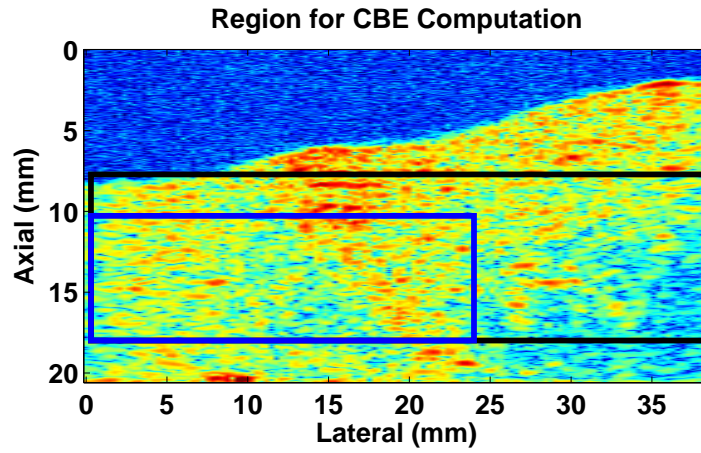


Figure 5.9: Tissue regions from which CBE was computed in experiment NL002. The black rectangle is the region normally used. The blue rectangle is the qualitatively-selected strong signal region.

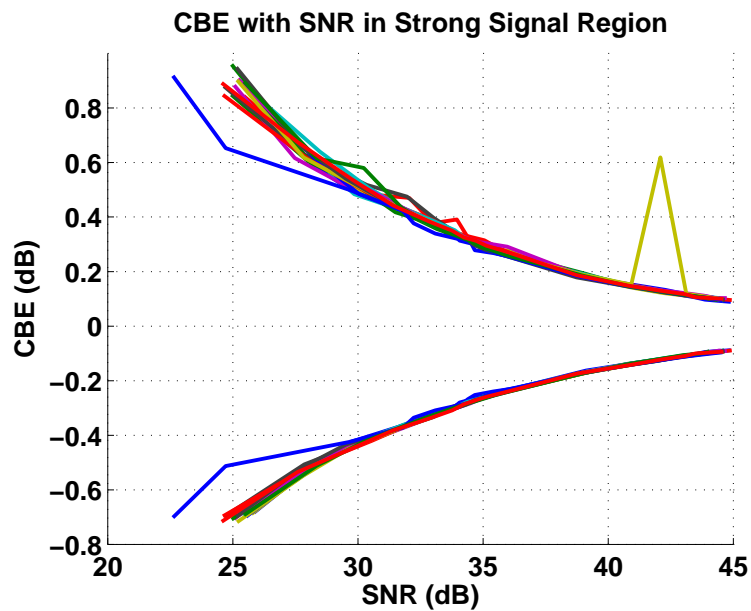


Figure 5.10: Variation of CBE with SNR in the strong signal region for all 17 loops of null experiment NL002. This region is shown as the blue rectangle in Fig. 5.9.

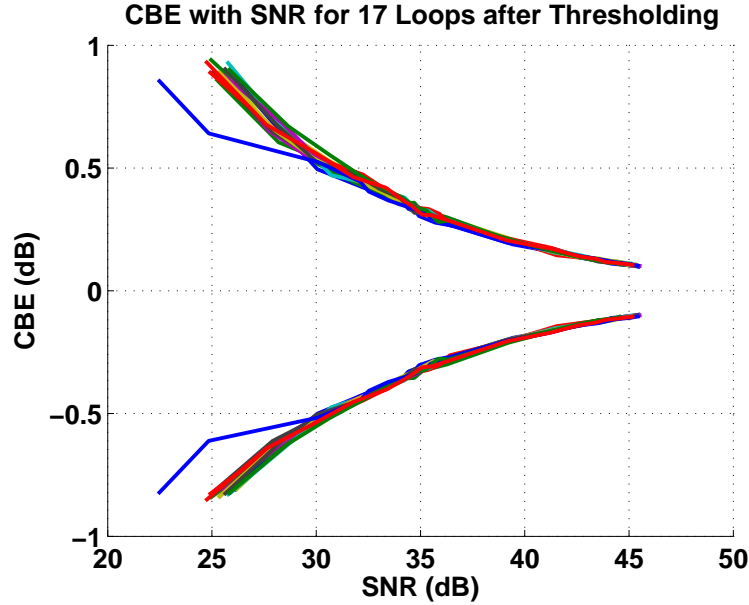


Figure 5.11: Variation of CBE with SNR from signals selected by thresholding in null experiment NL002.

Inter-loop CBE

We have demonstrated that, for our imaging system, noise-induced spurious CBE can be reduced by averaging frames in a loop. Recall that, in heating experiments, CBE is computed between images obtained at different temperatures. Correspondingly, we wish to inspect the CBE between frames of different loops, denoted as inter-loop CBE, in the null experiment.

Inter-loop CBE was computed for both single frames and averaged frames. For single frames, the first frames from loop2-17 and the second frame from loop one were compared to the first frame of loop1. For averaged frames, we averaged the first and second half of each loop. Hence, there are two averaged frames for each loop. The first averaged frames from loop2-17 and the second averaged frame from loop one were compared to the first averaged frame of loop one. According to the results of Chapter 3, we expected to see non-zero inter-loop CBE from single frames, which should be invariant with time and can be reduced by signal averaging. Inter-loop CBE from the averaged frames was expected to be close to $0.1 \sim 0.15dB$, as shown by the intra-loop CBE when seventy frames were averaged.

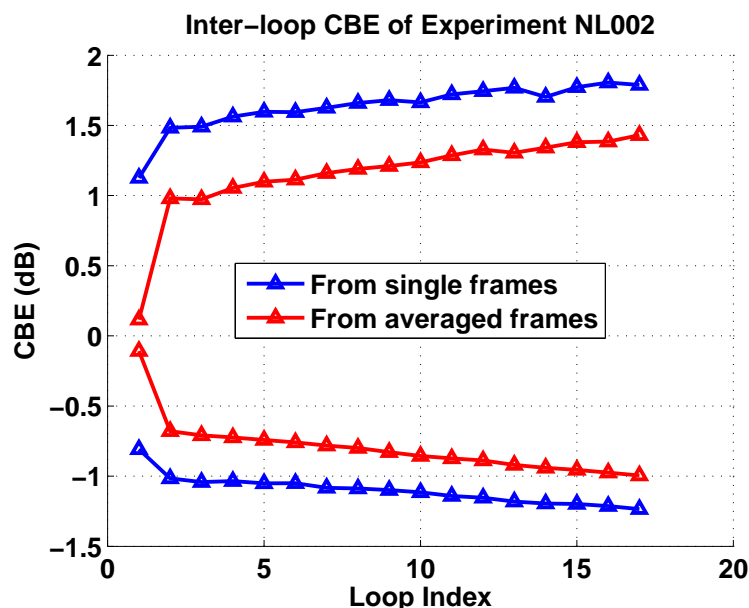


Figure 5.12: Inter-loop CBE from individual and averaged frames of null experiment NL002.

Contrary to our expectation, inter-loop CBE's shown in Fig. 5.12 are not invariant as the intra-loop CBE, but increase monotonically with loop number, i.e., with time. In addition, magnitude of inter-loop CBE from averaged frames was not reduced to $0.1 \sim 0.15dB$ as the intra-loop CBE. Because we have shown that SNR can be increased by averaging frames for all loops, the lack of expected reduction in inter-loop CBE of averaged images presumably results from changes in the backscattered signals between loops. The monotonic variation in inter-loop CBE implies that changes in the signals were systematic.

In order to check if signals changed over time without heating, we took the difference between the first frames in loop 17 and loop 1. The envelope of the difference image is shown in the upper part of Fig. 5.13. The shape of the tissue is clearly depicted in the image, which indicates that there was a difference between the backscattered signals in loop 17 and loop 1. As a reference, we also took the difference between the last and first frame of loop 1, whose envelope is shown in the lower part of Fig. 5.13. It can be seen that the difference between frames within a loop contains mostly noise, that is, there was almost no change in the backscattered signal within a loop.

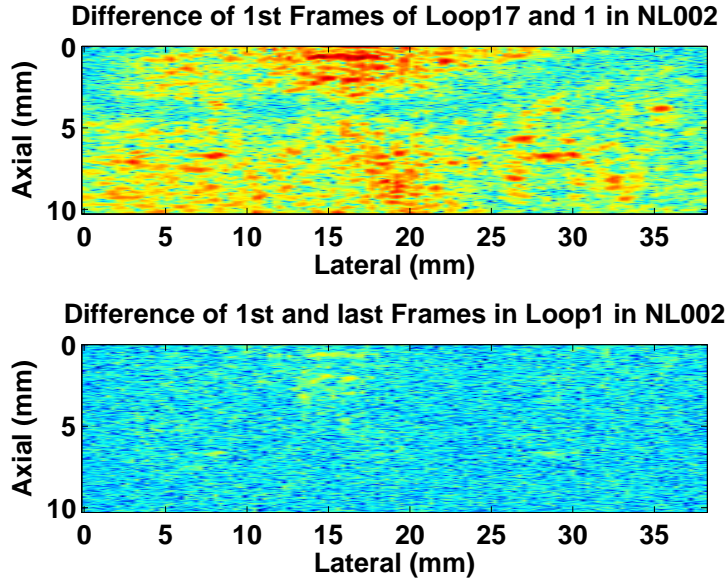


Figure 5.13: Upper: Difference between the first frames in loop 17 and loop 1, which shows changes in backscattered signals over loops. Lower: Difference between the last and first frames in loop 1, which shows that little change occurred in backscattered signals within individual loops.

Although there was $0.2^{\circ}C$ change in the tissue temperature, it was not large enough to produce the observed increase of $0.4dB$ in PCBE. The change in signals among loops could be caused by non-thermal factors. A possible explanation is that backscatter properties of the tissue, such as its density, changed when it is left in water, such that its backscatter properties varied during the experiment. To examine this hypothesis, a null experiment, NL004, was conducted during which turkey breast was left in Ringer's solution, with 0.9% sodium chloride by volume, to prevent change in the tissue. Inter-loop CBE was computed as for NL002 as shown in Fig. 5.14.

Fig. 5.14 shows that inter-loop CBE from experiment using Ringer's solution has similar behavior as the previous results from NL002. It still increased monotonically and cannot be reduced to $0.1 \sim 0.15dB$. The absolute value of CBE is about $0.4dB$ less than that in the previous experiment, because the SNR of this experiment was about $5dB$ higher than before, which led to approximately $0.4 - 0.5dB$ decrease in CBE as illustrated in Fig. 3.1. It again proved that increasing SNR will reduce spurious CBE. However, the change in the tissue backscatter property cannot be prevented using Ringer's solution.

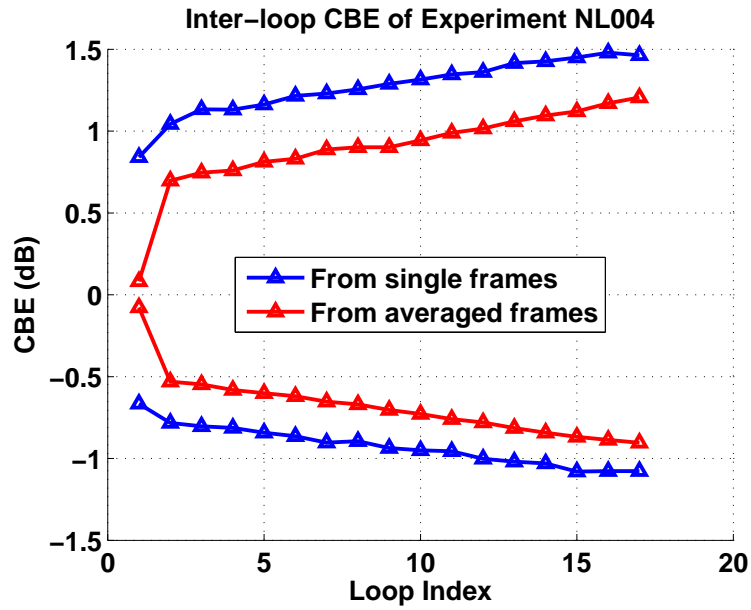


Figure 5.14: Inter-loop CBE from individual and averaged frames of null experiment NL004 using Ringer's solution.

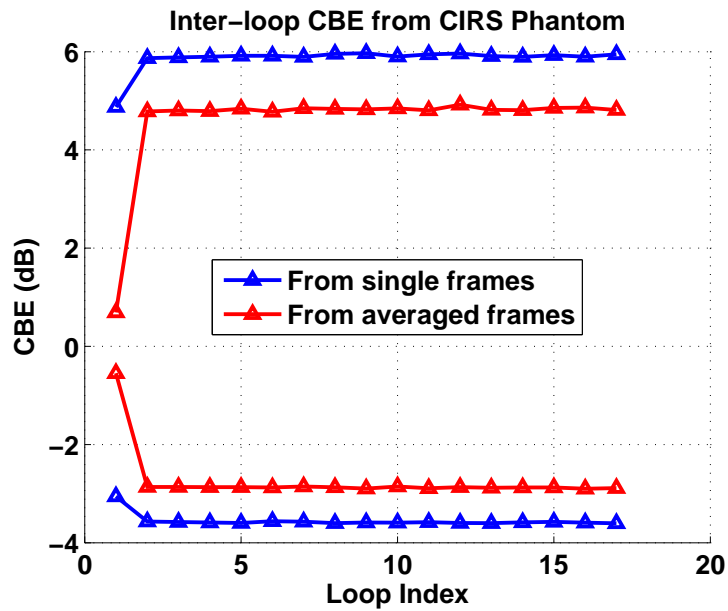


Figure 5.15: Inter-loop CBE from individual and averaged frames of null experiment NL009 using a CIRS phantom.

In order to eliminate the effect of the change in tissue property, we repeated the previous null experiment using a CIRS ultrasound phantom, model 054. The phantom was sealed in a housing and sat at room temperature for hours. Gel was used as coupling medium. As shown in Fig. 5.15, inter-loop CBE from CIRS phantom was consistent during the experiment and thus confirmed that the monotonic increase of inter-loop CBE from turkey breast resulted from the change in tissue backscatter property. Notice that, inter-loop CBE still cannot be reduced as intra-loop CBE can by averaging signals. This condition indicates there were still changes in the backscattered signal. Since these change did not come from the phantom, we believe it was caused by the imaging system.

Noise is a major source of error in CBE computation and temperature estimation. In this section, we showed that noise effects can be reduced by signal averaging. Since SNR in the image can be manipulated by varying the number of frames in averaging, it is possible for us to maintain all experiments at the same SNR. However, it was also found that signals may change due to the imaging system and the variation of tissue. Since living tissue stays in a stable environment, its backscatter property varies little without temperature change. The later problem may not happen in clinical applications. For the change caused by the imaging system, it may require modification of the instrument, which requires more resource and cooperation with the instrument provider.

5.2 Experimental Verification of Motion Compensation

Previously, we have shown that motion induced spurious CBE in simulated images can be reduced using our motion estimation and compensation algorithms. Performance of motion compensation, in terms of residual spurious CBE after compensation, can be improved by choosing appropriate interpolation approach or increasing the sampling rate during image transformation. In this section, we verify these results using real images of tissue from experiments. Since true motion is unknown in heating experiment, we conducted null experiments. Motion was introduced by moving

the transducer in both axial and lateral directions so that true motion in images was known.

5.2.1 Null Experiments with Motion

As in the null experiment described in preceding section, the Terason 3000 imaging system was used to acquire 17 loops of 2D frames of turkey breast, corresponding to 17 temperatures in heating experiments. The number of frames in each loop was determined automatically by Terason according to frame size and frame rate. The tissue specimen was fixed in a holder and left in de-ironized, de-gased water for 3 hours, such that both water and tissue reached room temperature. Motion was introduced between adjacent loops by moving the transducer in $30\mu m$ steps in both axial and lateral directions for a total shift of $0.48mm$ in each direction over 17 loops. This amount of motion covered the range observed in heating experiments. Fig. 5.16 shows the first frame of the loops with shifts of 0, 0.24 and $0.48mm$.

Before taking the images with motion, a set of 17 loops was acquired without changing transducer position. Therefore, there was no motion in the images of this set. CBE between each loop and the first loop was computed as the reference CBE. As discussed in previous section, the reference CBE was not zero due to noise, tissue degradation etc. CBE computed from the image set with motion was computed after motion compensation and compared to the reference to evaluate the performance of the motion compensation algorithm. Fig. 5.17 shows reference CBE measured from single frames. As discussed before, the jump in CBE curves was due to noise and signal changes caused by the Terason system. Variation caused by tissue degradation was small ($< 0.1dB$) during data acquisition which took only 5 minutes.

5.2.2 Motion Compensation and Spurious CBE Reduction

CBE from Single Frames

In order to evaluate our algorithms at the original SNR, which is $34dB$, we first estimated and compensated for motion in single frames, i.e., between the first frame

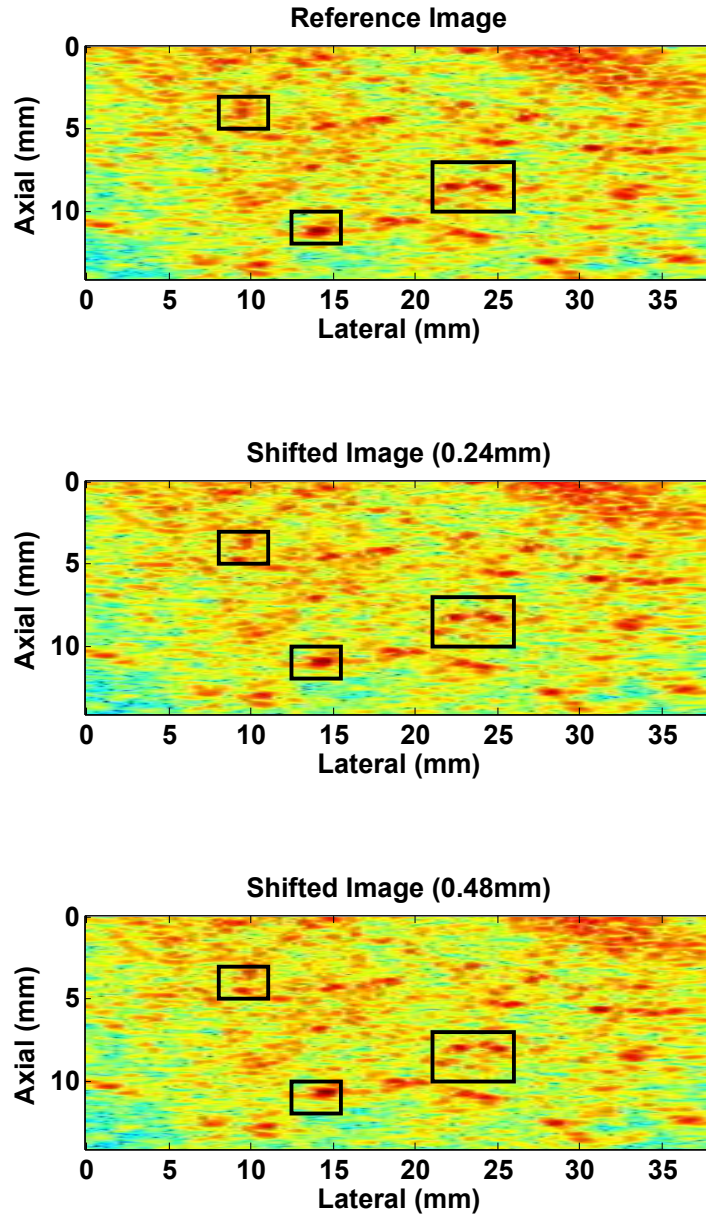


Figure 5.16: Images with motion from experiment NL012. Top: image without motion. Center: image shifted by 0.24mm . Bottom: image shifted by 0.48mm . Shifts were upwards and to the right.

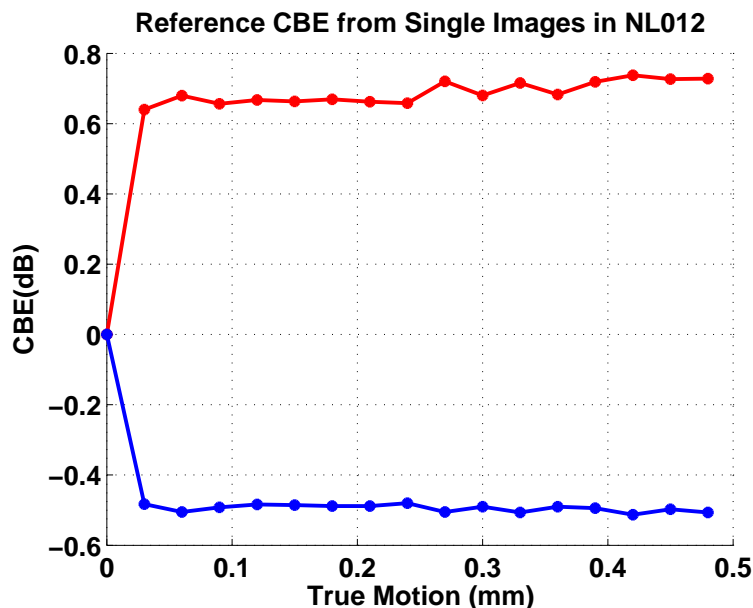


Figure 5.17: Reference CBE from single frames in experiment NL012.

of loop 2-17 and that of loop 1 (reference loop). Cumulated error in estimation was avoided by comparing loop 2-17 to loop 1. Motion compensation for images at higher SNR from averaged frames is considered in the succeeding section. Images with motion were compensated with cubic interpolation. Estimated motion was compared to the true motion and the error is shown in Fig. 5.18, which is up to $40\mu m$ in the axial and $50\mu m$ in the lateral directions, respectively. To see if this amount of error in motion estimation is acceptable, we first looked at compensated images in Fig. 5.19 corresponding to those in Fig. 5.16.

No obvious motion appears in Fig. 5.19, indicating that error in motion estimation does not produce visible motion in compensated images. However, our goal is to reduce motion induced spurious CBE. Therefore, we computed CBE from images before and after motion compensation as shown in Fig. 5.20.

As seen in the above figure, spurious CBE induced by motion was reduced, but the residual spurious CBE after motion compensation is still $0.75 - 1dB$. Two phenomena should be noted. First, CBE before motion compensation converges to some limit that is larger than what we saw in the previous chapter for rigid motion. This

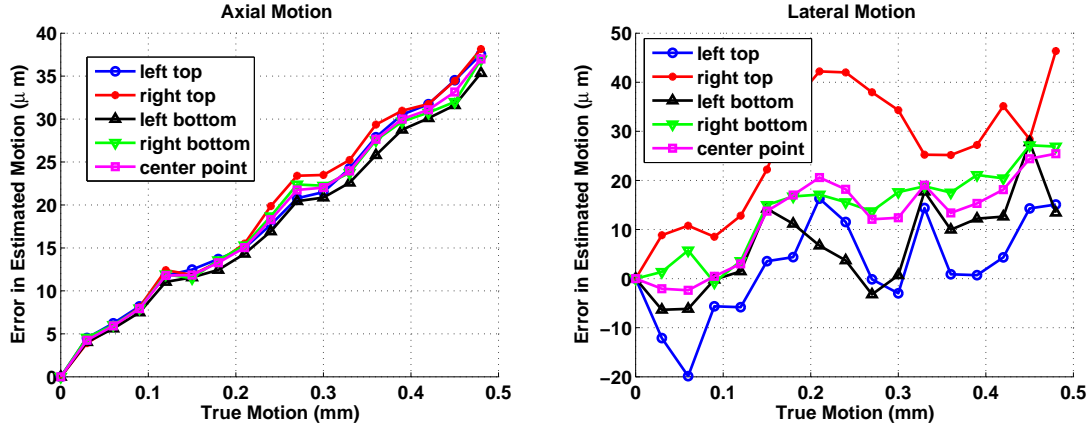


Figure 5.18: Error in motion estimation in experiment NL012 with cubic interpolation. Left: Axial direction. Right: Lateral direction.

difference occurs because the previous result was obtained assuming uniformly distributed scatterers and Rayleigh signals, but current results were from non-uniformly distributed scatterers and non-Rayleigh signals. Second, the residual spurious CBE did not increase monotonically, but showed some kind of "period". This period is related to the cubic interpolation and the experimental protocol. Recall that, in the preceding chapter, we showed that cubic interpolation did not work well when shift was not an integer multiple of the sample interval, in this case, around half a sample. In this experiment, motion between adjacent images was consistent and therefore accumulated motion was close to or far away from a multiple of the sample interval. Thus, CBE after compensation varied "periodically".

In Chapter 3, motion compensation can be improved by using spline interpolation. Here, we repeated motion compensation for NL012 with spline interpolation. Motion estimation error and residual spurious CBE are plotted in Figs. 5.21 and 5.22, respectively.

Comparing results in Fig. 5.21 to that in Fig. 5.18, it is seen that error in motion estimation did not vary periodically by using spline interpolation for image transformation. In addition, residual spurious CBE with spline interpolation shown in Fig. 5.22 is much less than that with cubic interpolation in Fig. 5.20. This result verifies that, the method of image transformation has significant impact on spurious CBE reduction. This conclusion is consistent with the conclusion made in the

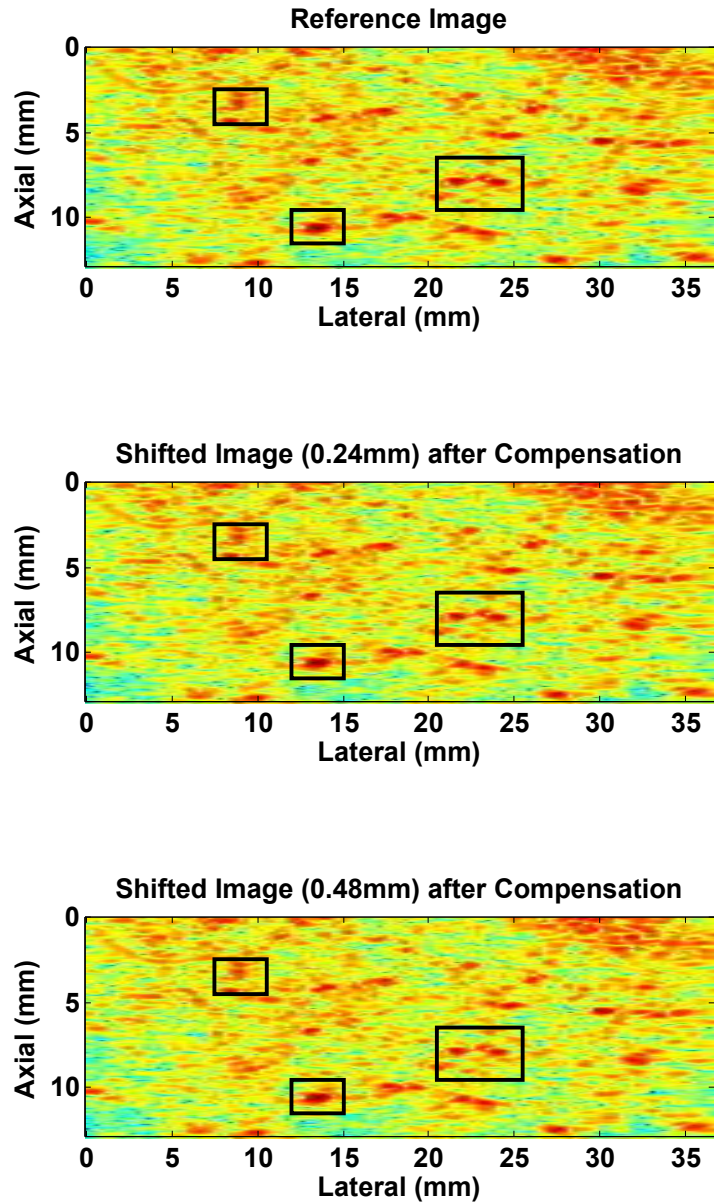


Figure 5.19: Motion compensated images from experiment NL012. Top: image without motion. Center: image shifted by 0.24mm . Bottom: image shifted by 0.48mm . Shifts were upwards and to the right.

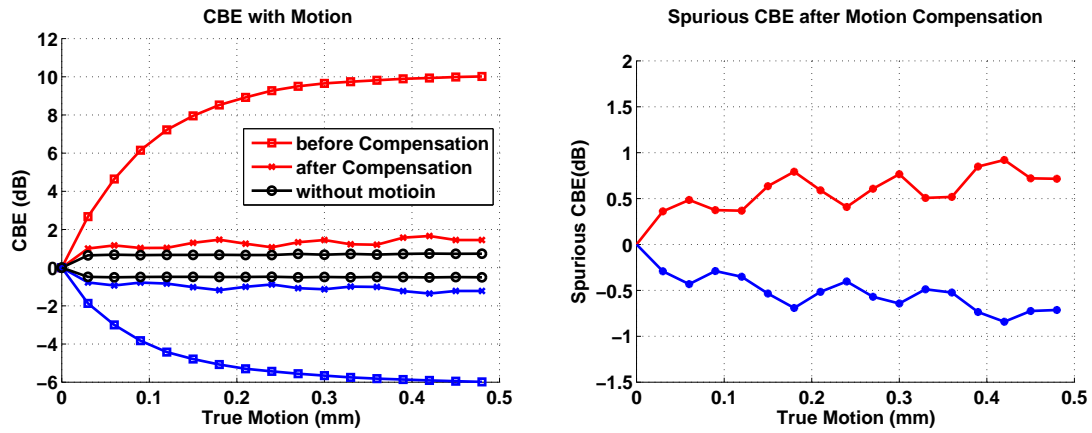


Figure 5.20: CBE in experiment NL012 with cubic interpolation. Left: CBE before and after motion compensation and reference CBE. Right: Difference between CBE after motion compensation and reference CBE.

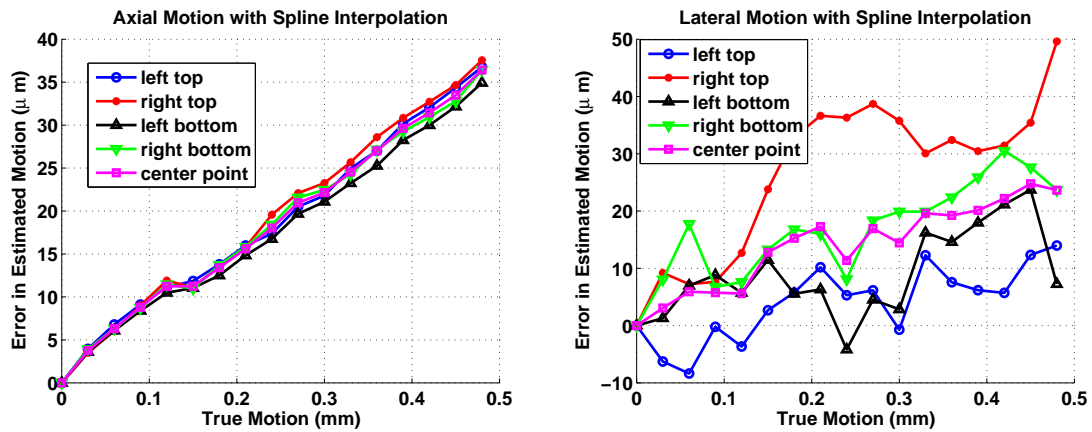


Figure 5.21: Error in motion estimation in experiment NL012 with spline interpolation. Left: Axial direction. Right: Lateral direction.

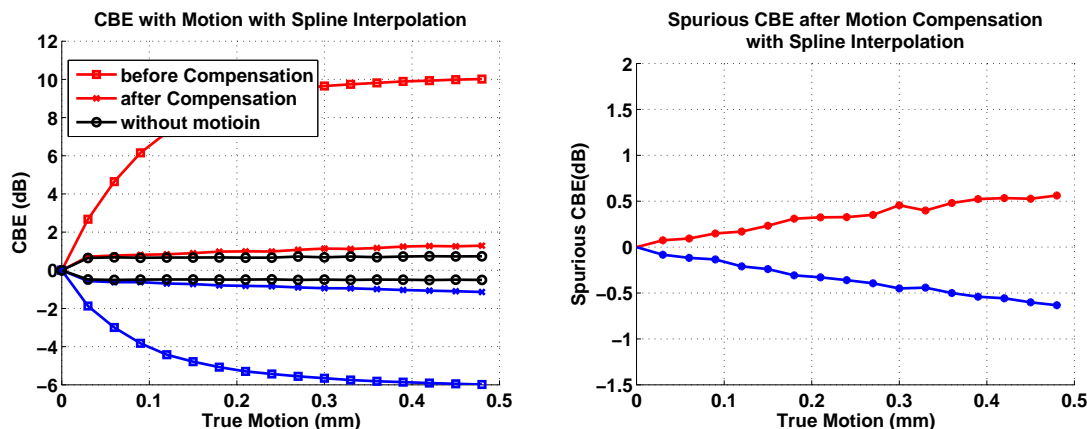


Figure 5.22: CBE in experiment NL012 with spline interpolation. Left: CBE before and after motion compensation and reference CBE. Right: Difference between CBE after motion compensation and reference CBE.

previous simulation studies. As discussed in the simulation studies, instead of using spline interpolation, the performance of image compensation can also be improved by increasing the sampling rate. Since the hardware settings of the Terason imaging system can not be changed, we up-sampled the original images and applied motion estimation and compensation with cubic interpolation. Up-sampling was first done in axial direction. Error in motion estimation and spurious CBE after compensation are shown in Figs. 5.23 and 5.24, respectively. Again, the estimation of lateral motion was slightly better than the result with spline interpolation. The residual spurious CBE was slightly less but close to the result with spline interpolation.

Similar to the results in the simulations, performance of spurious CBE reduction with up-sampling in the axial direction is close to that found using spline interpolation. We further up-sampled images in both axial and lateral directions. Error in motion estimation and the spurious CBE after compensation are shown in Figs. 5.25 and 5.26, respectively.

The above results confirm that our motion estimation and compensation algorithms are able to reduce motion-induced spurious CBE from images of real tissue specimens. In addition, performance of motion-compensation algorithms can be improved either by using spline interpolation or up-sampling the data. As shown in the simulation

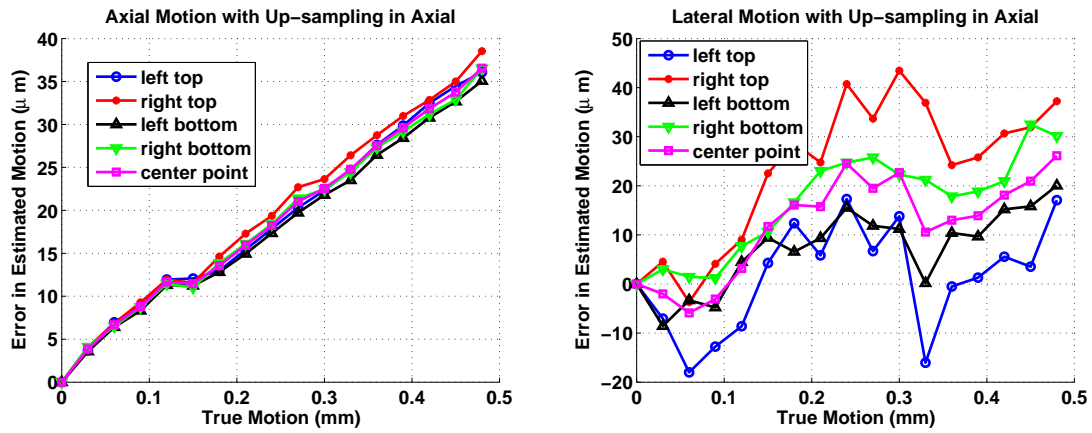


Figure 5.23: Error in motion estimation in experiment NL012 with up-sampling axially. Left: Axial direction. Right: Lateral direction.

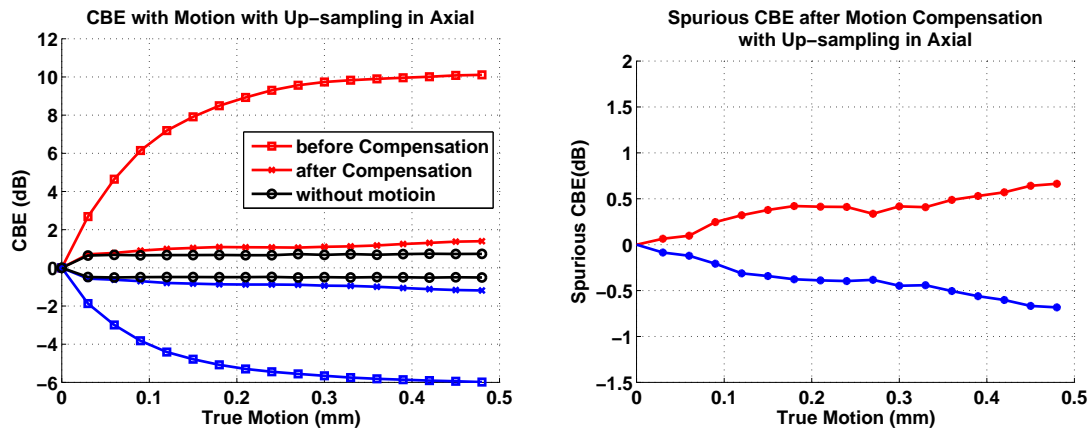


Figure 5.24: CBE in experiment NL012 with axial up-sampling. Left: CBE before and after motion compensation and reference CBE. Right: Difference between CBE after motion compensation and reference CBE.

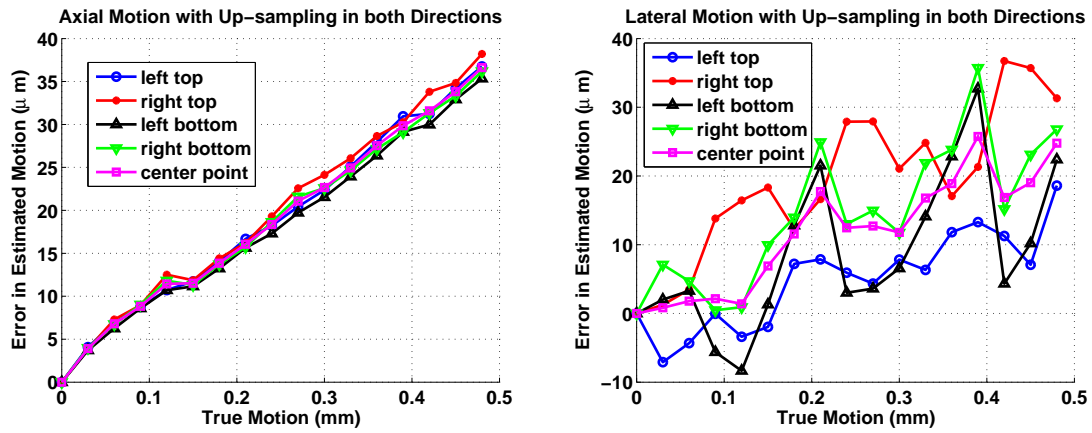


Figure 5.25: Error in motion estimation in experiment NL012 with up-sampling in both directions. Left: Axial direction. Right: Lateral direction.

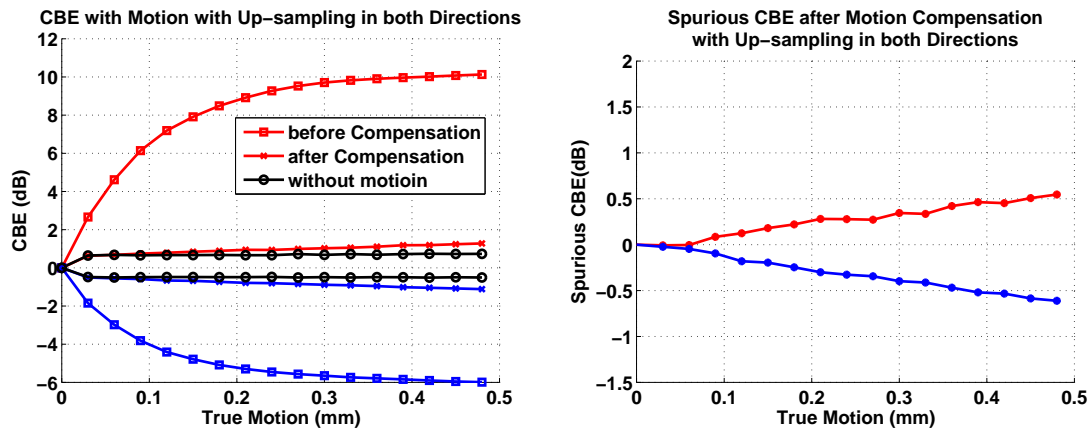


Figure 5.26: CBE in experiment NL012 with up-sampling in both directions. Left: CBE before and after motion compensation and reference CBE. Right: Difference between CBE after motion compensation and reference CBE.

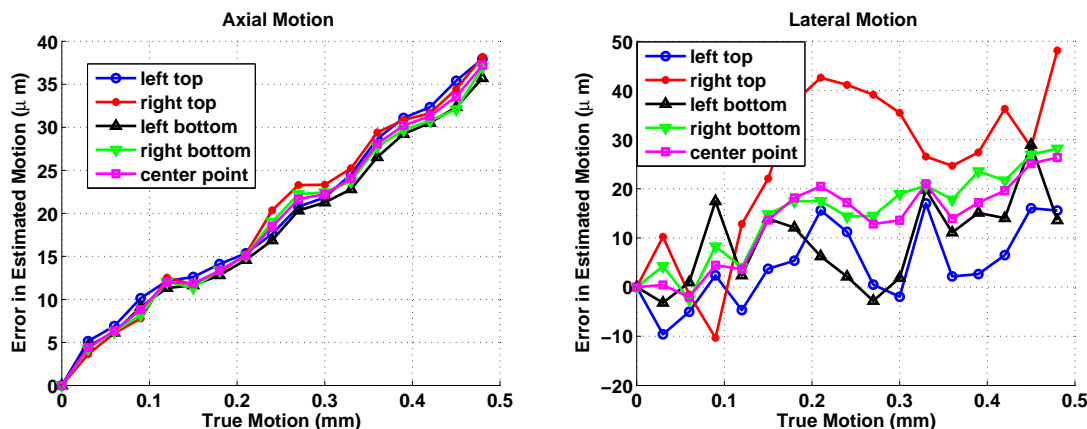


Figure 5.27: Error in motion estimation from averaged frames in experiment NL012 with cubic interpolation. Left: Axial direction. Right: Lateral direction.

study, the performance of spurious CBE reduction algorithms over small temperature changes that cause less motion, is more important than for large temperature changes. The results in this section show that, by choosing appropriate interpolation methods or by up-sampling the data, spurious CBE for small motions can be essentially removed.

CBE from Averaged Images

In order to see the effect of SNR on motion estimation and compensation, we averaged 78 frames (half a loop) in each loop. SNR was increased by about 19dB by averaging 78 frames, which is consistent with the result in Chapter 3. Motion was estimated and compensated and CBE computed from averaged frames as it was for single frames. Error in motion detection with cubic interpolation in Fig. 5.27 was similar to the error from single frames. This result confirms, as in simulation studies, SNR does not have significant impact on motion estimation.

Since reference CBE for single and averaged frames were different, instead of comparing residual spurious CBE, we compared CBE after motion compensation without subtracting the reference CBE. Results from different interpolation approaches and up-sampling methods are shown in Figs. 5.28, 5.29, 5.30 and 5.31.

In all situations, further spurious CBE reduction can be obtained by averaging frames, that is by increasing SNR. The improvement, about $0.1 - 0.15\text{dB}$, was however not

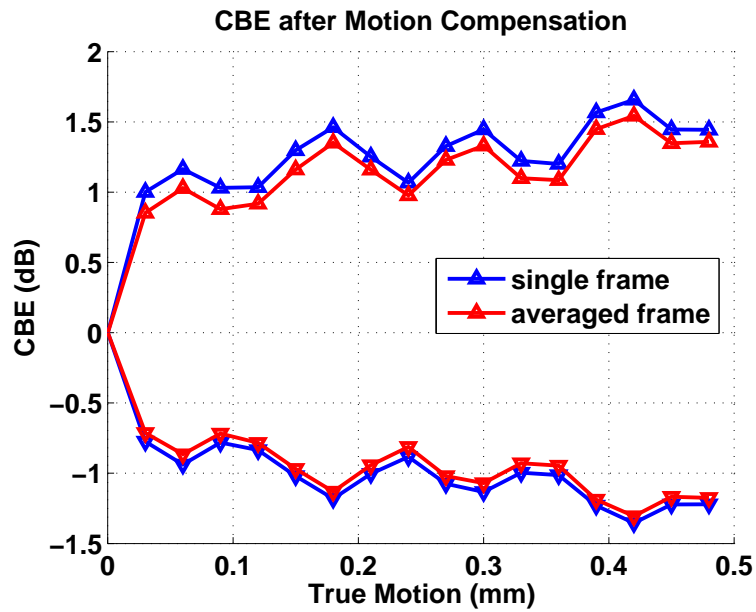


Figure 5.28: Residual spurious CBE from averaged frames of NL012 with cubic interpolation.

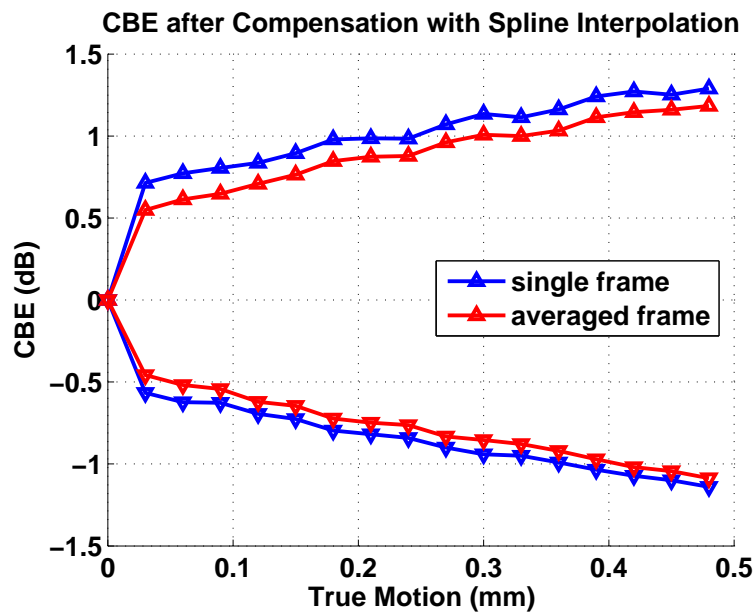


Figure 5.29: Residual spurious CBE from averaged frames of NL012 with spline interpolation.

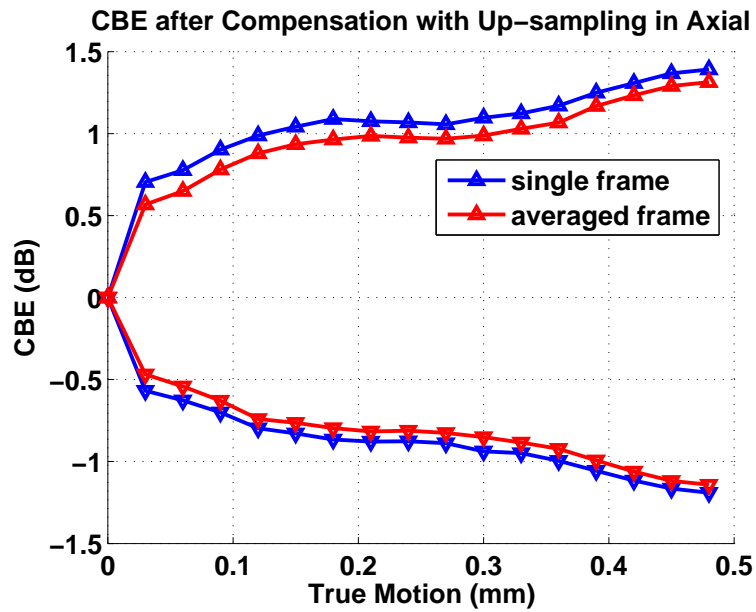


Figure 5.30: Residual spurious CBE from averaged frames of NL012 with axial up-sampling.

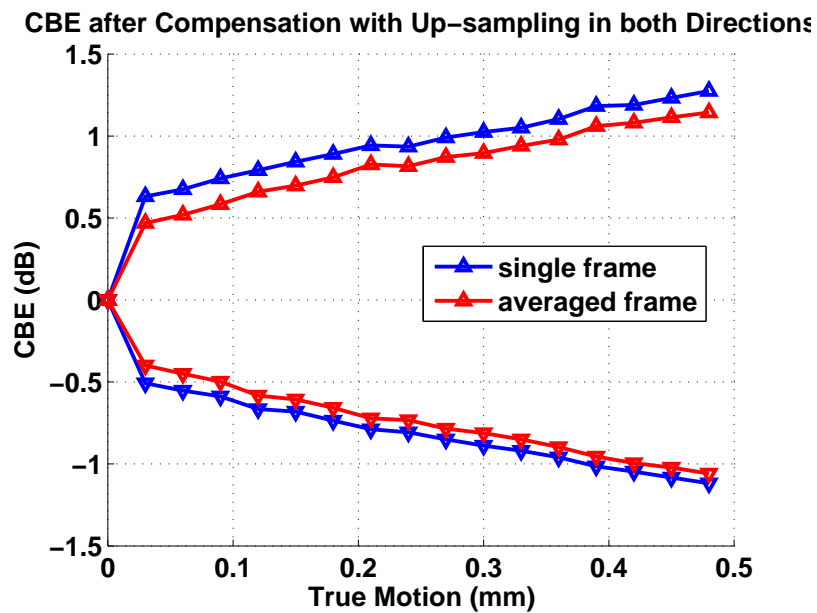


Figure 5.31: Residual spurious CBE from averaged frames of NL012 with up-sampling in both directions.

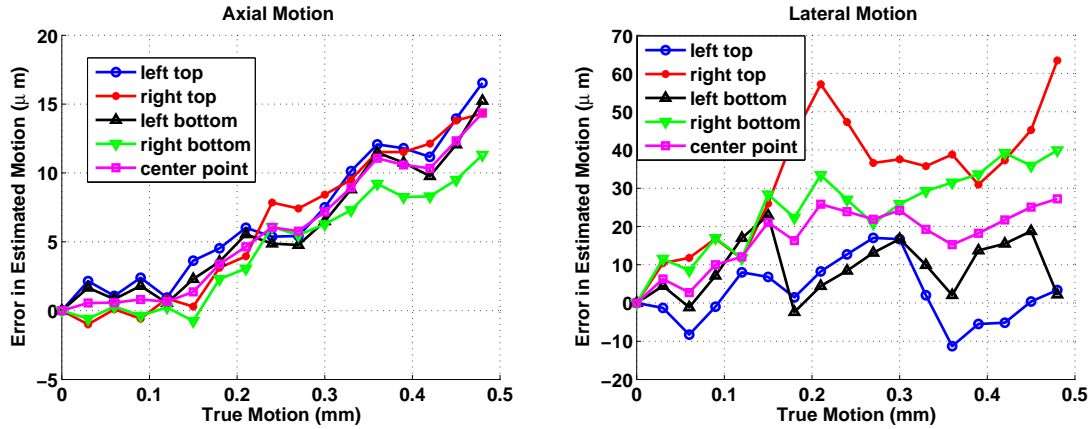


Figure 5.32: Error in motion estimation in experiment NL012 with cubic interpolation at $37^{\circ}C$. Left: Axial direction. Right: Lateral direction.

significant as we saw in the noise reduction study. This result is again because, although SNR is increased by averaging frames, the signal over loops may change slightly due to the Terason imaging system and thus result in spurious CBE. This change can be regarded as a kind of noise with properties that cannot be reduced by signal averaging.

Experiment at $37^{\circ}C$

The above experiment was conducted at room temperature. We also conducted an experiment at $37^{\circ}C$. The tissue sample was heated to $37^{\circ}C$ in a water tank as in the heating experiments. Water temperature was held at $37^{\circ}C$ for 20 minutes to ensure thermal equilibrium in the tissue. The error in motion estimation with cubic interpolation is shown in Fig. 5.32. Estimation error in the axial direction was up to $15\mu m$, which is less than the result at room temperature, while the error in the lateral direction was about $10\mu m$ larger than at room temperature. Nevertheless, the residual spurious CBE in Fig. 5.33 is close to the result in Fig. 5.20.

Figs. 5.34 and 5.35 show the results of motion estimation and spurious CBE reduction with spline interpolation. As seen at room temperature, motion detection was slightly better than the estimation with cubic interpolation, but the residual spurious CBE was much less. The residual spurious CBE with spline interpolation was also close to that obtained at room temperature.

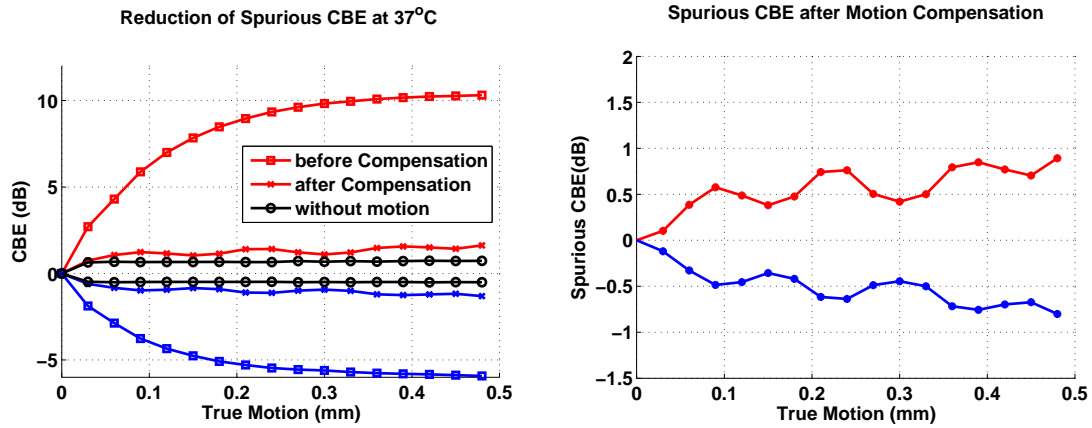


Figure 5.33: CBE in experiment NL012 with cubic interpolation at $37^{\circ}C$. Left: CBE before and after motion compensation and reference CBE. Right: Difference between CBE after motion compensation and reference CBE.

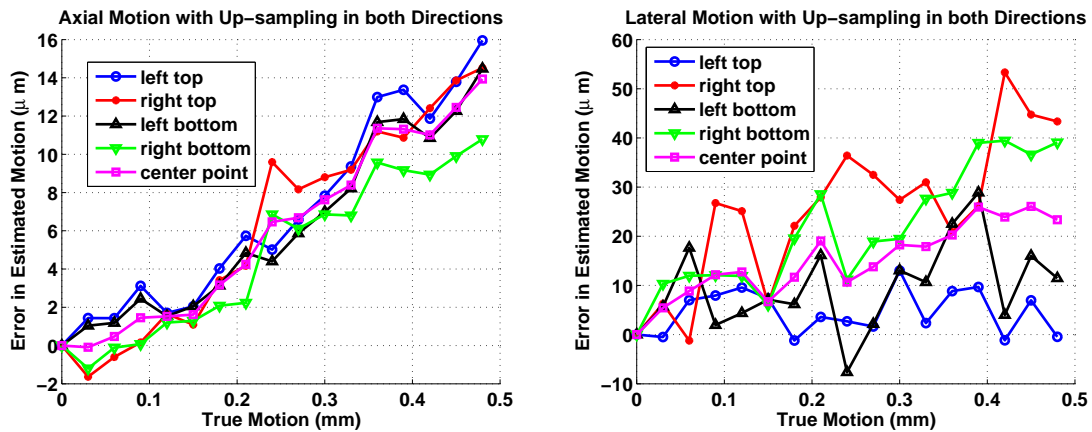


Figure 5.34: Error in motion estimation in experiment NL012 with up-sampling in both directions at $37^{\circ}C$. Left: Axial direction. Right: Lateral direction.

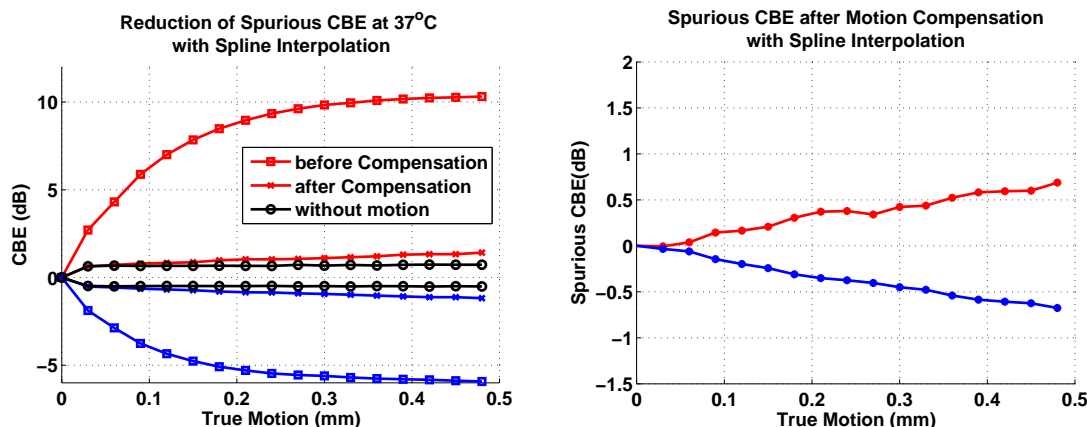


Figure 5.35: CBE in experiment NL012 with spline interpolation at $37^{\circ}C$. Left: CBE before and after motion compensation and reference CBE. Right: Difference between CBE after motion compensation and reference CBE.

Reduction of spurious CBE with up-sampling in both axial and lateral directions is shown in Figs. 5.36 and 5.37. Up-sampling did not produce a significantly different result from that at room temperature.

5.3 Summary and Conclusions

In this chapter, we applied the approaches to reducing noise and motion effects developed in Chapter 3 to experimental data. The results verified that noise effects can be reduced by signal averaging and thresholding as in the simulations. Spurious CBE caused by tissue degradation and variation in the imaging system, however, remain.

Our motion compensation algorithms were proved to be able to correct motion in real images and reduce motion-induced spurious CBE. We also showed for experimental data that motion compensation and spurious CBE reduction can be improved by choosing appropriate interpolation methods or by up-sampling. This conclusion verified the observations of the simulation study.

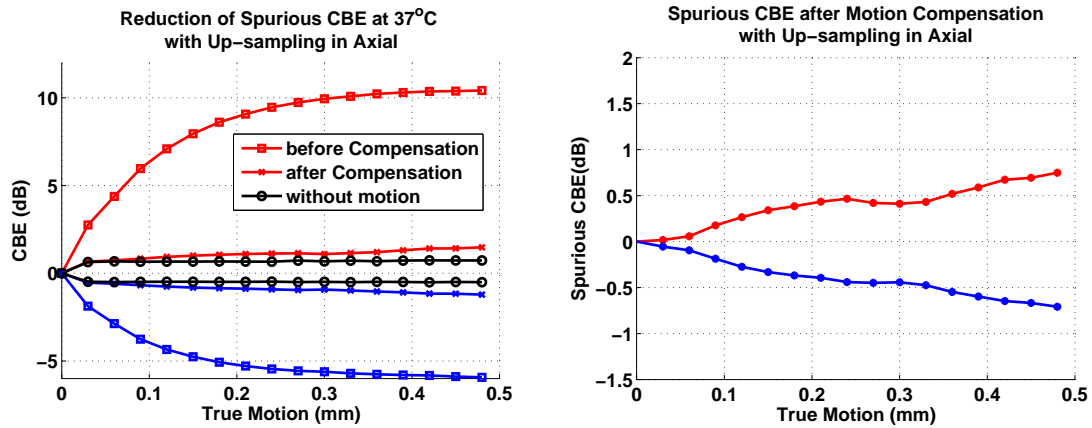


Figure 5.36: CBE in experiment NL012 with axial up-sampling at $37^{\circ}C$. Left: CBE before and after motion compensation and reference CBE. Right: Difference between CBE after motion compensation and reference CBE.

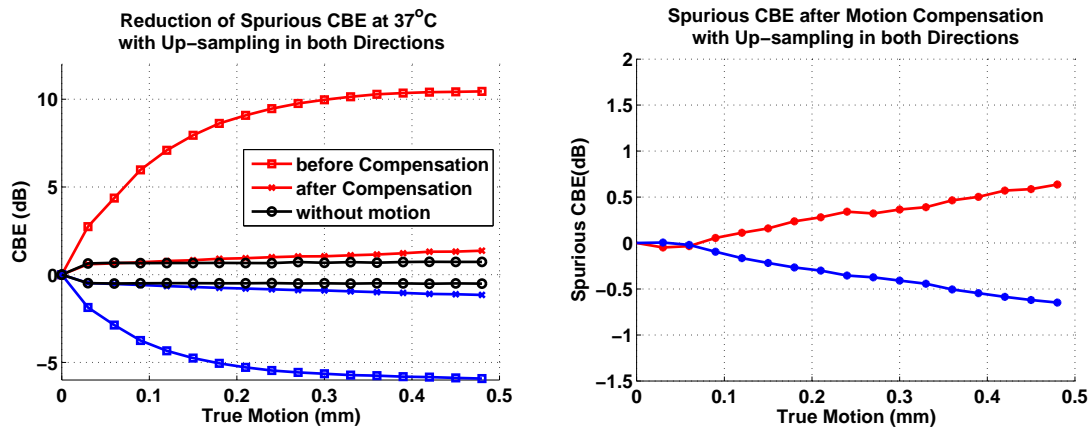


Figure 5.37: CBE in experiment NL012 with up-sampling in directions at $37^{\circ}C$. Left: CBE before and after motion compensation and reference CBE. Right: Difference between CBE after motion compensation and reference CBE.

Chapter 6

Framework for Temperature Imaging with CBE

In our initial work, a theoretical model was developed for CBE from single scatterers, which predicted increasing or decreasing of CBE depending on scatterer type [92]. Monotonic variation of CBE measured in various types of tissue in 1D and 2D *in-vitro* experiments confirmed the prediction of the model. CBE was computed by taking the ratio of images at current and reference temperatures. It was characterized as positive CBE (PCBE) and negative CBE (NCBE), which are the mean of the ratio over values larger than and less than 1, respectively. Although these results showed that CBE is a potential parameter for temperature imaging and CBE computation was straightforward, this procedure was somewhat *ad hoc* in the sense of lacking mathematic formality.

In this chapter, we model the problem of temperature imaging via a probabilistic framework and formalize computational methods of CBE. Based on the framework, we developed procedures for more careful calculation of CBE and thus better temperature estimation under certain conditions. This development was based on the extension of the well known random phasor-sum representation of ultrasonic backscattered signals to encompass the thermal dependent tissue properties. In the development of the framework, we assume changes in backscattered signals are temperature dependent only.

6.1 Modeling the Problem of Temperature Imaging

In this section, we model the problem of temperature imaging as estimating temperature from random processes resulting from thermal changes in ultrasonic backscattered signals. The marginal and joint distributions associated with the random processes are discussed.

6.1.1 Random Phasor Sum Model for Temperature Dependent Signals

Ultrasonic signals result from constructive or destructive superposition of scattering within a resolution cell of the transducer [110, 50], and may be approximated by a linear image formation model [100]

$$i(\mathbf{r}) = h(\mathbf{r}) * q(\mathbf{r}) \quad ,$$

where \mathbf{r} is the coordinate vector of the position, $h(\mathbf{r})$ is the point spread function of the imaging system, $q(\mathbf{r}) = \sum_{k=1}^N q_k \delta(\mathbf{r} - \mathbf{r}_k)$ is the discrete tissue model and q_k 's are the reflectivity of individual scatterers. The resulting complex envelope representation of the ultrasound signal is a random phasor sum [100]

$$i(\mathbf{r}) = \sum_{k=1}^N A_k e^{j\phi_k} \quad , \quad (6.1)$$

where i is the complex envelope of the signal, N is the number of scatterers, A_k and ϕ_k are the magnitude and phase of element phasor associated with each scatterer. A_k is determined by the reflectivity, q_k , and the position of k^{th} scatterer. ϕ_k relates only to the scatterer position. In this study, we assumed N is large and ϕ_k is uniformly distributed over $[0, 2\pi]$. Motion in the images due to the change of speed of sound and tissue movement may cause variation of ϕ_k . In our theoretical analysis using the random phasor sum model, we assumed that variation in ϕ_k can be compensated by our motion compensation algorithm.

According to our CBE model for single scatterers, the reflectivity of individual scatterers, q_k is temperature dependent and the discrete tissue model can be written as [92, 7, 103]

$$q(\mathbf{r}, T) = \sum_{k=1}^N q_k(T) \delta(\mathbf{r} - \mathbf{r}_0) \quad , \quad (6.2)$$

where T is the temperature. Since A_k is proportional to q_k , A_k is also a function of temperature. The random phasor sum in Eq. 6.1 becomes

$$i_T(\mathbf{r}) = \sum_{k=1}^N A_k(T) e^{j\phi_k} \quad , \quad (6.3)$$

where \mathbf{r} , N are the same as in Eq. 6.1, the subscript "T" in i_T represents the temperature dependence of i , the complex envelope. Eq. 6.3 is the temperature dependent random phasor sum model for the complex envelope of ultrasonic backscattered signals. For simplicity, we drop \mathbf{r} in the remaining part of this dissertation.

Because the scatterers are randomly distributed over the tissue region, A_k , ϕ_k and thus i_T are also random [100]. In addition, since i_T is temperature dependent, it can be represented as a collection of random variables indexed by temperature, resulting in random processes. In our case we can obtain ultrasonic RF signals from our Terason imaging system. Envelope detected images, i_{en} , can be computed from i_{rf} using the Hilbert transform. Both i_{rf} and i_{en} can be represented by random processes.

Random processes are statistically characterized by finite dimensional joint distributions, $p(x_{T_0}, x_{T_1}, \dots, x_{T_n})$, where x can represent any of the above random processes. In this study, we tried to estimate temperature from the variation between images at current and reference temperatures. The corresponding joint distribution we were interested in was $p(x_{T_0}, x_T)$. Therefore, the problem of temperature imaging can be modeled as estimating temperature from random processes resulting from thermal changes of tissue. In the next section, we discuss the marginal and joint distributions for the RF and envelope detected images.

Because we were interested in the change in the backscattered signals, it is helpful to express i_T in a form relative to the reference signal. From the CBE model for single scatterers, A_k can be expressed relative to its value at reference temperature

by introducing a coefficient, $\beta_k(T)$. Eq. 6.3 can then be modified as

$$i_T(\mathbf{r}) = \sum_{k=1}^N \beta_k(T) A_k(T_0) e^{j\phi_k} \quad , \quad (6.4)$$

where $A_k(T_0)$ and ϕ_k are the magnitude and phase of the k th phasor at the reference temperature, and $\beta_k(T)$ represents the change of the scatterer reflectivity, with $\beta_k(T_0) = 1$. The reference temperature T_0 was chosen to be 37°C in our study.

6.1.2 Marginal and Joint Distributions of Ultrasonic Signals

In the last subsection, we modeled the problem of temperature imaging as estimating temperature from collections of random variables. Knowledge of the joint and marginal distributions of the random variables are important for studying statistical properties of ultrasonic signals. As mentioned above, we usually obtained RF signals and compute their envelopes (B-scans). Distributions for these signals are discussed below.

Because the randomness of the signal is due to the random position of scatterers, statistical properties of the signals are determined by how the scatterers are distributed. A uniform distribution of the scatterers is a common and simple assumption that leads to a simple signal model and allows for straightforward theoretical analyses. Real tissue may not satisfy this assumption, or may include additional variances. Below, we first discuss signal distributions assuming uniformly distributed scatterers, then discuss distributions of signals from real tissue.

In order to discuss distributions of the signals, it is helpful to write Eq. 6.3 in the following form

$$i_T = \sum_{k=1}^N A_k(T) e^{j\phi_k} = R + jI \quad , \quad (6.5)$$

where R and I are random variables representing real and imaginary parts of the complex envelope i_T .

Signals from Uniformly Distributed Scatterers

RF signals

RF ultrasonic signal can be expressed as [100]

$$i_{rf} = \text{Re}\{i_T e^{j2k_0 z}\} \quad , \quad (6.6)$$

where i_T is the complex envelope, k_0 is the wavenumber corresponding to the center frequency, f_0 , and z corresponds to the axis in axial direction. Details of the derivation of Eq. 6.6 can be found in [100]. From Eq. 6.5, RF signal can also be written as

$$i_{rf} = R \cos 2k_0 z - I \sin 2k_0 z \quad .$$

When scatterers are uniformly distributed over the region, R and I can be approximated by independent Gaussian random variables with zero mean and same variance [110, 81], i.e.,

$$R, I \sim N(0, \sigma^2) \quad .$$

Since R and I are independent, i_{rf} is also Gaussian with

$$E(i_{rf}) = E(R) \cos 2k_0 z - E(I) \sin 2k_0 z = 0 \quad ,$$

$$\text{Var}(i_{rf}) = E(i_{rf}^2) = \text{Var}(R) \cos^2(2k_0 z) + \text{Var}(I) \sin^2(2k_0 z) = \sigma^2 \quad .$$

Let x represents the pixel in RF images, we have

$$f_X(x) = \frac{1}{\sqrt{2\pi}\sigma} e^{-\frac{1}{2}\frac{x^2}{\sigma^2}} \quad . \quad (6.7)$$

In order to estimate temperature, we are interested in the relation between images at reference and current temperatures, T_0 and T . For simplicity, we represent RF signals at T_0 and T by x_0 and x_T with $x_0 \sim N(0, \sigma_0^2)$ and $x_T \sim N(0, \sigma^2)$ respectively. Let ρ be the correlation coefficient between x_0 and x_T . Their joint distribution is

$$f(x_0, x_T) = \frac{1}{2\pi\sigma_0\sigma\sqrt{1-\rho^2}} \exp\left[-\frac{1}{2}(x_0, x_T)\Sigma^{-1}(x_0, x_T)^T\right] \quad , \quad (6.8)$$

or

$$f(x_0, x_T) = \frac{1}{2\pi\sigma_0\sigma\sqrt{1-\rho^2}} \exp \left[-\frac{1}{2(1-\rho^2)} \left(\frac{x_0^2}{\sigma_0^2} + \frac{x_T^2}{\sigma^2} - \frac{2\rho x_0 x_T}{\sigma_0\sigma} \right) \right] , \quad (6.9)$$

where

$$\rho = \frac{E(x_0 x_T)}{\sigma_0\sigma} ,$$

and

$$\Sigma = \begin{bmatrix} \sigma_0^2 & \rho\sigma_0\sigma \\ \rho\sigma_0\sigma & \sigma^2 \end{bmatrix} .$$

Parameters σ_0 , σ and ρ can be estimated from the signals.

Envelope detected signals

The envelope detected signal (B-scans) is usually used for better visualization and was used in our computation of CBE. It may be expressed by

$$i_{en} = |i_T| = |R + jI| = \sqrt{R^2 + I^2} . \quad (6.10)$$

When R and I are independent Gaussian as described above, $R, I \sim N(0, \sigma^2)$, i_{en} is Rayleigh signal [110]. Let i_{en} be represented by random variable y . The distribution for the pixels in envelope detected images is

$$f(y) = \frac{y}{\sigma^2} e^{-\frac{y^2}{2\sigma^2}} . \quad (6.11)$$

Similar to our description of RF signals, we denote the envelope detected images at T_0 and T by y_0 and y_T , with

$$f(y_0) = \frac{y_0}{\sigma_0^2} e^{-\frac{y_0^2}{2\sigma_0^2}} ,$$

$$f(y_T) = \frac{y_T}{\sigma^2} e^{-\frac{y_T^2}{2\sigma^2}} .$$

The joint density function of (y_0, y_T) can be written in form [91]

$$f(y_0, y_T) = \frac{4y_0 y_T}{(1-r^2)\sigma_1^2\sigma_2^2} \exp \left[-\frac{1}{1-r^2} \left(\frac{y_0^2}{\sigma_1^2} + \frac{y_T^2}{\sigma_2^2} \right) \right] I_0 \left(\frac{-2r y_0 y_T}{(1-r^2)\sigma_1\sigma_2} \right) , \quad (6.12)$$

where $\sigma_1^2 = 2\sigma_0^2$, $\sigma_2^2 = 2\sigma^2$, $I_0(\cdot)$ is modified Bessel function of 0th order and r is a correlation parameter with $0 \leq r \leq 1$. Eq. 6.12 is in fact a special case of the joint probability density function of correlated Weibull random variables [13]. σ_1^2 and σ_2^2 can be estimated from y_0 and y_T . r can be estimated by [91, 13]

$$\hat{r} = \sqrt{\frac{Cov(y_0^2 y_T^2)}{\sqrt{Var(y_0^2) Var(y_T^2)}}} .$$

Distributions for Signals from Real Tissue

The assumption of uniformly distributed scatterers leads to Gaussian RF and Rayleigh envelope signal descriptions. Parameters of their density functions can be easily estimated and used for further analysis, which we will see in later sections. This assumption, however, may not be satisfied in reality.

In this study, real RF ultrasound signals backscattered from turkey breast were collected in *in-vitro* experiments. Fig. 6.1 shows the histogram of real RF signals from null experiment NL002 and estimated Gaussian distribution from the signal. The estimated distribution does not match data histogram well. By observing the data histogram, we found that the Laplace distribution, also known as bi-exponential distribution fits the histogram better as shown in Fig. 6.2.

Again, let x be the random variable representing RF signals. The density function of x is

$$f(x) = \frac{1}{\sqrt{2}\sigma} \exp\left(-\frac{\sqrt{2}|x - \mu|}{\sigma}\right) , \quad (6.13)$$

where $\mu = E(x)$ and $\sigma = Var(x)$. A possible joint distribution between two Laplace RF signals x_0 and x_T is given in [49]

$$f(x_0, x_T) = \frac{1}{\pi\sigma_0\sigma\sqrt{1-\rho^2}} K_0\left(\sqrt{\frac{2\left(\frac{x_0^2}{\sigma_0^2} - 2\rho x_0 x_T (\sigma_0\sigma) + \frac{x_T^2}{\sigma^2}\right)}{1-\rho^2}}\right) , \quad (6.14)$$

where σ_0 and σ are Laplace parameters of x_0 and x_T , ρ is a correlation coefficient, and $K_0(\cdot)$ is the Bessel function of the 3rd kind. Here, $E(x_0)$ and $E(x_T)$ are assumed

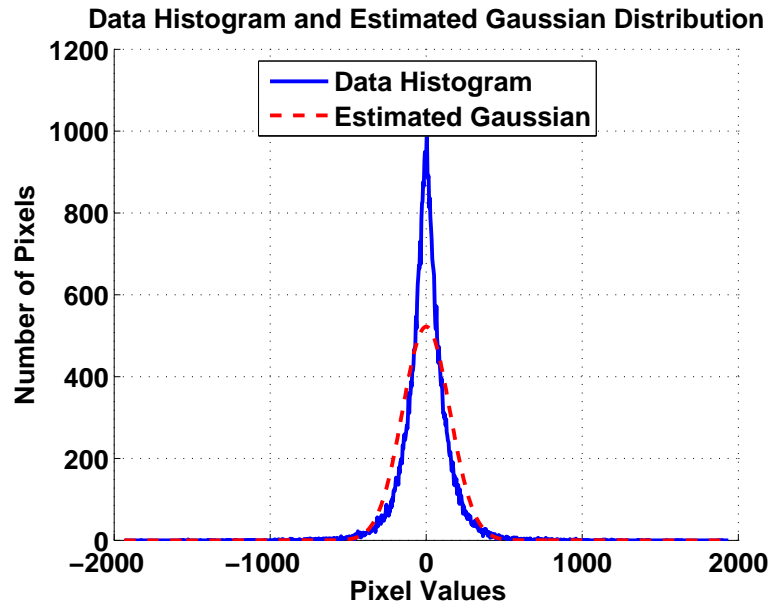


Figure 6.1: Histogram and fitted Gaussian distribution of RF signals obtained in experiment NL002. The specimen is turkey breast.

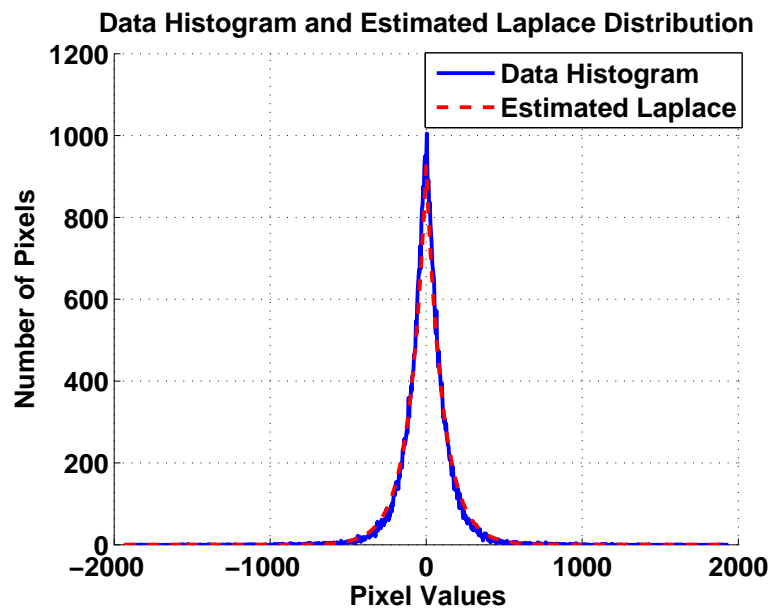


Figure 6.2: Histograms and fitted Laplace distribution of RF signals obtained in experiment NL002. The specimen is turkey breast.

to be zero according to the observed data. It is seen that the joint density function of two Laplace random variables has a complex form, which may limit its application in temperature estimation.

It was also found that the histograms of the envelope detected images from the experiment were not Rayleigh. Statistical models proposed for describing real ultrasonic signals were reviewed in the previous chapter. In this study, we found that the generalized Gamma distribution fits our data histogram. Let y be the random variable representing the envelope detected images. Then,

$$f(y) = \frac{py^{pm-1} \exp\left(-\left(\frac{y}{a}\right)^p\right)}{a^{pm}\Gamma(m)} \quad , \quad (6.15)$$

where $p > 0$. p and m are shaping parameters, and a is a scaling parameter [14]. Details of parameter estimation can be found in [90]. The generalized Gamma distribution is in fact equivalent to the generalized Nakagami model proposed by Shankar [82]. The histogram of B-scans from experiment NL002 was compared to fitted Rayleigh and generalized Gamma distributions in Fig. 6.3. Obviously, the generalized Gamma fits the histogram better than the Rayleigh distribution.

We denoted the B-scans at temperatures T_0 and T by y_0 and y_T , which follow the generalized Gamma distribution given by

$$f(y_0) = \frac{p_0 y_0^{p_0 m_0 - 1} \exp\left(-\left(\frac{y_0}{a_0}\right)^{p_0}\right)}{a_0^{p_0 m_0} \Gamma(m)} \quad ,$$

and

$$f(y_T) = \frac{p y_T^{pm-1} \exp\left(-\left(\frac{y_T}{a}\right)^p\right)}{a^{pm}\Gamma(m)} \quad .$$

The joint probability density function of (y_0, y_T) is given by [75]

$$\begin{aligned} f(y_0, y_T) &= p_0 p (1 - \rho)^m \\ &\left[\sum_{k=0}^{\infty} \frac{(m_0)_k \rho^k}{k!} \left(\frac{m_0^2}{a_0^{p_0} (1 - \rho)}\right)^{(m_0+k)} \left(\frac{m^2}{a^p (1 - \rho)}\right)^{(m+k)} \frac{y_0^{p_0(m_0+k)-1}}{\Gamma(m_0+k)} \frac{y_T^{p(m+k)-1}}{\Gamma(m+k)} \right] \\ &\exp\left\{-\frac{1}{1 - \rho} \left(\frac{m_0^2 y_0^{p_0}}{a_0^{p_0}} + \frac{m^2 y_T^p}{a^p}\right)\right\} {}_1F_1\left\{(m - m_0, m + k; \frac{\rho^2 y_T^p}{a^p (1 - \rho)}\right\} \quad , \quad (6.16) \end{aligned}$$

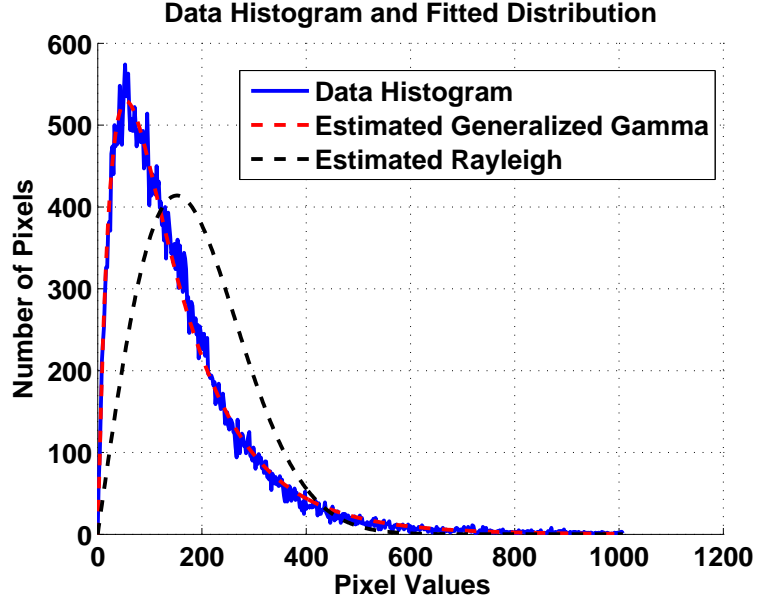


Figure 6.3: Histogram and fitted Rayleigh and generalized Gamma distribution of envelope detected images obtained in experiment NL002. The specimen is turkey breast.

where $\rho = \frac{\text{cov}(y_0^T, y_T^2)}{\sqrt{\text{var}(y_0^2)\text{var}(y_T^2)}}$ is the correlation parameter and ${}_1F_1(a; b; z) = \sum_{n=0}^{\infty} \frac{(a)_n z^n}{(b)_n n!}$ is the confluent hypergeometric function. $(u)_k = u(u+1)(u+2)\dots(u+k-1)$ is the rising factorial.

The deviation of data histograms from Gaussian/Rayleigh distributions may be due to non-uniformly distributed scatterers or the existence of isolated strong scattering, for example. In our case, we believe that non-uniformly distribution of the scatterers is a major cause of the deviation of data histogram. Fig. 6.4 shows a simulated ultrasound envelope detected image, where 3/4 of the scatterers distributes in left half and one fourth in right half of the image. Figs. 6.5 and 6.6 show the histograms and fitted distributions of the simulated RF image and envelope detected image, respectively. These results demonstrate that, when the scatterers are distributed non-uniformly, RF and envelope detected images deviate from Gaussian and Rayleigh distributions, but may be described as Laplace and generalized Gamma signals.

It is natural to ask: "Why do the histograms of RF and B-scan images deviate from Gaussian/Rayleigh when scatterers are not uniformly distributed?". Here, we provide

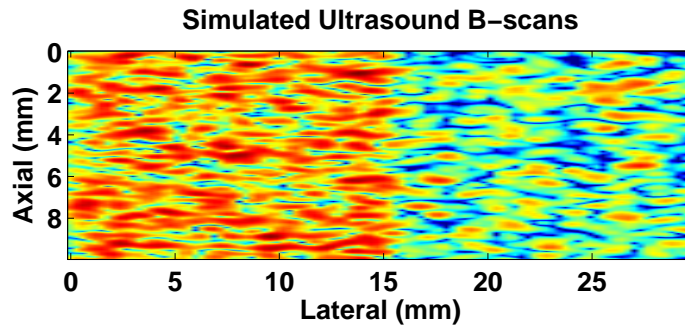


Figure 6.4: Simulated B-scans of non-uniformly distributed scatterers. Three fourths of the scatterers are located in the left half and one fourth in the right half of the image.

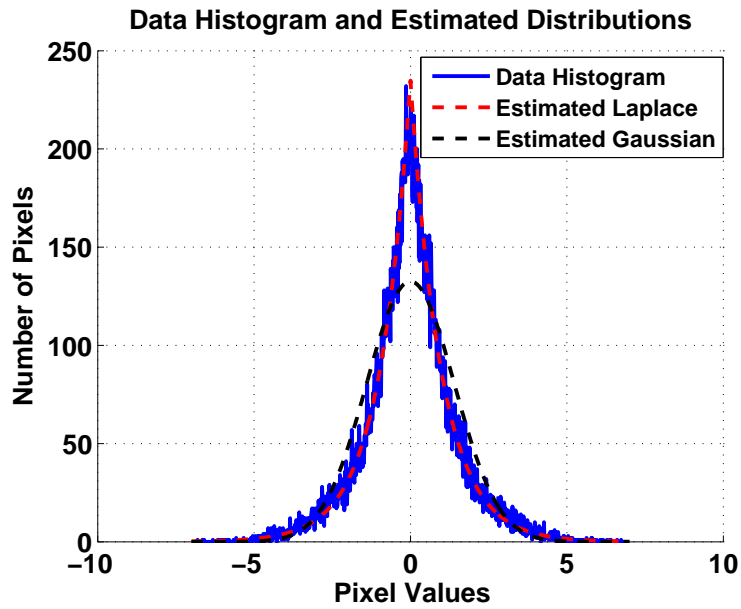


Figure 6.5: Histogram and fitted distributions of a simulated RF image.

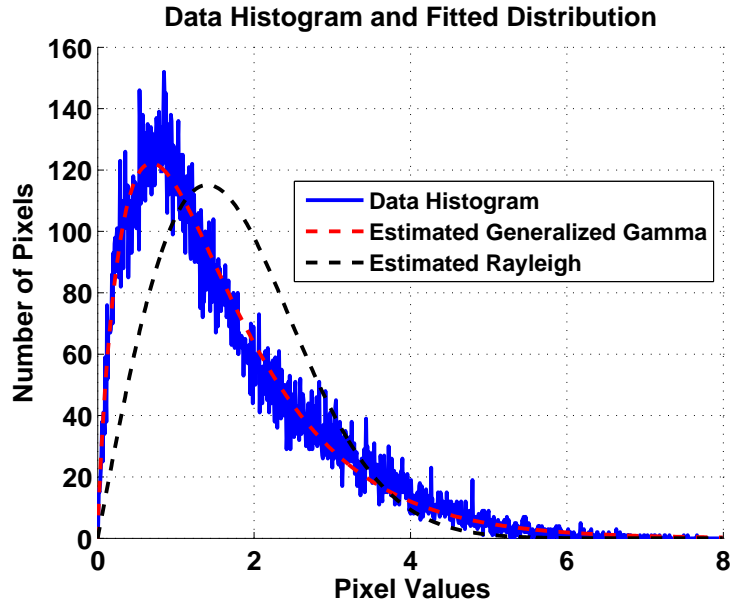


Figure 6.6: Histogram and fitted distributions of simulated envelope detected image.

a possible explanation. In fact, with the assumption of a large number of scatterers in the resolution cell of the transducer array, each pixel can still be described by a Gaussian distribution. Within the resolution cell, the scatterers are approximately uniformly distributed. Thus, each pixel in the RF image is still Gaussian with zero mean. When the scatterers are not uniformly distributed over the whole region, however, each pixel of the RF image follows a Gaussian distribution with a different variance. That is, we may still assume independent pixels, but they are not identical. When, the histogram of these non-identical pixels is fitted to a distribution, they are treated as independent identically distributed. Thus, it can not be matched by a Gaussian anymore. Correspondingly, the envelope detected image from non-uniformly distributed scatterers contains non-identically distributed Rayleigh pixels. Its histogram too no longer matches a Rayleigh distribution.

In order to illustrate this explanation, we generated 10000 Gaussian random variables with zero mean and different variance in Matlab. Data histogram and fitted distributions are shown in Fig. 6.7. The data histogram is not Gaussian, but is matched by a Laplace distribution. Similarly, we generated Rayleigh random variables with different parameters and match the data histograms to Rayleigh and generalized gamma

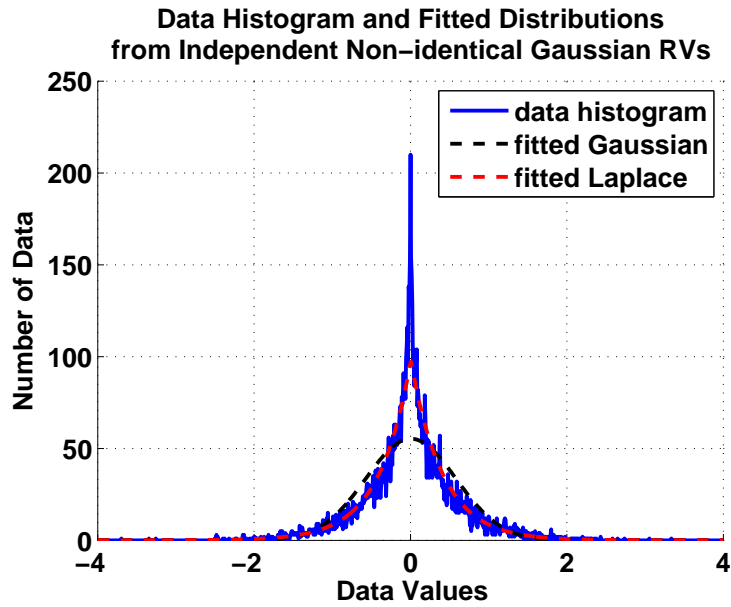


Figure 6.7: Histogram and fitted distributions of independent non-identically distributed Gaussian random variables.

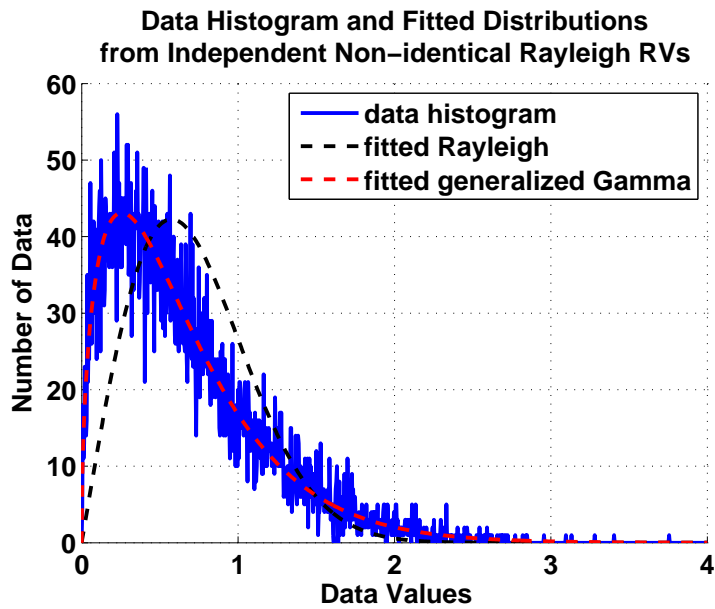


Figure 6.8: Histogram and fitted distributions of independent non-identically distributed Rayleigh random variables.

distributions as shown in Fig. 6.8. These simulations demonstrate that, when non-uniformly distributed scatterers lead to non-identically distributed image pixels, RF and B-scan histograms deviate from Gaussian and Rayleigh distributions respectively.

The above interpretation of mismatch between real image histogram and Gaussian/Rayleigh distribution may not be complete or general enough for tissue. More studies are needed for a comprehensive understanding of realistic signal statistical properties.

6.2 Formalization of CBE Computation

In this section, CBE calculation and characterization are formalized based on the discussion in the previous section. An approach to computing CBE independent of SNR is developed assuming uniformly distributed scatterers. It was used for temperature imaging in simulations and showed improvement in estimation accuracy.

6.2.1 CBE as a Ratio of Random Variables

In our initial work, CBE from backscattered signals was computed as ratios at each pixel in the envelope detected images at temperature T and T_0 [7]. CBE was characterized by averaging ratios larger than and less than 1, denoted as positive CBE (PCBE) and negative CBE (NCBE), which describe the increase and decrease in the backscattered energy respectively.

When i_{en} is represented as a random process as in the previous section, computation of the ratio can be modeled as a ratio between two random variables, y_T and y_0

$$z = \frac{y_T}{y_0} \quad . \quad (6.17)$$

Ratio, z , is also a random variable whose probability density function (PDF) is $f_Z(z)$. Computation of PCBE can be written as

$$PCBE = \frac{1}{N_+} \sum_{k \in \{k|z_k > 1\}} z_k = \frac{\frac{1}{N} \sum_{k \in \{k|z_k > 1\}} z_k}{\frac{N_+}{N}} ,$$

where N is the number of pixels in image and N_+ is the number of pixels with value larger than 1. Assuming z_k 's are independent, identically distributed random variables, the nominator approximates the integral $\int_1^\infty z f_Z(z) dz$. The denominator approximates the probability of z being larger than 1. Thus, PCBE is defined as the normalized mean of z over $z \in [1, \infty)$

$$PCBE = \frac{\int_1^\infty z f_Z(z) dz}{\int_1^\infty f_Z(z) dz} . \quad (6.18)$$

Similarly, NCBE is defined as normalized mean of z over $z \in (0, 1)$

$$NCBE = \frac{\int_0^1 z f_Z(z) dz}{\int_0^1 f_Z(z) dz} , \quad (6.19)$$

where the PDF of z is determined by the joint distribution of (y_0, y_T) [52]

$$f_Z(z) = \int_{-\infty}^{\infty} |y_0| f_{Y_0 Y_T}(y_0, y_0 z) dy_0 , \quad (6.20)$$

where y_0, y_T and $z > 0$. Since $f_Z(z)$ depends on σ_0, σ and r , PCBE and NCBE also depend on these parameters.

6.2.2 Calculation of PCBE and NCBE using Backscattered Signals from Uniformly Distributed Scatterers

In order to compute PCBE and NCBE, we need to know $f_Z(z)$. When scatterers are uniformly distributed, y_0 and y_T are Rayleigh random variables with parameters σ_0 and σ respectively. If the two signals involved in the ratio computation are

uncorrelated, that is y_0 and y_T are independent, Eq. 6.20 reduces to

$$f_Z(z) = \int_{-\infty}^{\infty} |y_0| f_{Y_0}(y_0) f_{Y_T}(y_0 z) dy_0 = \frac{2\sigma_0^2 \sigma^2 z}{(\sigma_0^2 z^2 + \sigma^2)^2} \quad (6.21)$$

Then PCBE and NCBE can be computed as

$$PCBE = \frac{\frac{\sigma^2}{\sigma_0^2 + \sigma^2} + \frac{\sigma}{\sigma_0} \left[\frac{\pi}{2} - \arctan\left(\frac{\sigma_0}{\sigma}\right) \right]}{\frac{\sigma^2}{\sigma_0^2 + \sigma^2}} \quad (6.22)$$

$$NCBE = \frac{\frac{\sigma}{\sigma_0} \arctan\left(\frac{\sigma_0}{\sigma}\right) - \frac{\sigma^2}{\sigma_0^2 + \sigma^2}}{\frac{\sigma_0^2}{\sigma_0^2 + \sigma^2}} \quad (6.23)$$

When y_0 and y_T are dependent, $f_Z(z)$ will be derived from the joint distribution given in Eq. 6.12. We computed $f_Z(z)$ by substituting Eq. 6.12 into Eq. 6.20

$$\begin{aligned} f_Z(z) &= \int_0^{\infty} |y_0| \frac{4y_0^2 z}{(1-r^2)\sigma_0^2 \sigma^2} \exp \left[-\frac{1}{1-r^2} \left(\frac{y_0^2}{\sigma_0^2} + \frac{y_0^2 z^2}{\sigma^2} \right) \right] I_0 \left(\frac{-2ry_0^2 z}{(1-r^2)\sigma_0 \sigma} \right) dy_0 \\ &= \frac{2\sigma_0^2 \sigma^2 (1-r^2)(\sigma^2 + \sigma_0^2 z^2) z}{[(\sigma^2 + \sigma_0^2 z^2)^2 - 4r^2 \sigma_0^2 \sigma^2 z^2]^{\frac{3}{2}}} \quad (6.24) \end{aligned}$$

where r is same as in Eq. 6.12. Details of the derivation can be found in Appendix B. The same result, but without details of the derivation, was shown in [13]. It is easy to show that, when y_0 and y_T are independent, i.e., $r = 0$, Eq. 6.24 becomes Eq. 6.21. Closed form solutions for PCBE and NCBE are difficult to find since the computation of integrals in Eq. 6.18 and 6.19 is not trivial. They can, however, be calculated numerically. In this study, we used function "quad" in Matlab for computing PCBE and NCBE.

Estimating Ratio PDF from Noisy Signals

Previously, when we computed CBE as ratios of B-scans, noise effects were not removed. Noise levels will impact the slope of CBE curves [103], and thus will introduce errors in calibration and temperature estimation. Fig. 6.9 shows PCBE and NCBE curves calculated by taking the ratio of simulated images at various signal to noise ratios (SNR) for a reference temperature of $37^\circ C$. It can be seen that the dynamic

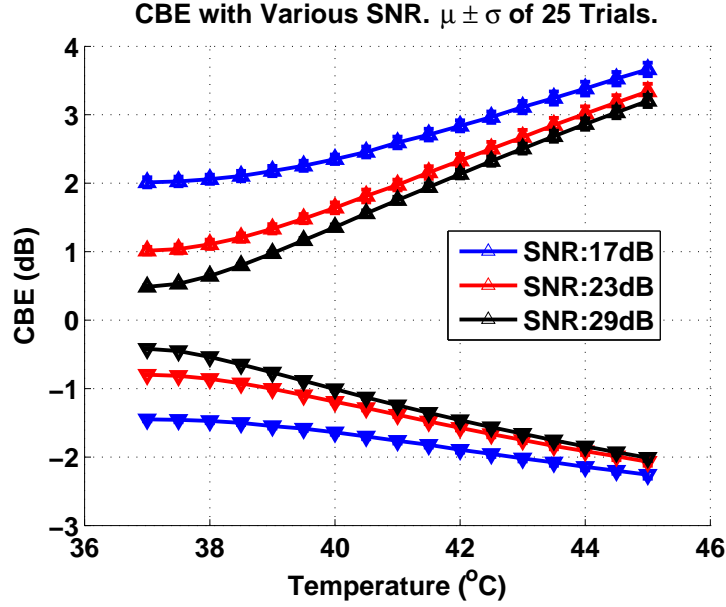


Figure 6.9: CBE from simulated images at different SNRs. They have different slopes.

ranges of PCBE and NCBE were reduced due to the jump at $37.5^{\circ}C$, which is related to the noise level.

In previous chapters, we demonstrated approaches to reducing noise effects. However, noise can not be completely removed. We wish to compute CBE independent of SNR, which may be achieved by calculating CBE from the ratio PDF. Below, we show that the parameters of the ratio PDF σ_0 , σ and r in Eq. 6.24 can be estimated from noisy signals. Therefore, CBE can be computed from estimated signal distributions such that noise effects are minimized.

Assuming additive Gaussian noise in RF signals

$$s = i_{rf} + n \quad ,$$

where s is the received RF signal, i_{rf} is the true signal, and $n \sim N(0, \sigma_n^2)$ is the noise. When i_{rf} is Gaussian with zero mean, $i_{rf} \sim N(0, \sigma^2)$, s is also Gaussian, $s \sim N(0, E(s^2))$. Then,

$$\sigma^2 = E(s^2) - \sigma_n^2 \quad ,$$

where σ_n^2 is assumed to be known. From Eq. 6.7 and 6.11, corresponding Rayleigh parameter is the same as σ . σ_0^2 and σ^2 in Eq. 6.24 can be estimated as in the above equation. From Eq. 6.12, $r = \sqrt{\frac{Cov(y_0^2 y_T^2)}{Var(y_0^2) Var(y_T^2)}}$. Let σ_{n0}^2 and σ_n^2 be the variance of noise in images at T_0 and T respectively. Let \tilde{y}_0 and \tilde{y}_T denote noise corrupted y_0 and y_T . In appendix C, it is shown that $Cov(y_0^2 y_T^2)$, $Var(y_0^2)$ and $Var(y_T^2)$ can be estimated from \tilde{y}_0 and \tilde{y}_T

$$\begin{aligned} Cov(y_0^2 y_T^2) &= Cov(\tilde{y}_0^2 \tilde{y}_T^2) \quad , \\ var(y_0^2) &= var(\tilde{y}_0^2) - 8\sigma_0^2 \sigma_{n0}^2 - 4\sigma_{n0}^4 \quad , \\ var(y_T^2) &= var(\tilde{y}_T^2) - 8\sigma^2 \sigma_n^2 - 4\sigma_n^4 \quad . \end{aligned} \quad (6.25)$$

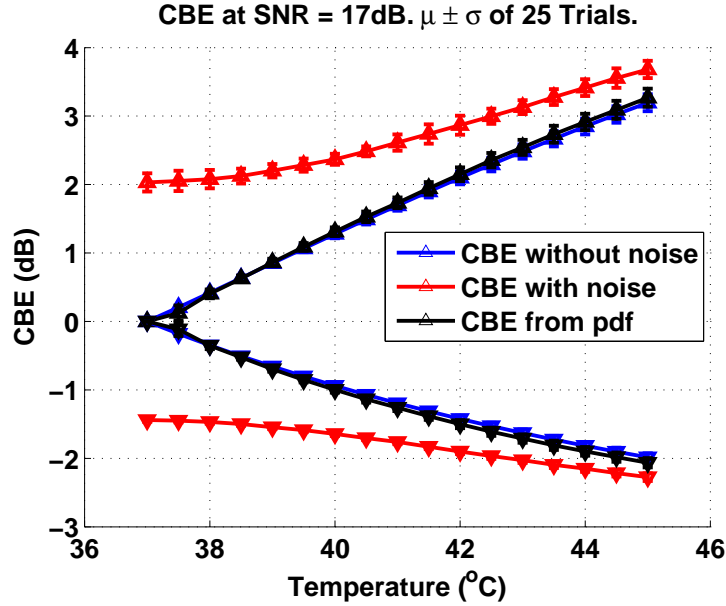


Figure 6.10: CBE from simulated images at SNR = 17dB. CBE computed using the PDF is very close to the CBE without noise. CBE computed from the signal ratio directly is much different from CBE without noise.

Thus, all the three parameters in Eq. 6.24 can be estimated from received signals with varying noise levels, given information about the noise. Figs. 6.10 and 6.11 show CBE curves computed from simulated images at 17dB and 29dB of SNR. In both figures, CBE computed from ratio PDF is consistent with CBE without noise. In other words, CBE from the ratio PDF is independent of SNR. Notice that, noise reduction studied in Chapters 3 and 5 is critical in two senses: 1) Even when CBE

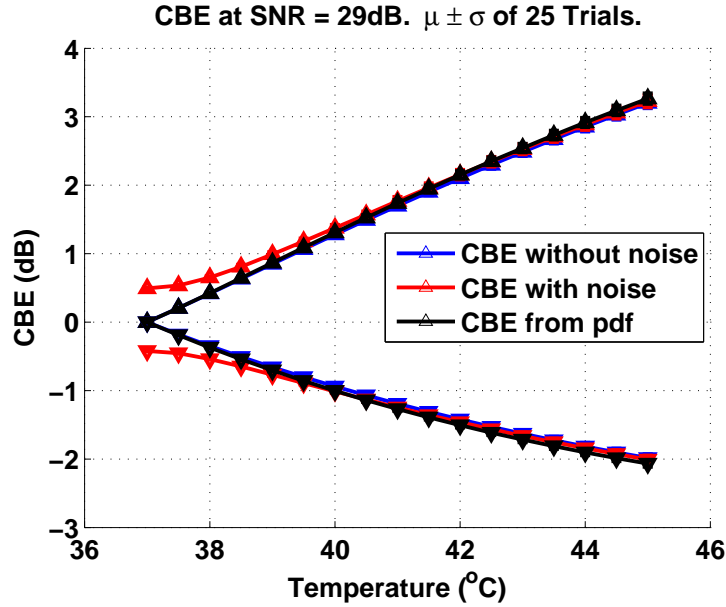


Figure 6.11: CBE from simulated images at SNR = 29dB. CBE curves computed from the distribution is very close to CBE without noise.

can be computed from the PDF, estimation of PDF parameters is more accurate at higher SNR, 2) CBE computed from the signal ratio directly should be close to CBE value without noise when SNR is high.

6.2.3 Temperature Imaging using CBE

In our initial work, in order to estimate temperature, CBE curves were calibrated from multiple trials and fitted to polynomials [103]. Here, we repeat the same approach with CBE curves computed using the ratio distribution. Ultrasonic images were simulated at SNR of $17dB$ and $29dB$, which are typical low and high SNR of experimental data. Figs. 6.12 and 6.13 show errors in temperature estimation using PCBE.

When CBE was computed from the ratio probability density function, where noise effect was taken into account, mean error in estimation is less than the error when CBE is computed directly from the ratio. When the temperature change is not large, e.g., $\delta T < 5^{\circ}C$, estimation using CBE from the ratio PDF has smaller variance

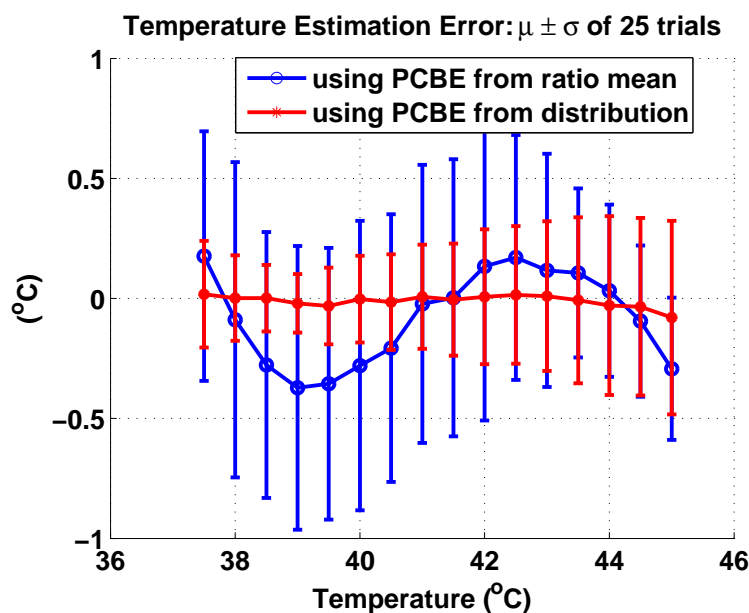


Figure 6.12: Error in temperature estimation using PCBE at SNR of 17dB.

than CBE directly from the ratio because CBE from the PDF has a larger dynamic range at lower temperatures as seen in Fig. 6.10. When the temperature change is high, CBE at successive temperatures has more overlap, independent of how CBE is calculated. Hence, estimation variance from both methods are similar and larger at high temperature than at low temperatures.

Similar conclusions can be drawn from temperature estimation using NCBE curves shown in Figs. 6.14 and 6.15. As expected, estimation error is less when SNR is higher for both approaches. The larger error at lower SNR indicates that CBE computed from the ratio PDF is not completely independent of SNR. Hence, the best way for removing noise effects is to increase SNR, which was discussed in Chapters 3 and 5.

A problem in the calibration of CBE curves and temperature estimation is that, signal to noise ratio may not be consistent over experiments. When calibration curves and curves for estimation have different SNR, large error may occur in temperature imaging. In order to achieve accurate estimates, we may have to create calibration curves at all possible SNR levels, or make all experiments run at the same SNR. One benefit resulting from being able to use the ratio PDF is that calculated CBE is independent of SNR and thus the effect of the variation in SNR is largely reduced.

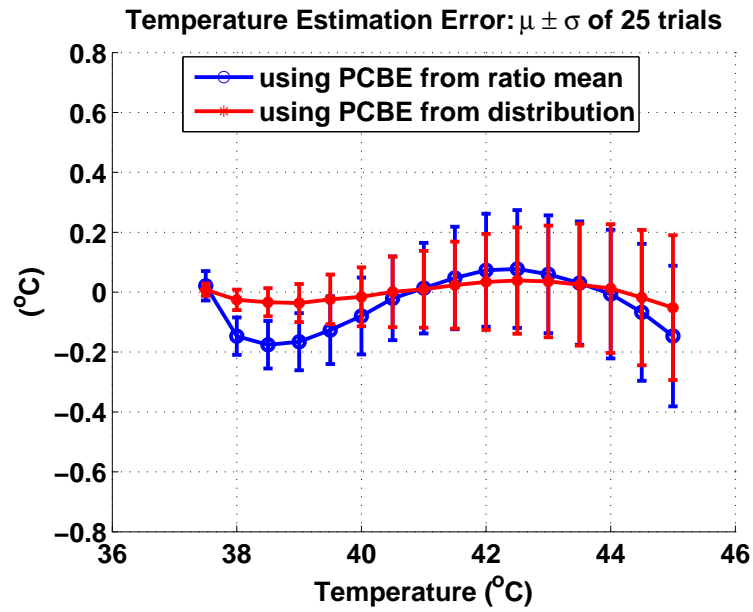


Figure 6.13: Error in temperature estimation using PCBE at SNR of 29dB.

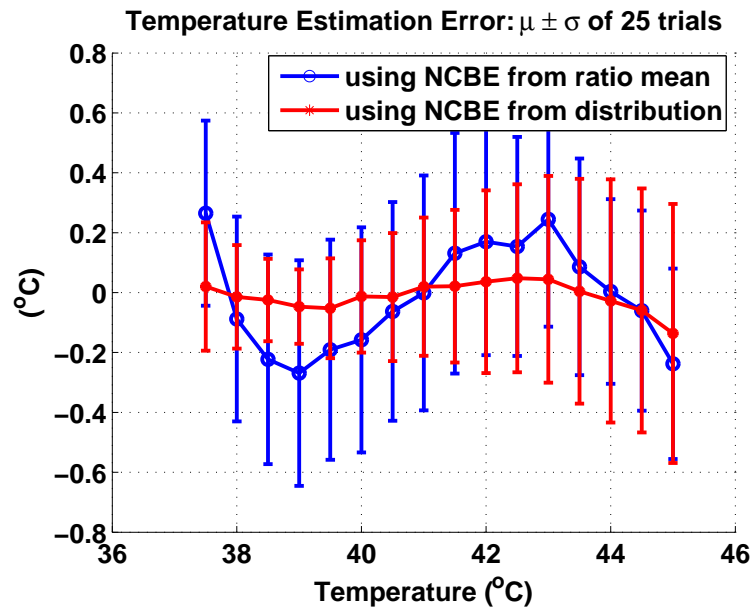


Figure 6.14: Error in temperature estimation using NCBE at SNR of 17dB.

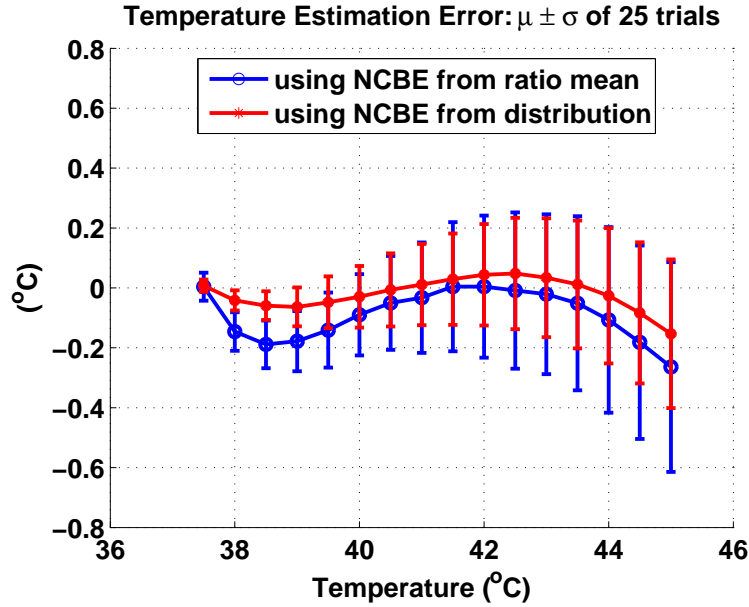


Figure 6.15: Error in temperature estimation using NCBE at SNR of 29dB.

In the following simulation, we generated calibration curves at SNR= 29dB and test data at SNR= 17dB. Estimation errors from both approaches are shown in Figs. 6.16 and 6.17. The difference in SNR between calibration and estimation data leads to large error in temperature estimation when CBE is computed from the ratio directly.

In practice, there is always uncertainty in temperature measurement, even using our calibrated thermocouples. In addition, the reference temperature and the temperature intervals may be different from experiment to experiment. If CBE is calibrated with respect to a specific value of temperature, the error may be greater than temperature estimation with respect temperature differences. The difference between CBE curves generated with different reference temperatures was simulated as shown in Fig. 6.18. In this study, CBE was calibrated with respect to the change in the temperature. Thus, the effect of different temperature references and intervals was reduced. This scheme can be seen in Fig. 6.18.

Characterization of CBE beyond PCBE and NCBE

From the computation of PCBE and NCBE, it is obvious that both contain only part of the data. Intuitively, involving more data in CBE characterization may provide

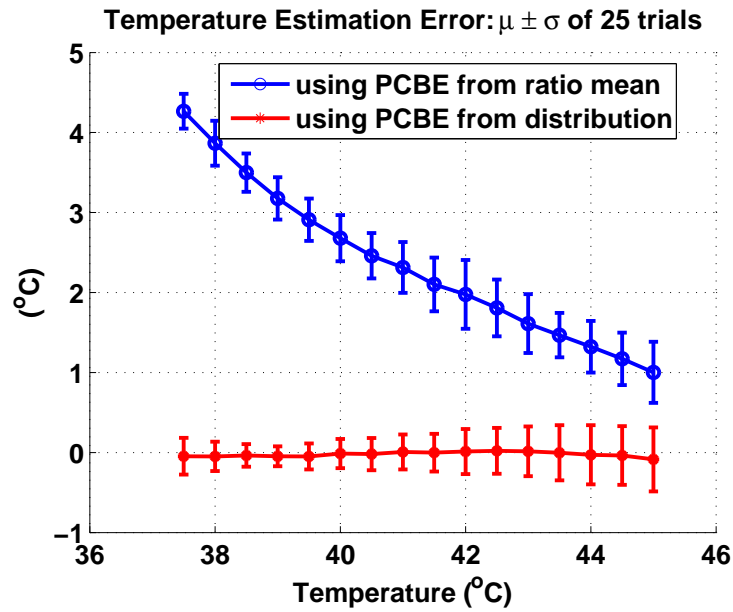


Figure 6.16: Error in temperature estimation using PCBE. Calibration curves were generated at SNR = 29dB. Test data were generated at SNR = 17dB.

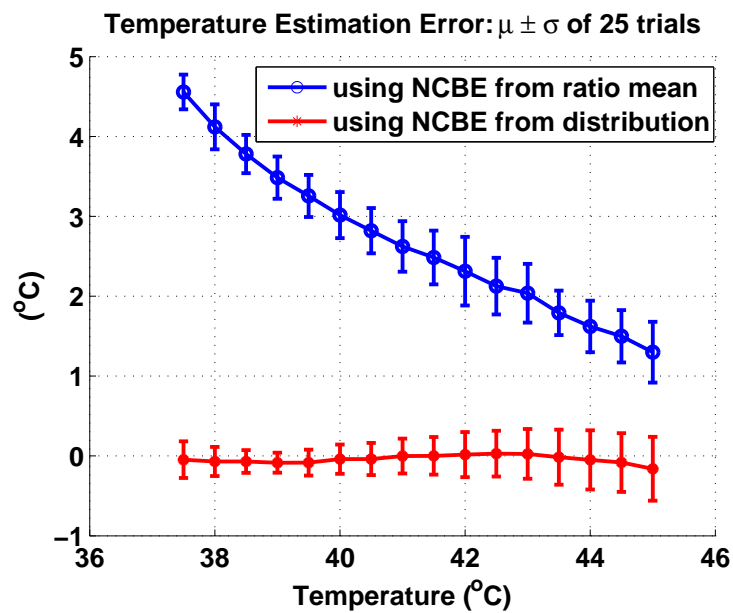


Figure 6.17: Error in temperature estimation using NCBE. Calibration curves were generated at SNR = 29dB. Test data were generated at SNR = 17dB.

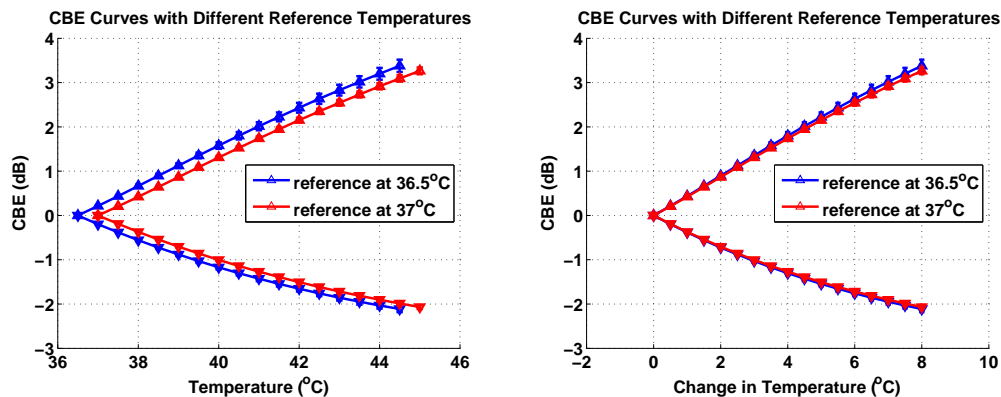


Figure 6.18: CBE curves with different reference temperatures simulated at SNR = 29dB. Left: CBE curves with respect to specific temperatures. Right: CBE curves with respect to temperature change.

more information of temperature change. For this purpose, the standard deviation (STD) of the ratio image was also examined in our initial work [7, 103]. In a more recent work based on 3D *in-vitro* experiments, it was found that estimation using the standard deviation results in less error than using PCBE and NCBE.

Better performance by using CBE STD may be because variation in CBE STD is less than the variation of PCBE and NCBE over experiments. CBE STD curves from simulated images at SNR=29dB are shown in Fig. 6.19. Compared to PCBE and NCBE curves in Fig. 6.11, the $\mu \pm \sigma$ range of CBE STD curves over 25 trials is less, especially when temperature change is small. This smaller variance of CBE STD presumably is the result of using more data (pixels) in the computation.

When signal to noise ratio is low, if CBE is computed directly from the ratio signals with noise, the advantage of the smaller variance of CBE STD may be reduced since its dynamic range over temperature is reduced by noise as shown in Fig. 6.20. More error in estimation is expected when SNR is low.

Figs. 6.21 and 6.22 show error in temperature estimation from simulated images using CBE STD at SNR = 17 and 29dB. As expected, when SNR=29dB, the estimation error is less than the error of using PCBE and NCBE in Figs. 6.13 and 6.15. However, comparing Fig. 6.21 to Figs. 6.12 and 6.14, it can be seen that the estimation

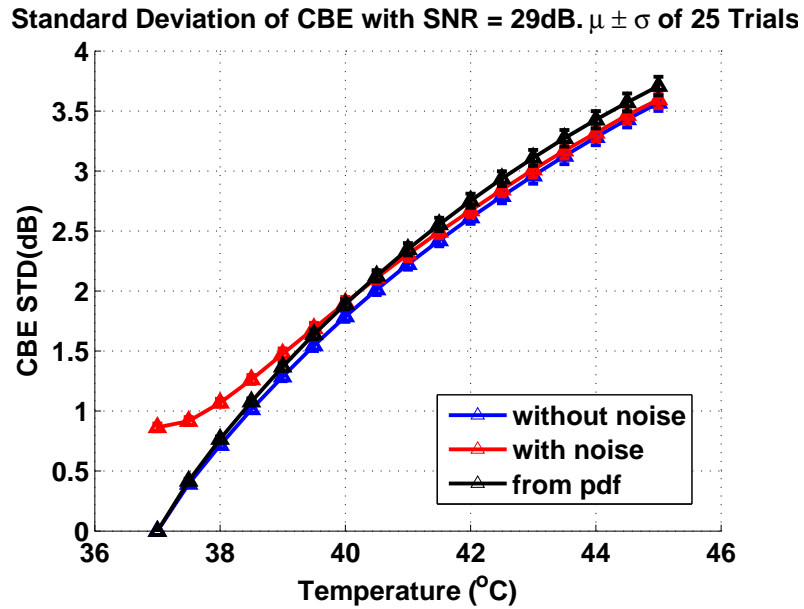


Figure 6.19: CBE STD computed simulated images at SNR = 29dB. Curves of STD with noise is close to the curves without noise at this SNR level.

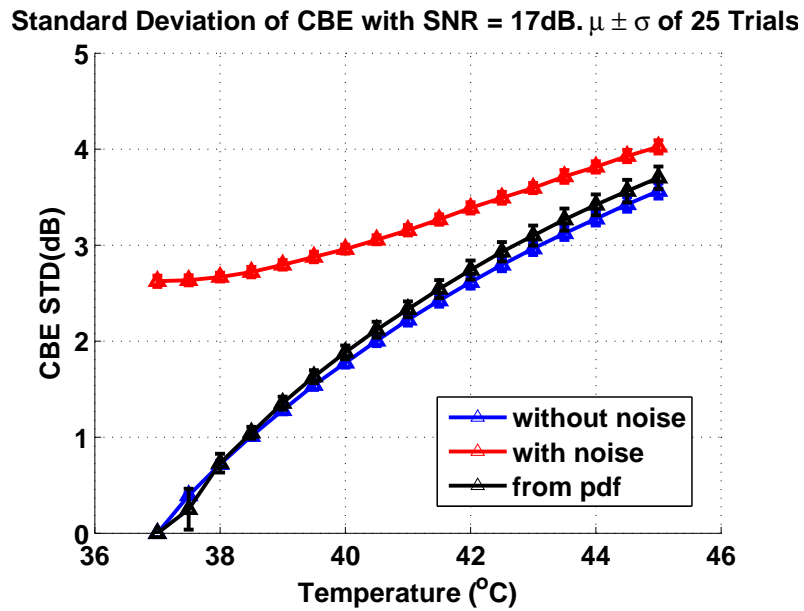


Figure 6.20: CBE STD computed from simulated images at SNR = 17dB. The curve of STD with noise has less dynamic range over temperature than the one without noise.

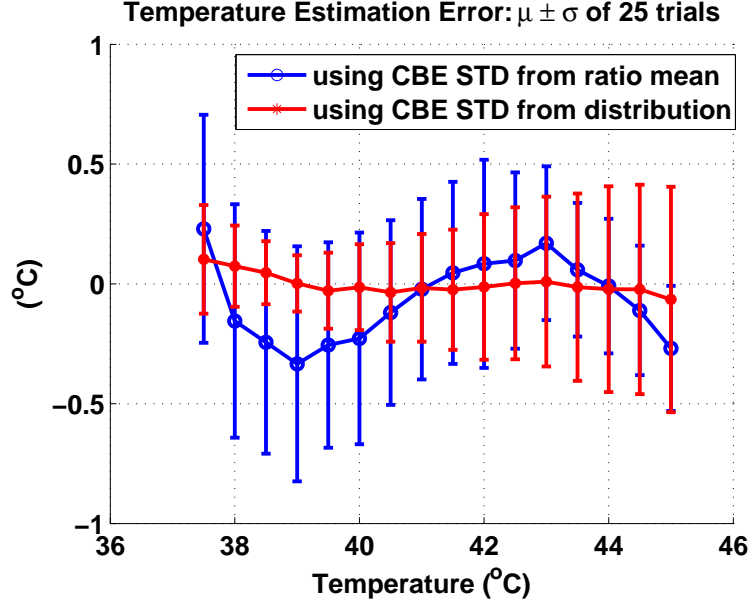


Figure 6.21: Error in temperature estimation using CBE STD at SNR = 17dB.

performance of using CBE STD is not better than that of using PCBE and NCBE when SNR is low.

We would point out that, the standard deviation here is not the standard deviation of the ratio, z . In stead of computing $20 * \log_{10}(STD(z))$, $20 \log_{10}(z)$ was calculated first and then the STD of the new variable was computed. In other words, we are looking at the STD of

$$u = 20 \log_{10}(z) \quad ,$$

whose distribution can be derive analytically when the scatterers are uniformly distributed over the region

$$f_U(u) = \frac{(\ln(10))\sigma_0^2\sigma^2(1-r^2)(\sigma^2 + \sigma_0^2 10^{u/10})(10^{u/10})}{10 [(\sigma^2 + \sigma_0^2(10^{u/10}))^2 - 4r^2\sigma_0^2\sigma^2(10^{u/10})]^{\frac{3}{2}}} \quad . \quad (6.26)$$

As for the parameters for ration PDF, σ_0^2 , σ^2 and r^2 can be estimated independent of SNR assuming uniformly distributed scatterers. Thus, the CBE STD discussed can also be computed independent of SNR.

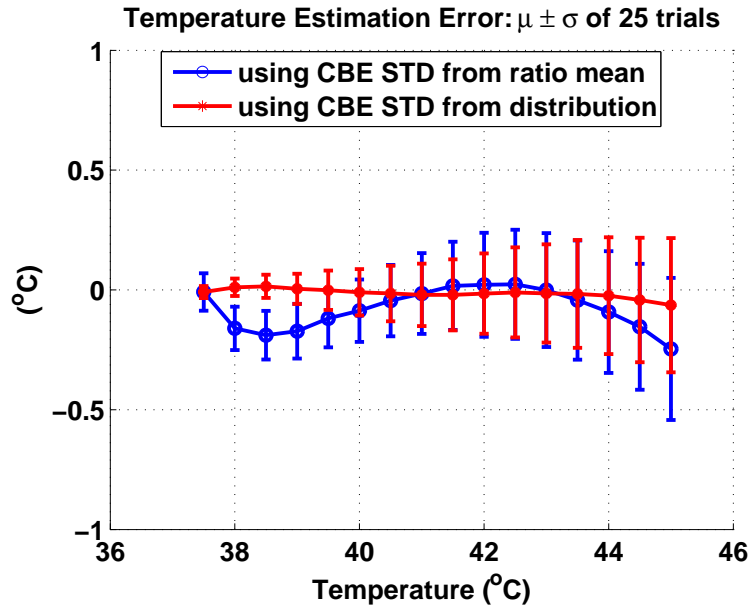


Figure 6.22: Error in temperature estimation using CBE STD at SNR = 29dB.

6.3 Summary and Conclusions

In this chapter, we modeled the problem of temperature imaging via a probabilistic framework and formalized our computational approach of CBE. As an example, we assumed uniformly distributed scatterers and showed that CBE can be computed independent of noise to improve temperature accuracy. More studies are needed to extend the results of this chapter to realistic experimental data. We would also like to explore approaches other than the energy ratio used in our initial work and in this chapter. These studies are presented in the next chapter.

Chapter 7

Examples of Temperature Imaging Beyond the Energy Ratio

In the previous chapter, temperature imaging was modeled as a problem of estimating tissue temperature from random processes or collection of random variables resulting from the thermal change in signals. A mathematical representation was developed for the energy ratio, which was shown as a potential parameter of temperature imaging for hyperthermia. As shown in the last chapter, this formalization for CBE based approach improved temperature accuracy under certain conditions. We, however, do not know if the energy ratio is the optimal choice for a thermometry. Here we explore other possible parameters and approaches to temperature imaging.

As mentioned before, distribution of the energy ratio is determined by the joint distribution of the two random variables involved in the ratio computation. Thus, the joint distribution should also contain temperature information. In this chapter, mutual information is explored as an example of parameters extracted from the joint distribution for temperature imaging. It shows the possibility of estimating temperature based on the change in the joint distribution.

It was seen that the ratio computation may lead to outliers that may affect CBE computation. In this chapter, instead of ratio, we also look at the difference between images. A maximum likelihood estimator is derived based on image difference by linearizing the random phasor sum representation.

7.1 Temperature Imaging based on the Joint Distribution of Signals at Reference and Current Temperatures

Previously, temperature imaging was modeled as estimating temperature from the random processes resulting from thermal effects of tissue on ultrasonic signals. The random processes are collections of random variables indexed by temperature. In this study, we pursue approaches to estimating temperature given measured random variables, (x_0, x_T) and (y_0, y_T) which represent RF and B-scan signals at reference and current temperatures, respectively. Information of thermal change of the tissue is contained in the joint distributions $f_X(x_0, x_T)$ or $f_Y(y_0, y_T)$. Therefore, temperature may be estimated from $f_X(x_0, x_T)$ or $f_Y(y_0, y_T)$.

Previously, the distribution of ratio z between y_T and y_0 , $f_Z(z)$, is determined by the joint distribution of (y_0, y_T) , $f(y_0, y_T)$. Variation of $f_Z(z)$ with temperature corresponds to the change in $f(y_0, y_T)$. To illustrate this relation, joint histograms of simulated B-scans at various temperatures and the corresponding ratio histograms are plotted in Fig. 7.1.

When temperature increases, the joint histogram is less concentrated around the diagonal because signals are more uncorrelated. Accordingly, more ratio values fall in the regions larger than and less than 1 in the ratio histogram, which correspond to the left-top and right-top of the joint distribution, respectively. In other words, temperature information contained in the joint distribution is transferred to the ratio. In this section, we estimate temperature directly from the joint distribution.

7.1.1 Temperature Imaging using Mutual Information (MI)

When computing CBE, we took the ratio between signals, which may be regarded as a similarity measure of the signals. When temperature increases, more ratio values fall in regions larger than or smaller than 1, indicating that the signals are less alike. Alternatively, a straightforward similarity measure based on joint distribution

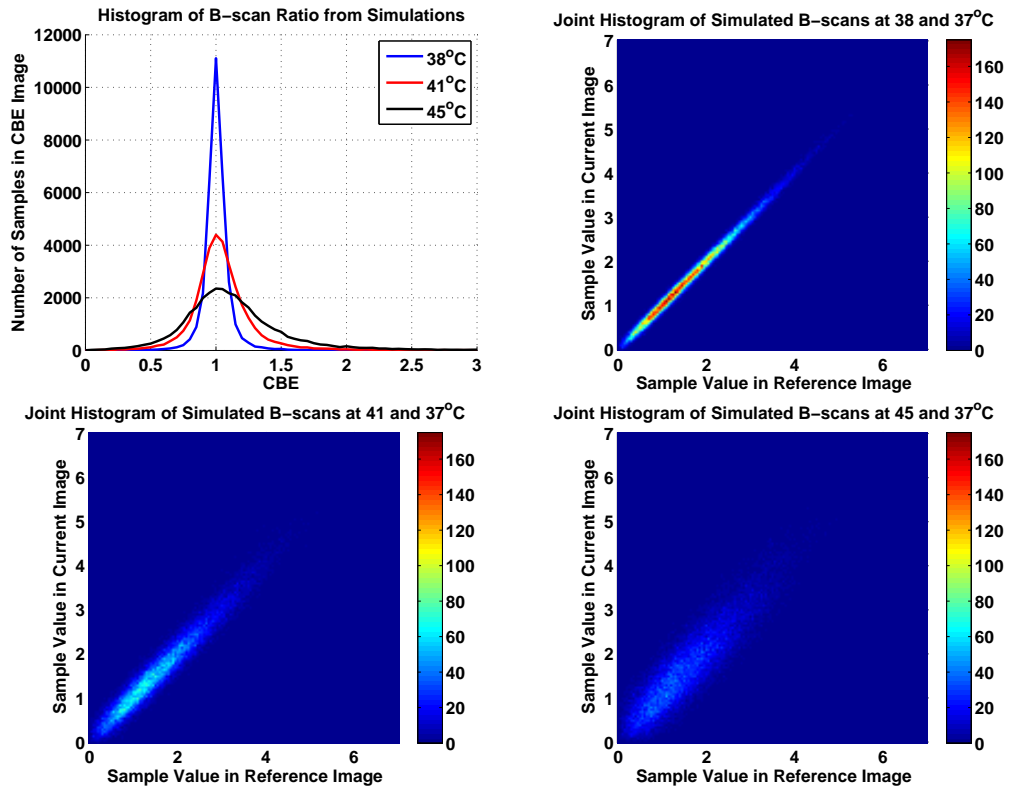


Figure 7.1: Ratio PDF and joint distribution of Simulated B-scans. Upper-left: Ratio PDF at various temperatures. Upper-right and Bottom: Joint histograms of current and reference simulated B-scan at various temperatures.

is mutual information (MI). In this section, we study the potential of using mutual information for temperature imaging.

Mutual information of two random variables, a_1 and a_2 , is defined as [24]

$$I(a_1; a_2) = \int f(a_1, a_2) \log \frac{f(a_1, a_2)}{f(a_1)f(a_2)} da_1 da_2 \quad ,$$

where $f(a_1)$ and $f(a_2)$ are probability density functions of a_1 and a_2 , $f(a_1, a_2)$ is the joint density function of a_1 and a_2 . Alternatively, mutual information can be computed by

$$I(a_1; a_2) = h(a_1) + h(a_2) - h(a_1, a_2) \quad ,$$

where $h(a_1)$ and $h(a_2)$ are differential entropies of a_1 and a_2 , $h(a_1, a_2)$ is the joint entropy of a_1 and a_2 .

We first consider the situation of uniformly distributed scatterers. Computation of mutual information involves the logarithm of the density functions, which raises difficulties in computing mutual information from the joint distribution of the envelope detected signals shown in Eq. 6.16. Consequently, we considered mutual information of RF signals instead of B-scans. RF signals are Gaussian with joint density shown in Eq. 6.8, and mutual information from RF signals can be computed by [24]

$$I(x_0; x_T) = -\frac{1}{2} \log(1 - \rho^2) \quad , \tag{7.1}$$

where x_0 and x_T are random variables representing RF signals at reference and current temperatures, ρ is the correlation coefficient defined in Eq. 6.8. Clearly, calculation of MI for RF signals depends simply on the correlation coefficient, ρ , which can be estimated accurately from noisy signal. Hence, given noise information, mutual information may be estimated independent of SNR.

Fig. 7.2 shows the mutual information estimated from ultrasonic RF signals simulated at various SNRs. Because noise has been taken into account, mutual information curves with temperature at various signal to noise ratios are consistent to each other. These consistencies in MI at different SNRs make it feasible to estimate temperature without calibrating MI for all SNRs or making all experiments at same SNR.

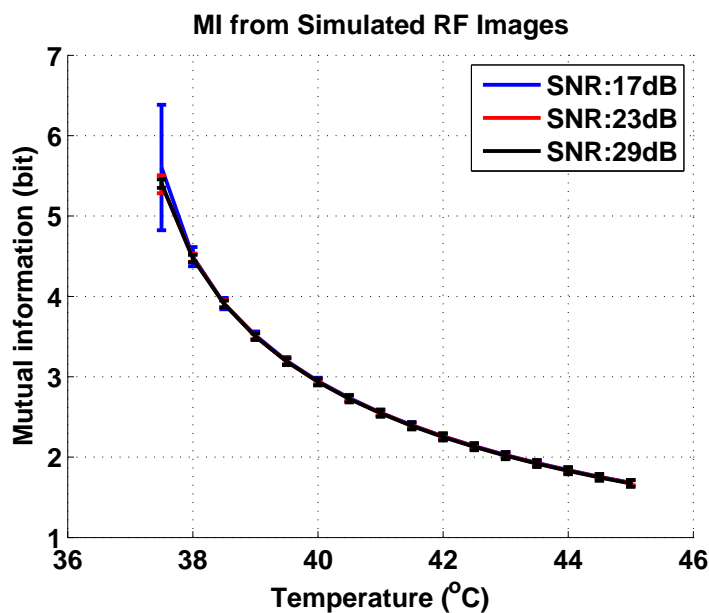


Figure 7.2: MI with temperature computed from simulated RF images at various SNR levels.

Notice that MI curve at SNR=17dB has large variance at $37.5^{\circ}C$. This large variance occurred because images at 37 and $37.5^{\circ}C$ are highly correlated, i.e., $\rho \rightarrow 1$, so that $I(x_0; x_T) \rightarrow \infty$. When SNR is low, there could be small errors in the estimation of ρ , which leads to large error in MI. Consequently, $I(x_0; x_T)$ varies dramatically due to error in estimating ρ at low SNR. For accurate temperature estimation, we are again required to increase SNR in the images as described in chapter 3.

Fig. 7.3 shows the error in temperature estimation using mutual information in simulations. MI curves from simulated images at SNR=29dB were calibrated and fitted to an 3rd order polynomial. MI for temperature estimation was then computed from simulated RF images at SNR=17, 23 and 29dB. Estimation error is less than $0.35^{\circ}C$ for all SNRs, except for that at $37.5^{\circ}C$ at SNR=17dB, which resulted from the large variance of MI at this point. The above results show that, assuming uniformly distributed scatterers, MI is a potential parameter for temperature imaging. Application of MI to experimental data is discussed in the next chapter.

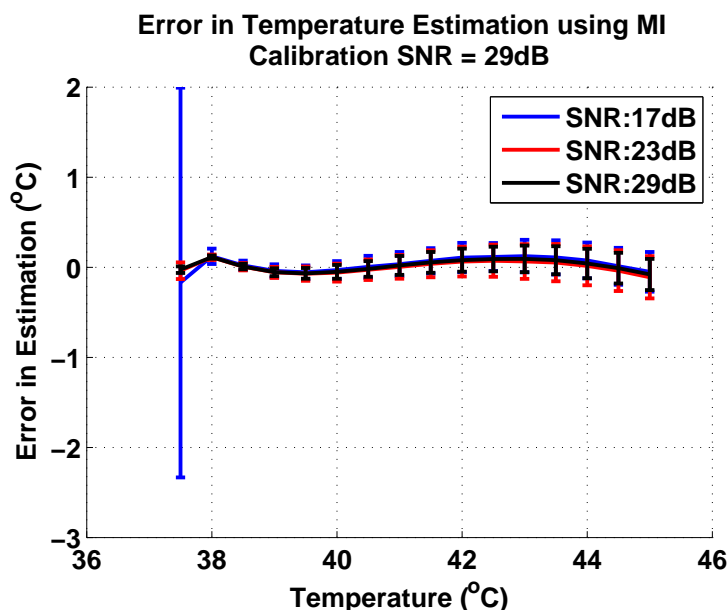


Figure 7.3: Error in temperature estimation using MI. Calibration was at SNR = 29dB. Test data for temperature estimation was simulated at SNR = 17, 23 and 29dB, respectively.

7.1.2 Temperature Imaging using Cross Correlation

From Eq. 7.1, it is seen that mutual information for RF signals depends only on the correlation coefficient ρ . Therefore, instead of computing mutual information, similarity of signals can also be measured by their cross correlation coefficient. The advantage of using cross correlation is that, when SNR is low, estimation of mutual information of highly correlated signals has large variance as seen in Fig. 7.2, but the correlation coefficient converges to 1. Hence, it does not have large variance at $37.5^{\circ}C$ as does the mutual information.

For Gaussian RF signal, ρ can be estimated accurately from different SNR levels given noise information. ρ curves estimated from simulated RF images at various SNRs are shown in Fig. 7.4. Errors in temperature estimation using ρ are shown in Fig. 7.5. Again, to illustrate the benefit gained by accurately estimating ρ from noisy signals, calibration of ρ was at SNR=29dB and temperature estimation was at SNR=17, 23 and 29dB.

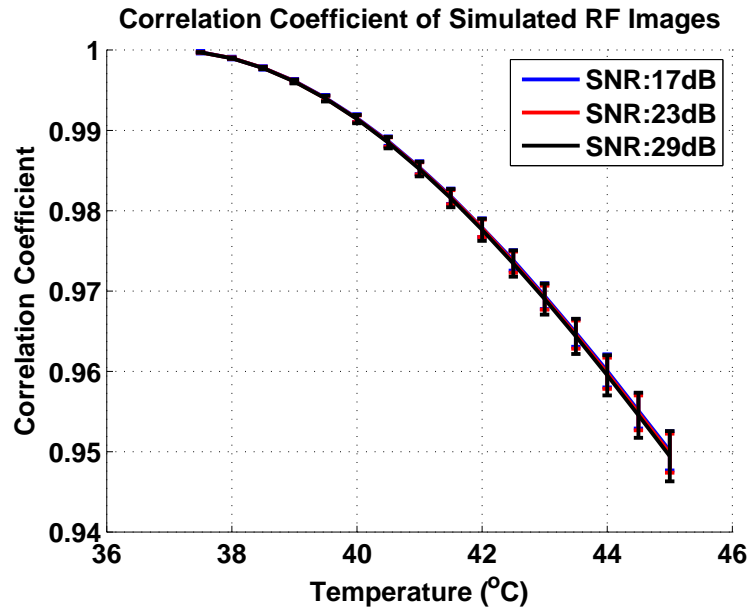


Figure 7.4: Correlation coefficients of simulated RF images at various SNRs.

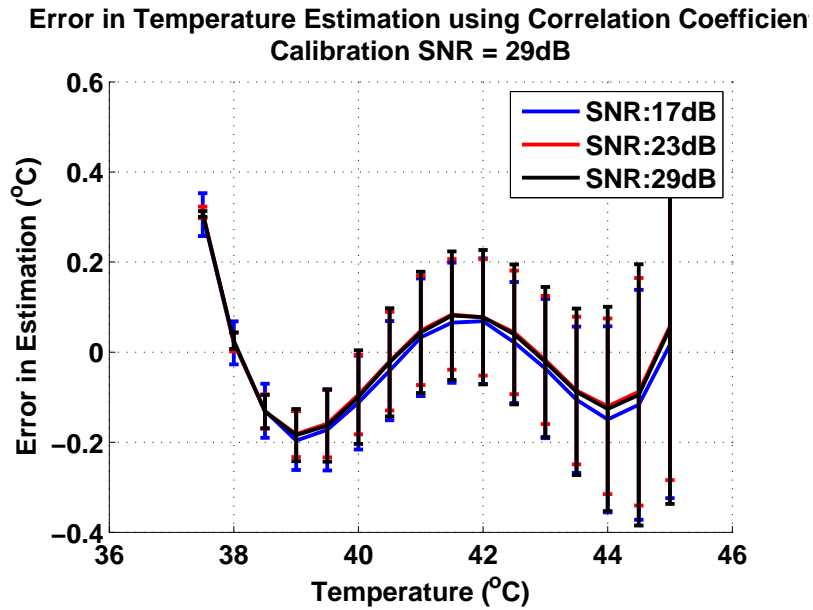


Figure 7.5: Error in temperature estimation using correlation coefficient. Calibration SNR=29dB.

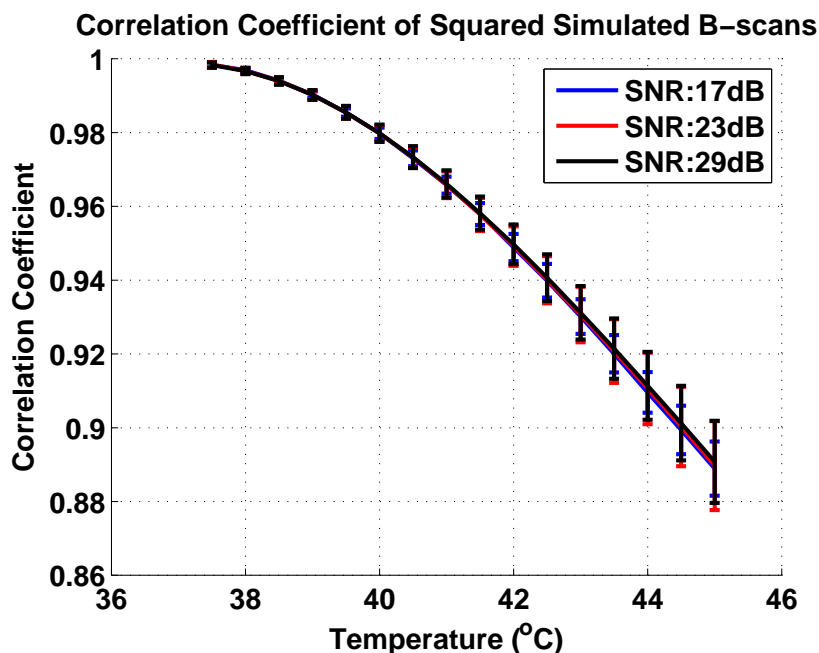


Figure 7.6: Correlation coefficient of squared simulated B-scans at various SNRs.

Alternatively, the correlation coefficient may be computed between envelope detected images. It is, however, not easy to estimate the B-scan correlation from noisy signals. Fortunately, we were able to compute correlation coefficient for the square of envelope-detected images, which is considered equivalent to the correlation between B-scans. This correlation coefficient is in fact r^2 in Eq. B.3 and can be estimated as in Eq. 6.25, where noise effect is taken into account. Fig. 7.6 shows r^2 from simulated B-scans of various SNRs. The r^2 curves of the B-scans in Fig. 7.6 are similar to the ρ curves of RF images in Fig. 7.4. Therefore, r^2 may also be used for temperature estimation.

7.2 A Maximum Likelihood Estimator for Tissue Temperature

In the previous study, CBE computation was formalized as a ratio between random variables and characterized as PCBE and NCBE which were formally defined as statistics of the ratio. During this procedure, temperature, however, did not show up

explicitly in PCBE and NCBE computation. That is, PCBE and NCBE were implicit functions of temperature. We fitted PCBE and NCBE curves to polynomials to find their dependence on temperature. The same problem existed in estimation based on the joint distributions between random variables.

The lack of an explicit relation between computed statistics and temperature resulted from the joint distribution which is generic for two random variables. For example, the joint distribution of two Rayleigh variables in Eq. B.3 is valid for any two dependent Rayleigh random variables including that used in our study. We know that temperature information must be contained in the joint distribution. Hence, it should be contained in the parameters of the generic joint distribution in an implicit way.

In this section, based on the CBE model for individual scatterers, we look at the effect of thermal change in backscattering on the signal model. We explore an approximate dependence of data distribution on temperature change, from which, a maximum likelihood estimator can be derived. In order to overcome the problem of "outliers" in ratio computation, we investigate the change in signals in the difference between images.

7.2.1 Envelope of the Image Difference

The ultrasonic signal at a given location is a coherent addition of the scattering within the resolution cell, which can be described by a sum of random phasors[110, 100]. Recall the random phasor sum of temperature dependent backscattered signals in Eq. 6.3 is

$$i_T(\mathbf{r}) = \sum_{k=1}^N A_k(T) e^{j\phi_k} \quad .$$

In [92], Straube and Arthur proposed a model for the change in the backscattered energy from single scatterers relative to the reference temperature. Consequently, the discrete tissue model is also temperature dependent as shown in Eq. 6.2[103], which may be further modified in form

$$q(\mathbf{r}, T) = \sum_{k=1}^N q_k(T) \delta(\mathbf{r} - \mathbf{r}_0) = \sum_{k=1}^N \beta_k(T) q_k(T_0) \delta(\mathbf{r} - \mathbf{r}_0) \quad ,$$

where $\beta_k(T)$ represents the change in reflectivity for individual scatterers at T and $\beta_k(T_0) = 1$. Since $A_k(T)$ is proportional to $q_k(T)$, Eq. 6.3 becomes

$$i_T(\mathbf{r}) = \sum_{k=1}^N \beta_k(T) A_k(T_0) e^{j\phi_k} \quad , \quad (7.2)$$

where β_k is the same as in the preceding equation. In order to measure the change in signals, we looked at the magnitude of difference between the complex envelopes at T and T_0

$$\begin{aligned} z &= |i_{\Delta T}| = |i_T - i_{T_0}| \\ &= \left| \sum_{k=1}^N (\beta_k(T) - \beta_k(T_0)) A_k(T_0) e^{j\phi_k} \right| \quad , \end{aligned} \quad (7.3)$$

where $\Delta T = T - T_0$ is the change in temperature. Eq. 7.3 shows that the difference of the complex envelopes can still be represented by a random phasor sum and z is the magnitude of the sum

$$z = |R_z + jI_z| \quad , \quad (7.4)$$

where R_z and I_z are real and imaginary components of $i_{\Delta T}$, $R_z \perp I_z$. When scatterers are uniformly distributed over the region, $R_z, I_z \sim N(0, \sigma^2)$. Then, z is simply a Rayleigh random variable

$$f_Z(z) = \frac{z}{\sigma^2} e^{-\frac{z^2}{2\sigma^2}} \quad , \quad (7.5)$$

For experimental data which is not Rayleigh, we may model z by a generalized Gamma distribution:

$$f_Z(z) = \frac{p z^{pm-1} \exp\left(-\left(\frac{z}{a}\right)^p\right)}{a^{pm} \Gamma(m)} \quad , \quad (7.6)$$

It is, however, not clear how the parameters of the generalized Gamma relate to parameters of distributions of R_z and I_z .

7.2.2 Maximum Likelihood Estimator

We first derive the maximum likelihood estimator (MLE) assuming the scatterers are uniformly distributed, i.e., z in Eq. 7.3 is Rayleigh. Furthermore, the pixels in the images were assumed to be i.i.d. Therefore, the likelihood function of the difference

magnitude image is

$$\begin{aligned}
L(T) = p(\bar{z}|T) &= \prod_{l=1}^M \frac{z_l}{\sigma^2} e^{-\frac{z_l^2}{2\sigma^2}} \\
&= \frac{\prod_{l=1}^M z_l}{\sigma^{2M}} \exp\left(-\frac{1}{2\sigma^2} \sum_{l=1}^M z_l^2\right) ,
\end{aligned} \tag{7.7}$$

where $\bar{z} = \{z_1, z_2, \dots, z_M\}$ is the set of random variables representing the pixels, M is the number of pixels in the image. The likelihood function is a function of temperature, although temperature does not appear in Eq. 7.7 explicitly but imbedded in parameter σ^2 . In order to introduce temperature to the likelihood function, we look at the random phasor sum of $i_{\Delta T}$ in Eq. 7.3, where $\beta_k(T)$ is the term associated with temperature. We assumed that $\beta_k(T)$ can be approximated linearly by the first two terms of its Taylor expansion at T_0

$$\beta_k(T) \cong \beta_k(T_0) + \Delta T \beta'_k(T_0) \quad , \tag{7.8}$$

where $\beta'_k(T_0)$ is the first order derivative of $\beta_k(T)$ evaluated at T_0 . We regarded Eq. 7.8 as a linear approximation of $\beta_k(T)$ because it contains only the first two terms in β_k 's Taylor expansion and it is a linear function of the temperature change. Substituting Eq. 7.8 into Eq. 7.3, z can be approximated as

$$z = |R_z + jI_z| \cong \left| \Delta T \sum_{k=1}^N \beta'_k(T_0) A_k(T_0) e^{j\phi_k} \right| = \Delta T \left| \sum_{k=1}^N \beta'_k(T_0) A_k(T_0) e^{j\phi_k} \right| \quad , \tag{7.9}$$

where z is a Rayleigh random variable with parameter σ^2 as shown in Eq. 7.5.

$\left| \sum_{k=1}^N \beta'_k(T_0) A_k(T_0) e^{j\phi_k} \right|$ is in fact the approximation of $z(\Delta T = 1)$, which is denoted as

$$z^1 \equiv z(\Delta T = 1) \cong \left| \sum_{k=1}^N \beta'_k(T_0) A_k(T_0) e^{j\phi_k} \right| = |R_1 + I_1| \quad , \tag{7.10}$$

where $R_1, I_1 \sim N(0, \sigma_1^2)$ are independent Gaussian random variables. z^1 is also a Rayleigh random variable with parameter $\sigma_{z^1}^2 \cong \sigma_1^2$. From Eq. 7.9, $R_z \cong \Delta T R_1$, $I_z \cong \Delta T I_1$ and

$$\sigma^2 \cong \Delta T^2 \sigma_1^2 \quad .$$

Eq. 7.5 is approximated as

$$f_Z(z) = \frac{z}{\sigma^2} e^{-\frac{z^2}{2\sigma^2}} \cong \frac{z}{\Delta T^2 \sigma_1^2} e^{-\frac{z^2}{2\Delta T^2 \sigma_1^2}} \quad . \quad (7.11)$$

Consequently, the likelihood function becomes

$$L(T) = p(\bar{z}|T) \cong \frac{\prod_{l=1}^M z_l}{\Delta T^{2M} \sigma_1^{2M}} \exp\left(-\frac{1}{\Delta T^2 \sigma_1^2} \sum_{l=1}^M z_l^2\right) \quad . \quad (7.12)$$

Corresponding log likelihood function is

$$\ln L \cong \sum \ln(z_l) - 2M \ln \Delta T - M \ln \sigma_1^2 - \frac{1}{\Delta T^2 \sigma_1^2} \sum_{l=1}^M z_l^2 \quad . \quad (7.13)$$

Differentiating $\ln L$ with respect to ΔT and setting the result to zero lead to

$$\frac{\partial \ln p(\bar{z}|\Delta T)}{\partial \Delta T} = 0 \quad .$$

The maximum likelihood estimator for temperature change is then

$$\widehat{\Delta T} = \sqrt{\frac{\frac{1}{2M} \sum_{l=1}^M z_l^2}{\sigma_1^2}} \quad , \quad (7.14)$$

where $\frac{1}{2M} \sum_{l=1}^M z_l^2$ is in fact the maximum likelihood estimator for σ^2 . In order to apply Eq. 7.14, σ_1^2 should be known. Here, we assume the image at $\Delta T = 1$, i.e., z^1 is known, then σ_1^2 can be estimated as

$$\widehat{\sigma}_1^2 \cong \widehat{\sigma}_{z^1}^2 = \frac{1}{2M} \sum_{l=1}^M (z_l^1)^2 \quad .$$

Notice that the MLE is for the change in temperature and not for a specific temperature. This makes sense because all images were compared to a reference.

Noise Effects

As shown before, the noise in RF signals can be assumed to be additive white Gaussian, i.e., $s = i_{rf} + n$, where s is observed RF signals, $n \sim N(0, \sigma_n^2)$ is the noise. We assume σ_n^2 is known or can be estimated from signals. Accordingly, magnitude of difference image, z in Eq. 7.9 becomes

$$\check{z} = |(R_z + n_R) + j(I_z + n_I)| \quad , \quad (7.15)$$

where \check{z} is the observed z with noise, $n_R \perp n_I$, $n_R, n_I \perp R_z, I_z$, $n_R, n_I \sim N(0, \sigma_{nz}^2)$, and $\sigma_{\check{z}}^2 = \sigma^2 + \sigma_{nz}^2$. Since n_R and n_I resulted from the difference of two images, $\sigma_{nz}^2 = 2\sigma_n^2$. Therefore, $\sigma^2 = \sigma_{\check{z}}^2 - 2\sigma_n^2$. When these parameters are estimated from data

$$\hat{\sigma}^2 = \hat{\sigma}_{\check{z}}^2 - 2\hat{\sigma}_n^2 = \frac{1}{2M} \sum_{l=1}^M \check{z}_l^2 - 2\hat{\sigma}_n^2 \quad .$$

Similarly, $\hat{\sigma}_1^2 = \frac{1}{2M} \sum_{l=1}^M (\check{z}_l^1)^2 - 2\hat{\sigma}_n^2$. The maximum likelihood estimator in Eq. 7.14 becomes

$$\widehat{\Delta T} = \sqrt{\frac{\frac{1}{2M} \sum_{l=1}^M \check{z}_l^2 - 2\hat{\sigma}_n^2}{\frac{1}{2M} \sum_{l=1}^M (\check{z}_l^1)^2 - 2\hat{\sigma}_n^2}} \quad . \quad (7.16)$$

7.2.3 Factors Affecting the Performance of MLE

A good estimator is an unbiased one with small variance. We investigate the mean and variance of the estimator in Eq. 7.16 qualitatively for factors affecting estimator performance.

Mean of the estimator

For simplicity, we studied $\widehat{\Delta T}^2$ in stead of $\widehat{\Delta T}$ in Eq. 7.16

$$\widehat{\Delta T}^2 = \frac{\frac{1}{2M} \sum_{l=1}^M \check{z}_l^2 - 2\hat{\sigma}_n^2}{\frac{1}{2M} \sum_{l=1}^M \check{z}_{1l}^2 - 2\hat{\sigma}_n^2} \quad . \quad (7.17)$$

In principle, the denominator and numerator in the above equation are correlated random variables and calculation of $E[\widehat{\Delta T^2}]$ is not trivial. The denominator is the estimation of σ_1^2 defined in Eq. 7.10. Here, we first assume σ_1^2 can be estimated perfectly, that is, σ_1^2 is known. The denominator in the above equation is then constant and the expectation of $\widehat{\Delta T^2}$ is

$$E[\widehat{\Delta T^2}] = \frac{E\left[\frac{1}{2M} \sum_{l=1}^M \hat{z}_l^2 - 2\hat{\sigma}_n^2\right]}{\sigma_1^2} = \frac{\sigma^2}{\sigma_1^2} \quad , \quad (7.18)$$

where σ^2 is defined in Eq. 7.5. If the linear approximation of $\beta_k(T)$ is perfect, $\sigma^2 = \Delta T^2 \sigma_1^2$ and $E[\widehat{\Delta T^2}] = \Delta T^2$. Unfortunately, the Taylor expansion of β_k contains non-linear components of ΔT

$$\begin{aligned} \beta_k(T) &= \beta_k(T_0) + \Delta T \beta'_k(T_0) + \frac{\Delta T^2}{2} \beta_k^{(2)}(T_0) + \dots + \frac{\Delta T^n}{n!} \beta_k^{(n)}(T_0) + \dots \\ &= \beta_k(T_0) + \Delta T \beta'_k(T_0) + \Delta T \varepsilon(\Delta T) \quad , \end{aligned} \quad (7.19)$$

where $\Delta T \varepsilon_k(\Delta T)$ represents higher order components in the Taylor expansion of β_k . Therefore, Eq. 7.3 can be written as

$$\begin{aligned} z &= \left| \sum_{k=1}^N (\beta_k(T) - \beta_k(T_0)) A_k(T_0) e^{j\phi_k} \right| \\ &= \Delta T \left| \sum_{k=1}^N [\beta'_k(T_0) + \varepsilon(\Delta T)] A_k(T_0) e^{j\phi_k} \right| \\ &= \Delta T w \quad , \end{aligned} \quad (7.20)$$

where $w = \left| \sum_{k=1}^N [\beta'_k(T_0) + \varepsilon(\Delta T)] A_k(T_0) e^{j\phi_k} \right|$ is also Rayleigh random variable with parameter σ_w^2 and $\sigma^2 = \Delta T^2 \sigma_w^2$. σ_w^2 varies with temperature due to the term $\varepsilon(\Delta T)$ in Eq. 7.20 and Eq. 7.18 becomes

$$E[\widehat{\Delta T^2}] = \frac{\Delta T^2 \sigma_w^2(\Delta T)}{\sigma_1^2} \quad .$$

This result shows that the estimator has a time variant bias even when σ_1^2 is known. Notice that if β_k contains only linear terms in its Taylor expansion, then $\varepsilon(\Delta T) = 0$, $\sigma_w^2 = \sigma_1^2$ and the estimator is unbiased. Because β_k contains nonlinear terms, the MLE

is biased and the linearization of β_k could be a major cause of bias in temperature imaging. Because β_k depends on the type of scatterers, the estimation bias relates to scatterer population.

Furthermore, σ_1^2 is usually unknown and the denominator of Eq. 7.17 is also a random variable. In addition, the denominator and numerator in Eq. 7.17 are correlated. Both of them are the difference of two Chi-square random variables and follow a complicated distribution [88]. It is difficult to determine their joint distribution. It is, however, intuitive that the joint distribution may depend on the correlation between the denominator and numerator, which varies with SNR since \check{z}_m and \check{z}_{1m} are noisy signals. Consequently, the mean of the estimator may be affected by SNR. It is difficult to see the noise impact on the estimator mean analytically. Bias with SNR was studied using simulation tools as shown below.

Estimator variance

A good maximum likelihood estimator requires small variance, which may be evaluated by Cramér-Rao bound (CR bound). According to the Cramér-Rao bound for biased estimators in [99], the variance of our estimator satisfies

$$\text{Var}(\widehat{\Delta T}) \geq \left(1 + \frac{dB(\Delta T)}{d\Delta T}\right)^2 \frac{1}{E\left[\left(\frac{\partial \ln L(T)}{\partial \Delta T}\right)^2\right]}, \quad (7.21)$$

where $L(T)$ is given in Eq. 7.7, while z_l and σ^2 are replaced by \check{z}_l and $\sigma_{\check{z}}^2$, respectively, to count the noise effect. Therefore,

$$\frac{\partial \ln L(T)}{\partial \Delta T} = \frac{\partial \sigma_{\check{z}}^2}{\partial \Delta T} \frac{-M\sigma_{\check{z}}^2 + \frac{1}{2} \sum_{l=1}^M \check{z}_l^2}{\sigma_{\check{z}}^4}, \quad (7.22)$$

where $\sigma_{\check{z}}^2 = \sigma^2 + 2\sigma_n^2$. Therefore,

$$\left[\frac{\partial \ln L(T)}{\partial \Delta T}\right]^2 = \frac{1}{\sigma_{\check{z}}^8} \left[\frac{\partial \sigma_{\check{z}}^2}{\partial \Delta T}\right]^2 \left[M^2 \sigma_{\check{z}}^4 - M \sigma_{\check{z}}^2 \sum_{l=1}^M \check{z}_l^2 + 0.25 \left(\sum_{l=1}^M \check{z}_l^2 \right)^2 \right]. \quad (7.23)$$

As defined previously, σ^2 is the Rayleigh parameter of z in Eq. 7.3 and σ_n^2 is the variance of noise in RF images. Given

$$E(\check{z}_l^2) = 2\sigma_z^2 \quad ,$$

$$E(\check{z}_l^4) = 8\sigma_z^4 \quad ,$$

we have

$$E \left[\left(\frac{\partial \ln L(T)}{\partial \Delta T} \right)^2 \right] = \frac{M}{\sigma_z^4} \left[\frac{\partial \sigma_z^2}{\partial \Delta T} \right]^2 . \quad (7.24)$$

Accordingly,

$$\begin{aligned} Var(\widehat{\Delta T}) &\geq \left(1 + \frac{dB(\Delta T)}{d\Delta T} \right)^2 \frac{\sigma_z^4}{M \left[\frac{\partial \sigma_z^2}{\partial \Delta T} \right]^2} \\ &\cong \left(1 + \frac{dB(\Delta T)}{d\Delta T} \right)^2 \frac{(\frac{\sigma^2}{\sigma_n^2} + 2)^2 \Delta T^2}{4M \left[\frac{\sigma^2}{\sigma_n^2} \right]^2} , \end{aligned} \quad (7.25)$$

where noise is assumed to be temperature invariant and $\sigma^2 \cong \Delta T^2 \sigma_1^2$ by approximating β_k as in the development of MLE. Obviously, the estimator variance increases with temperature, ΔT . On the other hand, if M is large, i.e., the size of images increases, variance is smaller. Smaller variance due to larger image size is reasonable because more samples are involved and provide better estimation of the statistics. Notice that $\frac{\sigma^2}{\sigma_n^2}$ represents the signal to noise ratio. When SNR is large, the CR bound is mainly determined by ΔT and M . When SNR is very small, the denominator decreases rapidly, whereas the numerator is bounded by $4\Delta T^2$. Therefore, we can conclude that the estimator variance decreases with SNR or increases with noise level, which is consistent with our intuition.

In summary, the mean and variance of the MLE are affected by several factors. The population of the scatterers, i.e., the type and proportion of scatterers, affects the bias of the estimation mean resulted from the linearization of the reflectivity parameter β_k . The bias also increases with temperature because β_k contains more higher order components when temperature is high. Estimator variance increases with temperature, but decreases with image size and SNR.

7.2.4 Temperature Imaging using MLE – Simulation Results

In this subsection, we evaluate the performance of the maximum likelihood estimator in Eq. 7.16 using the simulation tool. As discussed in the preceding subsection, scatterer population, SNR and image size may affect estimator performance. In this study, we simulated sequences of ultrasonic images with varying values for SNR, image size and proportion ratio for aqueous and lipid scatterers. Baseline values for SNR, image size and population are 29dB, $1 \times 3\text{cm}^2$ and 2:1 N_a/N_l ratio, where N_a and N_l are the numbers of aqueous and lipid scatterers, respectively. The scatterers were assumed to be uniformly distributed over the image region. Following the setting in our *in-vitro* heating experiments, the temperature range was chosen to be $37 \sim 45^\circ\text{C}$ with 0.5°C intervals.

Figs. 7.7 shows simulated envelope images of signal differences at various temperatures. As expected, the variance, σ^2 in Eq. 7.5, of these difference images increased with temperature, such that it can be used for temperature imaging.

We first applied MLE to simulated image sequences at various SNRs that were typically seen in *in-vitro* experiments. Fig. 7.8 shows mean \pm standard deviation of errors in estimation from 50 trials with $N_a/N_l = 2$ and image size $1 \times 3\text{cm}^2$. Notice that, in the development of MLE, we assumed the image at $\Delta T = 1$ is known. In the simulations, estimation was performed for temperatures above 38°C and errors at $37 \sim 38^\circ\text{C}$ were set to be zero.

It can be seen that the estimation is biased and the bias increases with temperature, which is consistent with the analysis in the previous section. The bias at SNRs of 23 and 29dB are similar, while the bias at SNR of 17dB is even smaller. Further studies are needed to explore the impact of noise on the bias.

As discussed in the preceding subsection, the variance in estimation decreases with SNR. When SNR is as low as 17dB, the range of the mean \pm STD may be larger than $\pm 0.5^\circ\text{C}$ after 42°C . Otherwise, the error in temperature estimation is less than $\pm 0.5^\circ\text{C}$. This result shows that, although noise has been taken into account, MLE is not completely SNR independent because estimation of MLE parameters, such as σ_1 in Eq. 7.16, is affected by noise. This again reminds us of the significance of noise reduction.

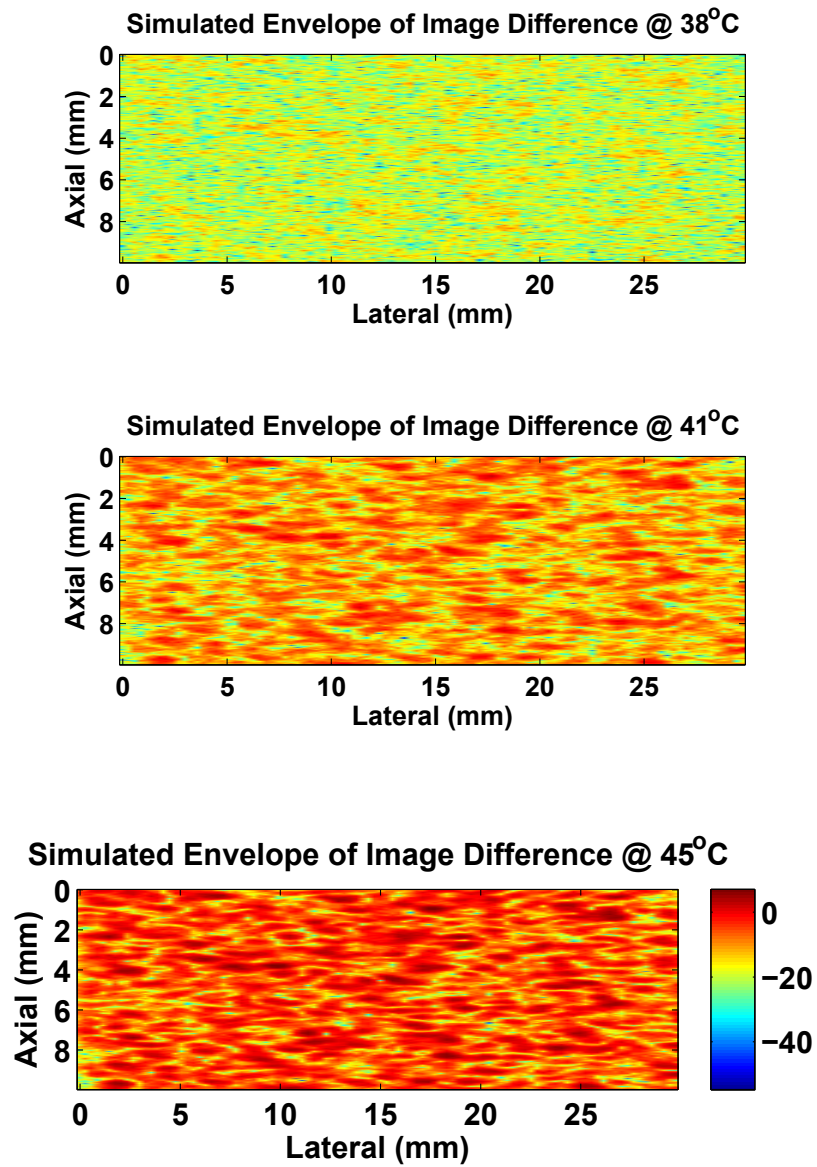


Figure 7.7: Simulated envelope images of the signal difference of the reference image and images at various temperatures. Top: 38°C. Center: 41°C. Bottom: 45°C. Color scale is in dB.

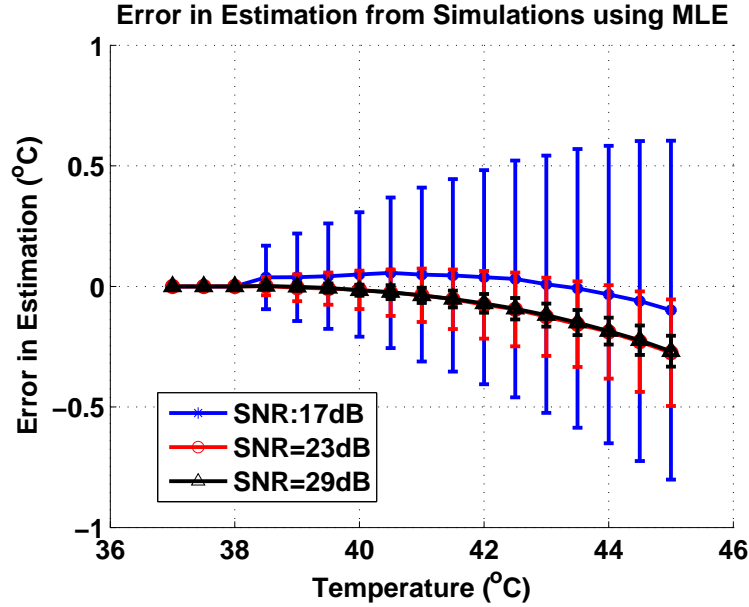


Figure 7.8: Error in temperature estimation using MLE at various SNRs. Mean \pm STD of 50 trials.

In the previous discussion, we found that scatterer population affects both the bias and variance of the estimator. In this study, following [103], we applied MLE to image sequences generated with $N_a/N_l = 2 : 1$ and $N_a/N_l = 1 : 1$, and baseline values for SNR and image size. Mean \pm standard deviation of the estimation error from 50 trials is plotted in Figs. 7.9.

Estimation biases at $N_a/N_l = 2 : 1$ and $N_a/N_l = 1 : 1$ are obviously different, which confirms our analysis. Estimation variance at $N_a/N_l = 2$ is slightly larger than that at $N_a/N_l = 1$. This increase occurs because the bias at $N_a/N_l = 2$ changes more with temperature and thus the term $\frac{dB(\Delta T)}{d\Delta T}$ in Eq. 7.21 is larger resulting in larger variance.

Estimation variance may also be affected by the size of images. Fig. 7.10 shows estimation error with different image sizes. Biases are same in the results, while the estimation variance is slightly larger when image size is smaller, which is consistent with our analytical discussion in previous subsection.

The simulation results verified the analysis in the previous subsection. We would point out that estimation variance is largely affected by SNR. If SNR can be controlled

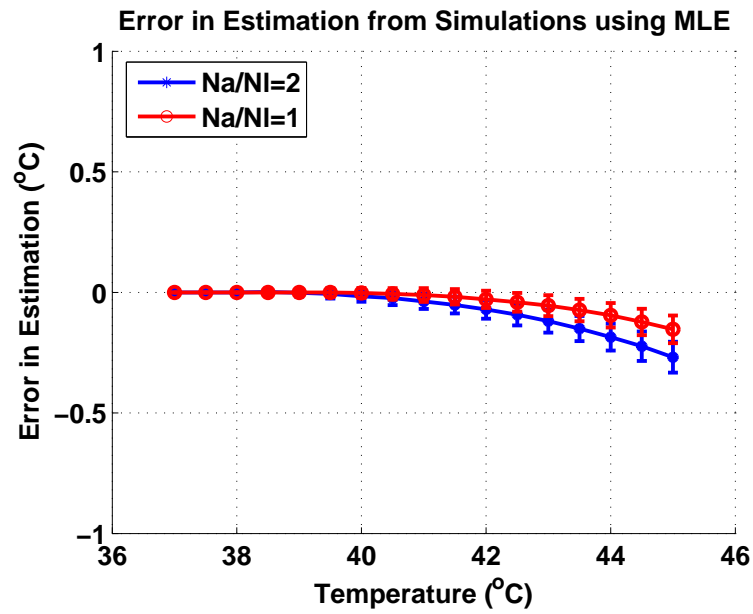


Figure 7.9: Error in temperature estimation using MLE at two scatterer proportions. Mean±STD of 50 trials.

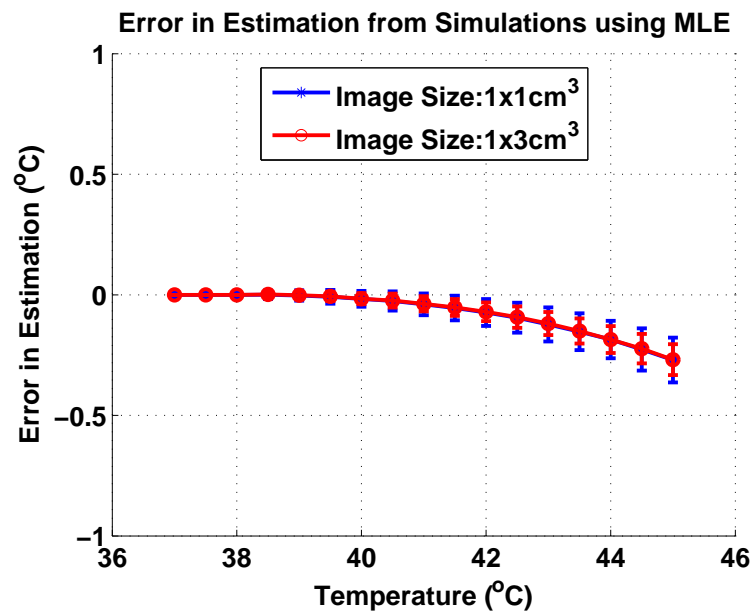


Figure 7.10: Error in temperature estimation using MLE at two image sizes. Mean±STD of 50 trials.

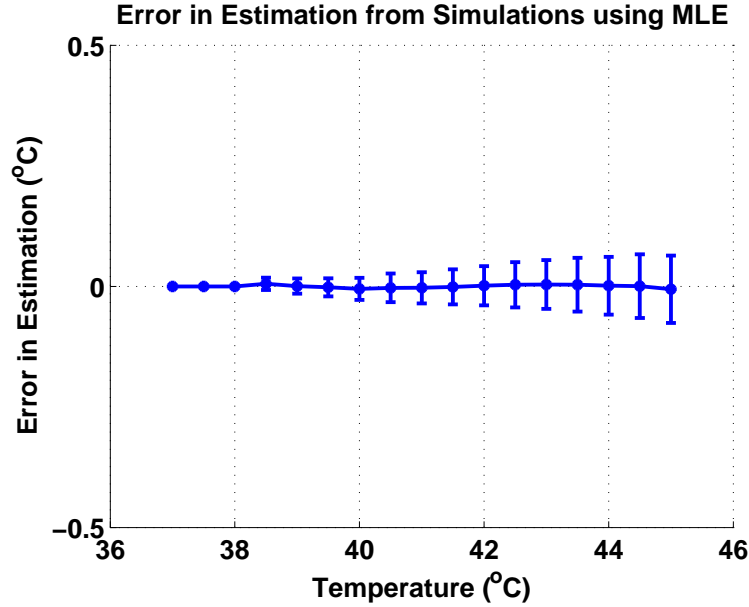


Figure 7.11: Error in temperature estimation using MLE with calibration for bias. Mean \pm STD of 50 trials. SNR:29dB. Image size:1x3cm². $N_a/N_l = 2$.

to 29dB or above, the standard deviation of estimation could be less than 0.1°C . Approaches to increasing SNR were discussed in Chapters 3 and 5. The bias was affected by both SNR and scatterer proportion. We assumed scatterer proportion varies little for the same type of tissue and SNR can be kept at or above 29dB. In this case, the mean bias of the estimator remains the same. As an initial attempt at reducing bias, we generated images with baseline settings, calibrated the $\widehat{\Delta T}$ curves with respect to true ΔT , assuming true values are known. The calibration curve was then used to estimate temperature from another group of images. The error of calibrated estimation from 50 trials is shown in Fig. 7.11. The bias was largely reduced by calibration.

The above results show that the MLE is a potential estimator for temperature imaging. Looking at Eq. 7.16, the numerator and denominator are actually estimations of σ^2 at $\Delta T =$ and > 1 , respectively, which are equivalent to the energy of the difference image. In other word, we were evaluating temperatures using the energy of change in the signals. Therefore, the idea of maximum likelihood estimator is consistent with temperature imaging from CBE in principle, because both of them are based on the model of CBE for individual scatterers developed in [92]. The advantages of using

MLE are: 1) computing the difference does not generate "outliers" as in ratios, 2) it is easier to find distributions for the envelope of the difference, 3) we may be able to find a relation between data and temperature that allows us to analytically discuss estimator performance.

7.3 Summary and Conclusions

In this chapter, we discussed estimating temperature from joint distributions between signals. Mutual information and correlation were examples of parameters that may be computed from the joint distribution. This study was an initial look at the potential of temperature imaging from signal joint distributions. More studies are needed for more comprehensive approaches to optimal solutions.

By linearizing the random phasor sum representation, we developed a maximum likelihood estimator for temperature assuming uniformly distributed scatterers. Analytical analysis and simulation results show how SNR, image size and scatterer proportion affect MLE performance. Scatterer population cannot be controlled, so that more investigations are necessary for approaches to reducing bias other than by calibration in cases for which scatterer proportion varies. Image size has less effect than the other two factors and is usually determined by application, so it will not be discussed further. SNR plays an important role in the estimation.

Chapter 8

Investigation of Experimental Applications of the Framework

In previous chapters, we developed a framework for temperature imaging using the change in backscattered signals. Our former approach using energy ratio was formalized. Two other examples of temperature estimator other than energy ratio, mutual information and a maximum likelihood estimator, were investigated. Simulation results showed that temperature accuracy was improved using these methods. For the framework to be meaningful, its results should be able to be applied to experimental data.

As shown in Chapter 5, in addition to noise and motion, change in signals may also be caused by degradation of tissue in the medium or by imaging system variation. In clinical application, degradation is not likely to happen in living tissue. Changes caused by variation in the imaging system could be avoided by modifying hardware or changing the image formation method. These changes require cooperation with system provider. On the other hand, signal changes caused by these reasons could be dominated by thermal change when tissue is heated. Therefore, we did not consider these effects in this work.

We have shown that motion in images has significant impact when comparing signals. There are two ways to handle motion effects: 1) model motion effects in the framework. 2) compensate motion in the images. In this work, we followed the second consideration. In Chapters 3 and 5, we showed motion can be compensated well. Here, we assume motion compensation is good enough such that the residual effect of motion is dominated by thermal changes in the signals. Our framework does not

take motion into account for now, but it may be extended or modified to encompass motion effect in the future.

There are two other issues we need to face when applying the mutual information (MI) and maximum likelihood estimator (MLE) methods to experimental data. First, the scatterers are not uniformly distributed in real tissue, which was assumed in previous chapters. Second, due to the first issue, we may not be able to take noise into account in the framework, and thus SNR has significant impact on both MI and MLE performance.

The envelope images of real tissue can not be described by Rayleigh distribution since the scatterers are not uniformly distributed. In Chapter 6, we showed that generalized Gamma (GG) or generalized Nakagami (GN) distributions match the histogram of B-scans from turkey muscle. Therefore, the random variables involved in the ratio in Eq. 6.17 follow the GG distribution shown in Eq. 6.15. The ratio distribution is determined by their joint distribution as in Eq. 6.16. Although it may be possible [13], computing ratio PDF from the joint distribution is complicated. In order to compute CBE independent of SNR as for the Rayleigh case, an appropriate choice of ratio distribution and a smart way of estimating distribution parameter are required. Exploring the ratio PDF for GG random variables can be part of future work. Below, we discuss the possibility of computing mutual information and applying the maximum likelihood estimator to experimental data.

8.1 Computation of Mutual Information from the Data Histogram

In the last chapter, we computed mutual information as a function of correlation coefficient between RF images, assuming uniformly distributed scatterers. Noise can be taken into account and thus MI can be calculated independent of SNR. When considering experimental data, computing MI analytically from RF or envelope images is difficult because of the complex form of their joint distributions as shown in Eq. 6.14 and 6.16. In image registration problems, mutual information is alternatively computed from marginal and joint histograms of two images [89]. Here, we computed MI

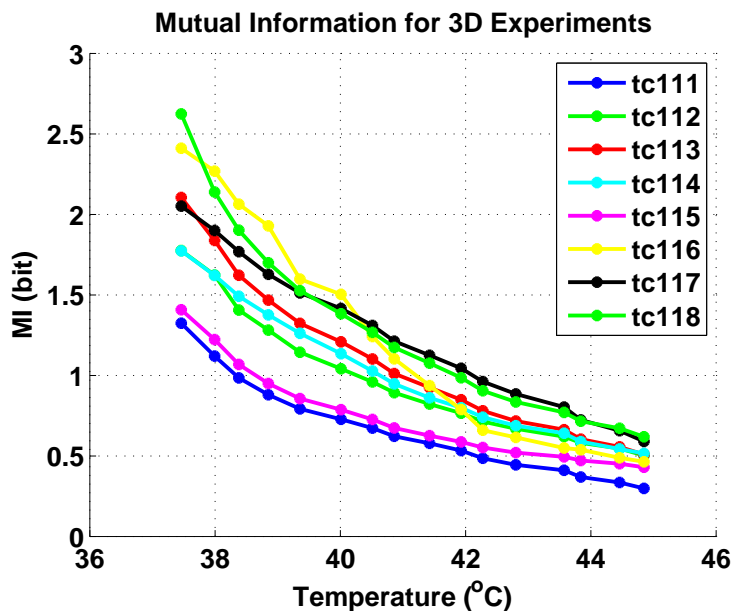


Figure 8.1: Mutual information computed from the histograms of envelope-detected images acquired in 3D heating experiments.

with temperature using histograms of envelope images of 3cm^3 turkey breast volumes from eight 3D heating experiments. The results are plotted in Fig. 8.1.

There is obvious variation among MI curves from experiments. A likely cause of this variation is the noise effect. Histograms used in MI computation were generated from the noisy data. Therefore, MI curves depend on SNR. If SNR varies among experiments, which was usually the case, MI curves also vary. To illustrate the effect of SNR on MI, we simulated images at various SNRs and computed MI using histograms. MI curves are plotted in Fig. 8.2.

The results in the above figure demonstrate the apparent impact of SNR on MI computation. To reduce this impact, SNR needs to be increased. In addition, it is desired that all experiments have similar SNR to reduce variation in MI curves. From results of Chapter 5, increasing and keeping SNR consistent are possible if we can implement signal averaging for 3D heating experiments.

The choice of bin width for generating histograms also has impact on MI computation. Our signals were represented by continuous values after motion compensation and thus there was no natural choice of the bin width for histograms. In order to

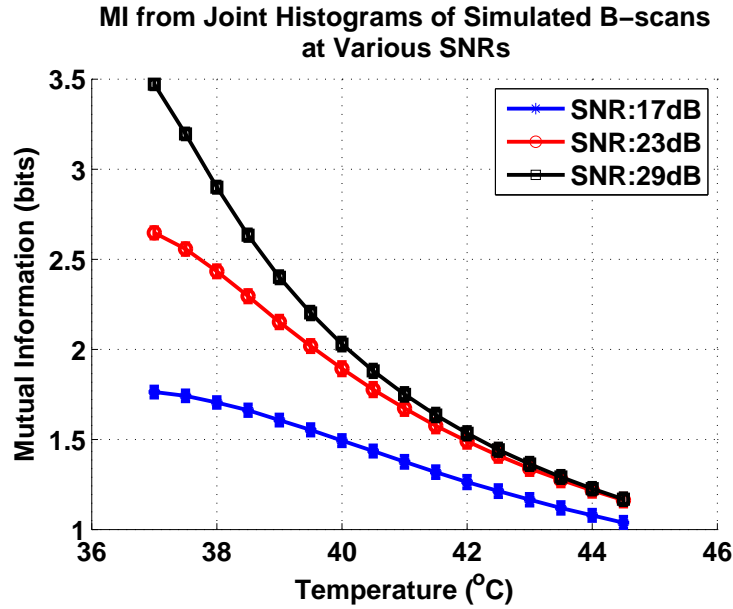


Figure 8.2: Mutual information computed from the histograms of simulated B-scans at various SNRs.

demonstrate the effect of the bin width, we simulated images for uniformly distributed scatterers, and computed mutual information using both the PDF in Eq. 7.1 and the joint histograms. Fig. 8.3 shows the variation of MI curves with the bin width of the histograms. There seems to be an "optimal" bin width for MI computation so that MI values are consistent with MI computed from the PDF. Differences in the "optimal" bin width among experiments may also cause variation in MI calculation. How to choose the bin width for histograms could be part of future work.

In this section, we showed that MI can be computed from experimental data using histograms. However, SNR and choice of bin width of histograms may cause variation in measured MI. Work in previous chapters showed that it is possible to reduce SNR effects once we can implement signal averaging for 3D heating experiments. A smart way of choosing bin width for histograms is desired as future work. From the results in section, it can be seen that MI is sensitive to signal de-correlation caused by noise. Hence, we do not rule out other possible causes of signal de-correlation, such as residual motion effects after motion compensation.

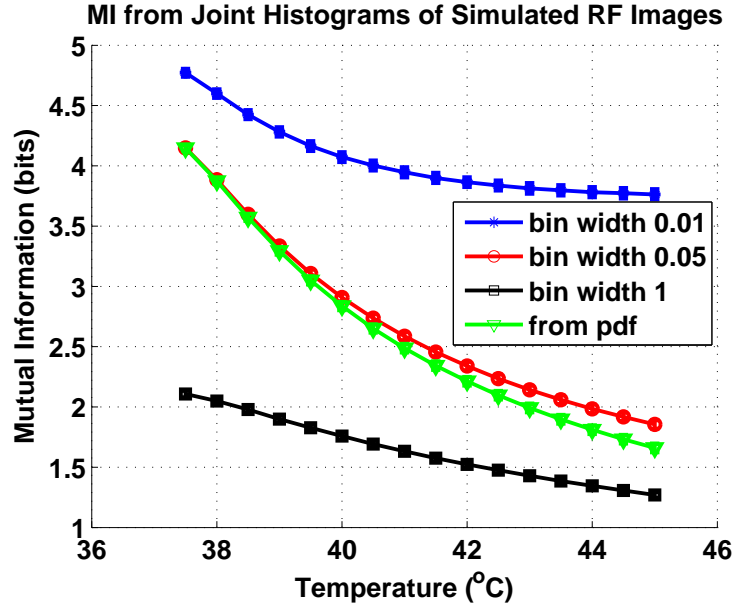


Figure 8.3: Mutual information computed from joint histograms of RF images at SNR=29dB with different bin widths.

8.2 Application of the Maximum Likelihood Estimator to Experimental Data

In the previous chapter, in deriving the maximum likelihood estimator (MLE), we looked at the difference between the random phasor sums (RPS) representing images at current and reference temperatures. This difference is still a random phasor sum. As mentioned above, for experimental data, the magnitude of the random phasor sum does not fit a Rayleigh distribution, but does fit the generalized Gamma (GG) well. Hence, the magnitude of RPS difference can also be modeled by a generalized Gamma distribution. The difference magnitude, z , was previously approximated as

$$z \cong \Delta T \left| \sum_{k=1}^N \beta'_k(T_0) A_k(T_0) e^{j\phi_k} \right| = \Delta T u \quad ,$$

where $u = \left| \sum_{k=1}^N \beta'_k(T_0) A_k(T_0) e^{j\phi_k} \right|$ and u follows generalized Gamma distribution

$$f(u) = \frac{pu^{pm-1} \exp\left(-\left(\frac{u}{a}\right)^p\right)}{a^{pm}\Gamma(m)} \quad . \quad (8.1)$$

From the properties of GG random variables [90], if $u \sim f(u; a, m, p)$, then $w = ku \sim f(w; ka, m, p)$. Therefore, distribution of z is

$$f(z) = \frac{pz^{pm-1} \exp\left(-\left(\frac{z}{\Delta T a}\right)^p\right)}{(\Delta T a)^{pm}\Gamma(m)} \quad . \quad (8.2)$$

The likelihood function in Eq. 7.7 now becomes

$$L(T) = \frac{p^M \left(\prod_{l=1}^M z_l \right)^{pm-1} \exp\left[-\frac{1}{(\Delta T a)^p} \sum_{l=1}^M z_l^p\right]}{(\Delta T a)^{pmM}\Gamma(m)^M} \quad . \quad (8.3)$$

Log likelihood function is then

$$\ln L = M \ln p + (pm-1) \ln \left(\prod_{l=1}^M z_l \right) - \frac{1}{\Delta T^p} \left(\frac{1}{a^p} \sum_{l=1}^M z_l^p \right) - pmM \ln \Delta T - pmM \ln a - M \ln \Gamma m. \quad (8.4)$$

Differentiating the log likelihood function with respect to ΔT and setting it to zero lead to

$$\frac{\partial \ln L}{\partial \Delta T} = \frac{1}{\Delta T^{p+1}} \left(\frac{p}{a^p} \sum_{l=1}^M z_l^p \right) - \frac{pmM}{\Delta T} = 0 \quad . \quad (8.5)$$

The MLE for temperature change is found as

$$\widehat{\Delta T} = \left[\frac{1}{a^{pmM} \sum_{l=1}^M z_l^p} \right]^{\frac{1}{p}} \quad . \quad (8.6)$$

The above estimator is in fact a scaled L_p norm of z . When $m = 1$, $p = 2$ and $a = \sqrt{2}\sigma$, GG distribution reduces to a Rayleigh distribution with parameter σ . Accordingly, the L_p norm becomes L_2 norm and Eq. 8.6 reduces to the MLE based on a Rayleigh distribution as in Eq. 7.14.

When applied to experimental data, MLE parameters need to be estimated from noisy signals. Notice that, the effect of noise was not considered in the estimator in Eq. 8.6

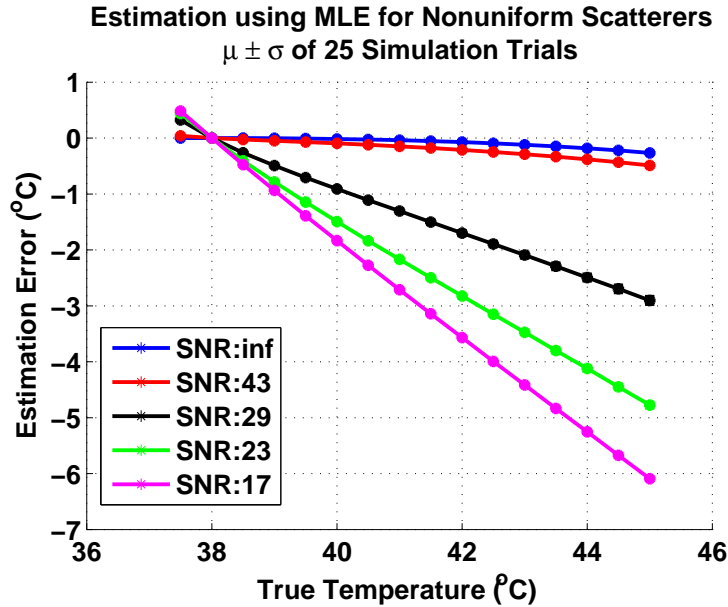


Figure 8.4: Error in temperature estimation for simulated images of non-uniformly distributed scatterers at various SNRs using MLE.

because the GG distribution is a direct generalization of the Rayleigh distribution. The impact of noise on GG parameters is not clear and to our knowledge there is no apparent approach to estimating these parameters from noisy data. Therefore, it is expected that we will see significant impact of SNR on the estimation of these parameters and thus on temperature imaging.

To see SNR effects on temperature estimation, images of non-uniformly distributed scatterer were simulated as in Fig. 6.4 at various SNRs. Since scatterer density in the left half is higher than that in the right half, the overall distribution is not Rayleigh, but generalized Gamma as shown in Fig. 6.6. The estimator in Eq. 8.6 was applied to the simulated images and errors in temperature estimation plotted in Fig. 8.4.

The results in Fig. 8.4 show that, when SNR is as high as $43dB$, performance of MLE is very good and estimation error at $45^{\circ}C$ is about $0.5^{\circ}C$. When SNR is reduced to $17 - 23dB$, the error in estimation, however, is between $4.8 - 6^{\circ}C$ at $45^{\circ}C$. The effect of SNR on temperature estimation is significant. To see the performance of MLE for real data, we applied it to the images from the 3D heating experiments. Errors in temperature estimation are shown in Fig. 8.5.

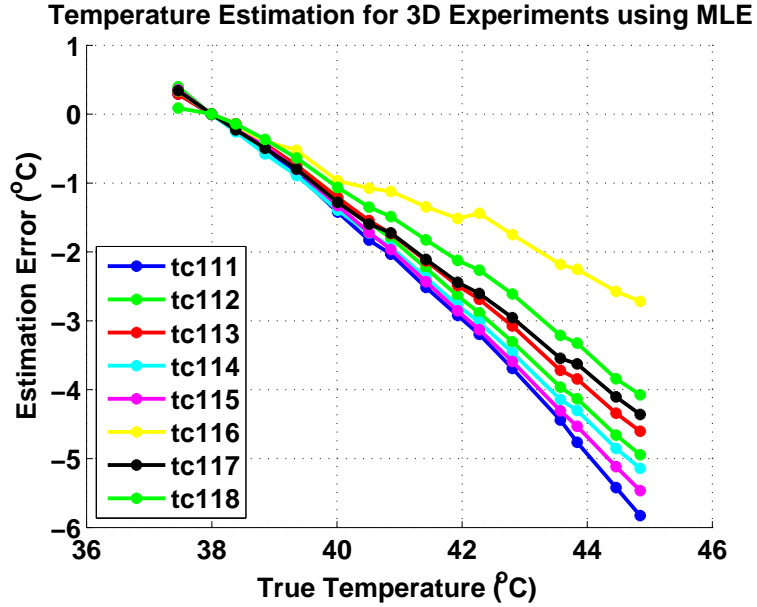


Figure 8.5: Error in temperature estimation for 3D heating experiments using MLE.

For most experiments, the error around $45^{\circ}C$ is between $4 - 6^{\circ}C$. Noticing that SNR of these experiments varied between 18 to $25dB$, the error in temperature estimation for experiments using MLE is consistent with the simulation results shown above. Hence, it is very likely that the large error in Fig. 8.5 is caused by noise, which can be reduced significantly if we can increase SNR of experimental data to about $43dB$ by, for example, signal averaging.

A special view of signals from non-uniformly distributed scatterers

We proposed a theory in Chapter 6 to explain why the histogram of experimental B-scans is not Rayleigh. Each pixel was still represented by a Rayleigh random variable, but with a distinct parameter. The histogram of non-identical random variables does follow a Rayleigh distribution, but a more general one. According to this theory, the likelihood function in Eq. 7.7 for i.i.d. pixels is modified for non-i.i.d. pixels as

$$L(T) = \frac{\prod_{l=1}^M z_l}{\prod_{l=1}^M \sigma_l^2} \exp\left(-\frac{1}{2} \sum_{l=1}^M \frac{z_l^2}{\sigma_l^2}\right), \quad (8.7)$$

where l is the index of image pixels. Because ideas embodied in Eqs. 7.8 to 7.11 are now valid for each pixel, we have

$$\sigma_l^2 \cong \Delta T^2 \sigma_{1l}^2 \quad ,$$

where σ_{1l}^2 is the value of σ_l^2 at $\Delta T = 1$. The likelihood function is approximated

$$L(T) = \frac{\prod_{l=1}^M z_l}{\prod_{l=1}^M \Delta T^2 \sigma_{1l}^2} \exp \left(-\frac{1}{2} \sum_{l=1}^M \frac{z_l^2}{\Delta T^2 \sigma_{1l}^2} \right) \quad . \quad (8.8)$$

Given

$$\frac{\partial L}{\partial \Delta T} = 0 \quad ,$$

a maximum likelihood estimator for ΔT can be derived

$$\Delta T = \sqrt{\frac{1}{2M} \sum_{l=1}^M \frac{z_l^2}{\sigma_{1l}^2}} \quad . \quad (8.9)$$

Eq. 8.9 is a theoretical result, but σ_{1l}^2 , the parameter of the distribution for the l^{th} pixel cannot be estimated accurately from a single sample. For the same reason, it is difficult to remove noise effects. One possible approach to estimating σ_{1l}^2 is to make use of the pixels in the neighborhood of the l^{th} pixel, which means considering the dependence among pixels. More consideration of this notion is presented in the next chapter.

8.3 Summary and Conclusions

In this chapter, we studied the application of results from the framework to experiments, especially the application of mutual information and the maximum likelihood estimator. Although these studies showed that these approaches are not yet ready to be used for experiments because of the obstacle presented by the effects of noise. This obstacle can be overcome by increasing SNR. One approach we have shown to be effective at increasing SNR is signal averaging, but these methods cannot be

implemented with our present imaging instruments. Once these methods can be implemented for 3D heating experiments, it is highly likely that temperature can be estimated accurately using MI or MLE. Furthermore, application of MI and MLE are examples of temperature imaging other than the energy ratio. We do not rule out other possible approaches.

Chapter 9

Conclusions and Future Work

9.1 Conclusions

This dissertation extended the initial studies on temperature imaging for hyperthermia using the change in backscattered energy. Approaches to noise reduction were not implemented and motion compensation algorithms were not evaluated in our initial works. The mathematical representation of our method presented here is the first formal representation for CBE based thermometry. It made it possible to investigate potential temperature estimators using changes in backscattered signals other than the energy ratio.

In chapter 3, we implemented noise reduction approaches by signal averaging and thresholding in simulations, assuming additive white Gaussian noise. In chapter 5, these approaches were applied to image loops acquired in null experiments. Successful reduction of noise with an accompanying increase of SNR for experiment data showed that the assumption of additive Gaussian noise is valid. Thus noise effects can be handled in experimental environments. That is, we can increase SNR to maintain experiments at the same SNR, and therefore improve calibration of CBE and temperature accuracy.

Motion compensation algorithms were evaluated using simulations in chapter 3 and were shown to be able to correct for motion effects. It was also found that both interpolation methods and sampling rate affect the performance of motion compensation algorithms. In chapter 5, these observations were confirmed in null experiments, during which known motion was added to images of turkey breast.

The studies on reducing effects of noise and motion benefit not only the temperature imaging methods developed in our initial work, but also the development of the framework. For example, we may assume motion compensation works well enough so that motion effect does not need to be considered in the framework. It also makes the mathematic work simpler. In addition, we have seen that SNR has an apparent impact on applications of the framework, such as temperature imaging with MI and MLE. The ability of increasing SNR, e.g., by signal averaging, makes it possible to apply the framework to experimental data.

In chapter 6, we developed a mathematical representation of our approach to temperature imaging. Temperature imaging was modeled via a probabilistic framework. Computation and characterization of CBE were formalized, which improved temperature estimation in simulations of uniformly distributed scatterers. In chapter 7, we extended our view beyond the energy ratio to other possibilities, e.g., mutual information and maximum likelihood estimator. Both MI and MLE showed improvements in temperature accuracy compared to the energy ratio from the signal mean in simulations. Although the approaches developed in these two chapters work well in simulations, they required special assumption on scatterer distributions. These chapters showed the potential of improving temperature imaging with the framework.

Investigations in Chapter 8 showed high likelihood of success in applying the framework in experimental environments, if we have enough resource to implement noise reduction approaches. According to the results in Chapter 8, in order to reach the temperature accuracy of $\pm 0.5^{\circ}C$, SNR needs to be maintained above a certain level for each of the methods discussed in this work. Possible values of these required SNRs, above which the "mean \pm standard deviation" of the estimate is within $\pm 0.5^{\circ}C$, are summarized in table 9.1.

When the scatterers are uniformly distributed, the methods from the framework, i.e., PCBE from the ratio PDF, MI and MLE, allow lower SNR than the method using PCBE from ratio mean, because they take noise information into account in the estimation. It seems the MLE requires similar SNR to our former methods. This is because the MLE is biased due to the linearization of the random phasor sum representation. If the bias can be compensated, the MLE can allow lower SNR, since the standard deviation of the MLE at 23dB SNR is only $0.25^{\circ}C$. Reduction of MLE

bias will be discussed in the future work in Section 9.3. Furthermore, SNR for MLE in this table was generated without calibration, which is an advantage of using MLE over using MI and CBE.

When the scatterers are non-uniformly distributed, applications of MI and MLE with desired temperature accuracy require higher SNR because, currently, we are not able to take noise into account in the estimation. If SNR can be increased to the levels shown in the table, it is likely that the $\pm 0.5^\circ C$ accuracy can be reached. In addition, if we can estimate parameters of the generalized Gamma distribution from noisy signals, the requirement of SNR for MLE can be reduced. On the other hand, our former method using PCBE from the ratio mean does not require SNR to be much higher and therefore is still the appropriate method for experimental data for now.

Table 9.1: SNR for Temperature Accuracy of $\pm 0.5^\circ C$

TI Method	PCBE from ratio mean	PCBE from ratio PDF	MI from RF images	MLE $N_a/N_l = 2$
Uniform Distribution	25	17	20	23
Non-uniform Distribution	30	X	35	45

N_a/N_l is the ratio of aqueous to lipid scatterers

Results in the above table are from simulations and can be used as reference for SNR requirements. There are other factors which impact temperature accuracy, such as residual motion effects. When CBE and MI are fitted to a polynomial for temperature imaging, the order of the polynomial may affect temperature accuracy. In this work, the polynomial for CBE was 2^{nd} order and that for MI was 3^{rd} order. For images from non-uniformly distributed scatterers, MI is computed from data histograms and is affected by the bin width of the histograms. In the table, the SNR of $35dB$ was determined by choosing bin width as 0.5 for RF images which were simulated as in Fig. 6.4. When signal range changes, the choice of bin width may change. Developing a systematic way to find the optimal bin width for computing the MI can be part of the future work. For the MLE, notice that simulations were done with $N_a/N_l = 2$. When the scatterer population changes, the results in the table also change.

The main contributions of this work are summarized below. We

1. Developed and verified noise reduction approaches and discovered factors affecting CBE measurement that were unknown before, specifically, tissue degradation and change due to the imaging system,
2. Evaluated motion compensation algorithms,
3. Created a framework for temperature imaging using the change in backscattered signals; developed mathematical representation of our approach to temperature imaging; formalized CBE computation and characterization; and investigated approaches to CBE temperature imaging beyond the energy ratio,
4. Investigated the application of the framework to experiments.

9.2 Further Work on Noise and Motion Reduction

In future studies, noise reduction procedure needs to be implemented for 3D heating experiments. Recall that, for 3D experiments, a set of 30 2D images were acquired at each temperature. In order to perform signal averaging, each of these 2D images should be replaced by an image loop that contains around 150 frames. If stored on computer, these files may use around 90G bytes in Matlab data format. Although it is not impossible to average files on a hard drive, it is inefficient. In addition, saving loops to hard drive may cost more time for data acquisition during which tissue temperature may vary. Alternatively, signal averaging may be done online during the time interval between two temperatures (two acquisitions). Our Matlab control program, however, can not process data directly before saving them to files and converting them to the Matlab data format. Furthermore, we hope to be able to control the number frames in a loop. These requirements for online processing need cooperation with Teratech Inc., the provider of imaging system.

We have shown motion in images can be detected and compensated well, although better performance is always desired. Currently, the optimization function in Matlab is used for maximizing correlation between two images. An implementation of the optimization algorithm specific to our problem may produce faster convergence. In

future *in-vivo* experiments, motion in images could be highly non-rigid over large volumes. Current algorithms may need modifications, e.g., to model nonlinear motion over large region, or to change reference during an experiment. Furthermore, the residual effect of motion after compensation may be considered as disturbance in the phase of the phasors in the random phasor sum model. Hence, the motion effect could be incorporated into the framework. The disadvantage of doing so is that the framework becomes more complicated.

9.3 Further Development of the Framework

The framework studied in this work is a first step of the theoretical development for temperature imaging using the change in backscattered signals. More effort is needed to make it more comprehensive and complete. For example, as mentioned before, the temperature dependent random phasor sum model may be modified to account for residual motion effects.

For real tissue images, modeling the energy ratio from joint generalized Gamma distributions may need more refined mathematical work [13]. Alternatively, it is helpful to find a simple form for the ratio PDF, which can be used for experimental data.

Mutual information has been used as an example of temperature imaging using joint distribution. However, we do not know if it is the best method and there could be other possible choices. For example, we have seen that the joint histogram spreads away from its diagonal with temperature. Hence, proportion between the number of pixel pairs on the diagonal and total number of pixels could be a parameter of temperature dependence of the joint histogram. To our knowledge, there is no clear direction to an optimal method. Research on temperature imaging using the joint distribution or joint histogram is an open area.

The maximum likelihood estimator is attractive due to its analytical form and the good performance shown in simulation. A limitation of applying MLE to experimental data is, however, the linearization of random phasor sum (RPS) representation, which introduces bias in the estimation. In Chapter 6, we discussed the calibration and reduction of bias for the same type of scatterer population. If the MLE can be derived

based on higher order approximation of the RPS, estimation bias may be reduced and calibration for removing bias as done in simulation study is no longer needed. An alternative is to change the reference in the experiments. The linearization of RPS is with respect to the reference image. If reference is changed so that relative temperature change is not very large, then the bias caused by linearization can be limited. Furthermore, as mentioned before, the parameters of the MLE based on the generalized Gamma distribution need to be estimated from noisy signals, which requires more study.

Through this dissertation, we assumed that pixels are independent. In the future, we may consider the correlation among pixels. An important tool to incorporate pixel dependence is Markov random field (MRF), which has been used for texture classification [20] and modeling ultrasound envelope images [17, 16]. For example, pixels of envelope-detected images can be modeled as realizations of Nakagami random variables, whose parameters are determined by the pixels in a neighborhood [17, 16]. This concept is similar, in part, to our idea mentioned in Chapter 6, that pixels are realizations of same type of distribution, but with different parameters. If MRFs can be combined into the development of an MLE or a ratio PDF, temperature estimation may be more accurate due to a more precise description of the data statistic properties.

9.4 Dynamic Model

Thermal changes in tissue and thus in backscattered signals during heating are dynamic. Acquiring images at various temperatures is in fact sampling the state of these dynamics. If we can develop a dynamic model to describe the change in signals, it could help link signal properties with temperature.

As in Eq. 7.9, by linearizing the random phasor sum, magnitude of difference images at T_n and T_{n+1} can be approximated by

$$z(\Delta T_n) = \Delta T_n \left| \sum_{k=1}^N \beta'_k(T_0) A_k(T_0) e^{j\phi_k} \right| ,$$

$$z(\Delta T_{n+1}) = \Delta T_{n+1} \left| \sum_{k=1}^N \beta'_k(T_0) A_k(T_0) e^{j\phi_k} \right| .$$

From these two equations, we have

$$z(\Delta T_{n+1}) = \frac{\Delta T_{n+1}}{\Delta T_n} z(\Delta T_n) \quad ,$$

where $\Delta T_n > 0$. The above equation is in fact a simple dynamic model describing the change in signals. The transition parameter is determined by temperature and therefore the system is temperature variant. Estimating temperature could be considered a system identification problem. Although we do not know how much this idea could benefit the study of thermometry for hyperthermia, it is an open area of research. In fact, the above dynamic relation between system states is embedded in the development of the MLE, which was based on the linearization of random phasor sum. Notice that this model has a constraint of $\Delta T_n > 0$, which means the initial state cannot be obtained at T_0 . Correspondingly, a training image was required for estimating the parameter of MLE because image difference at reference temperature provided no information of the change in backscattered signals.

Another possible dynamic model can be considered using the linearized random phasor sum at T_n and T_{n+1}

$$i(T_n) = \sum_{k=1}^N A_k(T_0) e^{j\phi_k} + \Delta T_n \sum_{k=1}^N \beta'_k(T_0) A_k(T_0) e^{j\phi_k} \quad ,$$

$$i(T_{n+1}) = \sum_{k=1}^N A_k(T_0) e^{j\phi_k} + \Delta T_{n+1} \sum_{k=1}^N \beta'_k(T_0) A_k(T_0) e^{j\phi_k} \quad ,$$

where $i(T_0) = \sum_{k=1}^N A_k(T_0) e^{j\phi_k}$. From these equations, we have

$$i(T_{n+1}) = \left(1 - \frac{\Delta T_{n+1}}{\Delta T_{n+1}} \right) i(T_0) + \frac{\Delta T_{n+1}}{\Delta T_{n+1}} i(T_n) \quad .$$

The above equation is another dynamic model to describe thermal changes in signals. Here, there is no constraint that $\Delta T > 0$. However, the statistic property of $i(T_n)$ may be more complicated than that of $z(\Delta T_n)$.

From the above discussion, we see that the form of dynamic model is not unique. For a more practical model, disturbances, such as noise and motion, need to be included. Developing a suitable dynamic model of thermal change in signals for practical application can be a open area of future research. We believe that an accurate estimator for tissue temperature can be derived by combining a suitable dynamic model and a statistic model of the signals.

Appendix A

Matlab Control Functions for the Terason 3000 Ultrasonic Imaging System

A.1 Matlab Control Functions using AutoIt

To start the T3000 GUI and load an exam denoted by "cbe", we used the following AutoIt script, "OpenTerason.au3", which contains the following code:

```
Run("C:\Program Files\Teratech\Terason 3000\Ultrasound.exe") – Starts the Tera-  
son
```

```
WinActivate("Terason t3000 - Probe Data") – Activate T3000 GUI window
```

```
WinWaitActive("Terason t3000 - Probe Data") – Wait T3000 GUI window to be  
active
```

```
Send("!x") – mimic keyboard input "!x"
```

```
Send("O") – mimic keyboard input "O"
```

```
Send("cbe"), Sleep(500), Send("TAB"), Send("ENTER")– load exam "cbe"
```

After each single command, "Sleep" may be executed to ensure the command is finished. AutoIt shared library is loaded by `loadlibrary('AutoItX3')`. Images are saved by calling following functions in Matlab:

```
calllib('AutoItX3','AU3_Send',' ',0); – Send space to freeze image
calllib('AutoItX3','AU3_Sleep', 100);
```

```
calllib('AutoItX3','AU3_Send','F8',0); – Send "F8" to save current frame
calllib('AutoItX3','AU3_WinWaitActive','Terason t3000 - Suspended'," ,0);
calllib('AutoItX3','AU3_Sleep', 50);
```

```
calllib('AutoItX3','AU3_Send',' ',0); – Send space to activate live image
calllib('AutoItX3','AU3_WinWaitActive','Terason t3000 - Probe Data'," ,0);
calllib('AutoItX3','AU3_Sleep', 100);
```

A.2 Matlab Control Functions using the Terason Software Developer's Kit (SDK)

Function StartTerasonActx

```
% Function name: StartTerasonActx
% Descript: This function starts Terason 3000 in Matlab as external
% command. Then, create an ActiveX control for TTAutomation associated
% with the running Terason application. Desired exam will be loaded
% using this control.
% Input: name of exam. e.g. 'cbe'.
% Output: handle of the TTAutomate control.
% Author: Yuzheng Guo
% Date: 1/15/2009
```

```
function hTTauto = StartTerasonActx(exam)
```

```
if (nargin~=1)
    disp('There should be one input');
    exit;
end
```

```

if (~isstr(exam))
    disp('Input should be a sting of exam name');
    exit;
end

% start Terason
% \! C:\\Program Files\\Teratech\\Terason 3000\\Ultrasound.exe \&
system('C:\\Program Files\\Teratech\\Terason 3000\\Ultrasound.exe \&');
pause(15);

% create TTAutomate control
hTTauto = actxcontrol('TTAUTOMATE.TTAutomateCtrl.1');
if (~OpenUltrasound(hTTauto))
    disp('Terason can not be opened!');
    exit;
end

% load exam
if (~LoadPreset(hTTauto,exam))
    disp('Exam can not be loaded!');
    exit;
end

-----

% Author: Yuzheng Guo
% Date: 1/15/2009

function savesglimage\_ttauto(hTTauto,filename)

% freeze image
if(~FreezeImage(hTTauto))

```

```

        disp('Can not freeze image!');
        return;
end

% save image
if(~SaveUltrasoundFile(hTTauto,filename,0))
    disp('Can not save file!');
    return;
end

% Resume live image
if(~ResumeLiveImaging(hTTauto))
    disp('Can not resume live image!');
    return;
end

-----

% Function name: saveloop\_ttauto
% Descript: Save a loop of 2D images using Terason SDK.
% Input: handle of the TTAutomate control. loop filename.
% Author: Yuzheng Guo
% Date: 1/15/2009

function saveloop\_ttauto(hTTauto,filename)

% freeze image
freezed = FreezeImage(hTTauto);
if(~freezed)
    disp('Can not freeze image!');
    return;
end

% save image

```

```
saved = SaveUltrasoundFile(hTTauto,filename,1);
if(~saved)
    disp('Can not save file!');
    return;
end

% Resume live image
if(~ResumeLiveImaging(hTTauto))
    disp('Can not resume live image!');
    return;
end
```

Appendix B

Distribution of the Ratio of Dependent Rayleigh Random Variables

Let y_0 and y_T be two dependent Rayleigh random variables with marginal distributions

$$f(y_0) = \frac{2y_0}{\sigma_1^2} e^{-\frac{y_0^2}{\sigma_1^2}} \quad (\text{B.1})$$

$$f(y_T) = \frac{2y_T}{\sigma_2^2} e^{-\frac{y_T^2}{\sigma_2^2}} \quad (\text{B.2})$$

and joint distribution

$$f(y_0, y_T) = \frac{4y_0y_T}{(1-r^2)\sigma_1^2\sigma_2^2} \exp\left[-\frac{1}{1-r^2}\left(\frac{y_0^2}{\sigma_1^2} + \frac{y_T^2}{\sigma_2^2}\right)\right] I_0\left(\frac{-2ry_0y_T}{(1-r^2)\sigma_1\sigma_2}\right) \quad , \quad (\text{B.3})$$

where $I_0()$ is a modified Bessel function of $0th$ order and r is a correlation parameter with $0 \leq r \leq 1$. We compute the distribution of the ratio, the random variable, z as

$$z = \frac{y_T}{y_0} \quad .$$

The distribution of z , $f_Z(z)$ can be computed using the joint distribution of y_0 and y_T [52]

$$f_Z(z) = \int_{-\infty}^{\infty} |y_0| f_{Y_0 Y_T}(y_0, y_0 z) dy_0 \quad . \quad (\text{B.4})$$

Substituting Eq. B.3 into Eq. B.4 yields

$$\begin{aligned} f_Z(z) &= \int_0^{\infty} y_0 \frac{4y_0 y_T}{(1-r^2)\sigma_1^2 \sigma_2^2} \exp \left[-\frac{1}{1-r^2} \left(\frac{y_0^2}{\sigma_1^2} + \frac{y_T^2}{\sigma_2^2} \right) \right] I_0 \left(\frac{-2r y_0 y_T}{(1-r^2)\sigma_1 \sigma_2} \right) \Big|_{y_T=y_0 z} dy_0 \\ &= \int_0^{\infty} y_0 \frac{4y_0^2 z}{(1-r^2)\sigma_1^2 \sigma_2^2} \exp \left[-\frac{1}{1-r^2} \left(\frac{y_0^2}{\sigma_1^2} + \frac{y_0^2 z^2}{\sigma_2^2} \right) \right] I_0 \left(\frac{-2r y_0^2 z}{(1-r^2)\sigma_1 \sigma_2} \right) dy_0 \quad . \end{aligned} \quad (\text{B.5})$$

Because the modified Bessel function $I_0(u)$ can be written in the form

$$I_0(u) = \sum_{m=0}^{\infty} \frac{u^{2m}}{(m!)^2 4^m} \quad ,$$

$f_Z(z)$ becomes

$$\begin{aligned} f_Z(z) &= \int_0^{\infty} y_0 \frac{4y_0^2 z}{(1-r^2)\sigma_1^2 \sigma_2^2} \exp \left[-\frac{1}{1-r^2} \left(\frac{y_0^2}{\sigma_1^2} + \frac{y_0^2 z^2}{\sigma_2^2} \right) \right] \sum_{m=0}^{\infty} \frac{\left(\frac{-2r y_0^2 z}{(1-r^2)\sigma_1 \sigma_2} \right)^{2m}}{(m!)^2 4^m} dy_0 \\ &= \int_0^{\infty} \frac{4y_0^3 z}{(1-r^2)\sigma_1^2 \sigma_2^2} \exp \left[-\frac{1}{1-r^2} \left(\frac{1}{\sigma_1^2} + \frac{z^2}{\sigma_2^2} \right) y_0^2 \right] \sum_{m=0}^{\infty} \frac{r^{2m} (y_0^2 z)^{2m}}{(m!)^2 (1-r^2)^{2m} (\sigma_1 \sigma_2)^{2m}} dy_0 \\ &= \sum_{m=0}^{\infty} \int_0^{\infty} \frac{4r^{2m} y_0^{4m+3} z^{2m+1}}{(m!)^2 (1-r^2)^{2m+1} (\sigma_1 \sigma_2)^{2m+2}} \exp \left[-\frac{1}{1-r^2} \left(\frac{1}{\sigma_1^2} + \frac{z^2}{\sigma_2^2} \right) y_0^2 \right] dy_0 \quad . \end{aligned} \quad (\text{B.6})$$

Defining

$$\begin{aligned}
\sigma_3^2 &= \left[\frac{1}{1-r^2} \left(\frac{1}{\sigma_1^2} + \frac{z^2}{\sigma_2^2} \right) \right]^{-1} \\
&= \left[\frac{\sigma_2^2 + \sigma_1^2 z^2}{(1-r^2)\sigma_1^2 \sigma_2^2} \right]^{-1} \\
&= \frac{(1-r^2)\sigma_1^2 \sigma_2^2}{\sigma_2^2 + \sigma_1^2 z^2} ,
\end{aligned} \tag{B.7}$$

$f_Z(z)$ now becomes

$$\begin{aligned}
f_Z(z) &= \sum_{m=0}^{\infty} \int_0^{\infty} \frac{4r^{2m} y_0^{4m+3} z^{2m+1}}{(m!)^2 (1-r^2)^{2m+1} (\sigma_1 \sigma_2)^{2m+2}} \exp \left[-\frac{y_0^2}{\sigma_3^2} \right] dy_0 \\
&= \sum_{m=0}^{\infty} \frac{4r^{2m} z^{2m+1}}{(m!)^2 (1-r^2)^{2m+1} (\sigma_1 \sigma_2)^{2m+2}} \int_0^{\infty} y_0^{4m+3} \exp \left[-\frac{y_0^2}{\sigma_3^2} \right] dy_0 \\
&= \sum_{m=0}^{\infty} \frac{2r^{2m} z^{2m+1} \sigma_3^2}{(m!)^2 (1-r^2)^{2m+1} (\sigma_1 \sigma_2)^{2m+2}} \underbrace{\int_0^{\infty} y_0^{4m+2} \frac{2y_0}{\sigma_3^2} \exp \left[-\frac{y_0^2}{\sigma_3^2} \right] dy_0}_{\cdot} .
\end{aligned} \tag{B.8}$$

The kernel of the integral is in fact the $(4m+2)$ th raw moment of a Rayleigh random variable, whose distribution is $\frac{2y_0}{\sigma_3^2} \exp \left[-\frac{y_0^2}{\sigma_3^2} \right]$ with parameter σ_3^2 . For the k th raw moment of a Rayleigh random variable as $\sigma^k \Gamma(1 + \frac{k}{2})$, the integral part can be written as

$$\int_0^{\infty} y_0^{4m+2} \frac{2y_0}{\sigma_3^2} \exp \left[-\frac{y_0^2}{\sigma_3^2} \right] dy_0 = \sigma_3^{4m+2} \Gamma(1 + \frac{4m+2}{2}) = \sigma_3^{4m+2} (2m+1)! .$$

Therefore,

$$f_Z(z) = \sum_{m=0}^{\infty} \frac{2r^{2m} z^{2m+1} \sigma_3^{4m+4} (2m+1)!}{(m!)^2 (1-r^2)^{2m+1} (\sigma_1 \sigma_2)^{2m+2}} . \tag{B.9}$$

Substituting the definition of σ_3^2 into $f_Z(z)$:

$$\begin{aligned}
f_Z(z) &= \sum_{m=0}^{\infty} \frac{2r^{2m} z^{2m+1} (2m+1)!}{(m!)^2 (1-r^2)^{2m+1} (\sigma_1 \sigma_2)^{2m+2}} \left[\frac{(1-r^2) \sigma_1^2 \sigma_2^2}{\sigma_2^2 + \sigma_1^2 z^2} \right]^{2m+2} \\
&= \sum_{m=0}^{\infty} \frac{2r^{2m} (1-r^2) z^{2m+1} (2m+1)! (\sigma_1 \sigma_2)^{2m+2}}{(m!)^2 (\sigma_2^2 + \sigma_1^2 z^2)^{2m+2}} \\
&= \frac{2(1-r^2) \sigma_1^2 \sigma_2^2 z}{(\sigma_2^2 + \sigma_1^2 z^2)^2} \sum_{m=0}^{\infty} \frac{r^{2m} z^{2m} (2m+1)! (\sigma_1^2 \sigma_2^2)^m}{(m!)^2 (\sigma_2^2 + \sigma_1^2 z^2)^{2m}} .
\end{aligned} \tag{B.10}$$

Lemma 1. *The power series in $f_Z(z)$ converges.*

Proof. Define

$$B = \frac{r^2 z^2 \sigma_1^2 \sigma_2^2}{(\sigma_2^2 + \sigma_1^2 z^2)^2}$$

The power series is then

$$A = \sum_{m=0}^{\infty} \frac{(2m+1)!}{(m!)^2} B^m = \sum_{m=0}^{\infty} a_m B^m .$$

The radius of convergence for A can be determined by [51]

$$\lim_{m \rightarrow \infty} \left| \frac{a_m}{a_{m+1}} \right| = \lim_{m \rightarrow \infty} \left| \frac{\frac{(2m+1)!}{(m!)^2}}{\frac{(2(m+1)+1)!}{((m+1)!)^2}} \right| = \lim_{m \rightarrow \infty} \frac{(2m+2)(2m+3)}{(m+1)(m+1)} = \frac{1}{4} .$$

Consider

$$4r^2 z^2 \sigma_1^2 \sigma_2^2 - (\sigma_2^2 + \sigma_1^2 z^2)^2 = (2rz\sigma_1\sigma_2 + \sigma_2^2 + \sigma_1^2 z^2)(2rz\sigma_1\sigma_2 - \sigma_2^2 - \sigma_1^2 z^2)$$

The first part in above equation is larger than zero. The second part can be written as $[-(\sigma_2 - \sigma_1 z)^2 - 2(1-r)z\sigma_1\sigma_2] \leq 0$. Then,

$$4r^2 z^2 \sigma_1^2 \sigma_2^2 - (\sigma_2^2 + \sigma_1^2 z^2)^2 \leq 0 \frac{r^2 z^2 \sigma_1^2 \sigma_2^2}{(\sigma_2^2 + \sigma_1^2 z^2)^2} = B \leq \frac{1}{4} . \tag{B.11}$$

Therefore, B is in the radius of convergence for A and thus A converges. \square

Lemma 2.

$$\sum_{m=0}^{\infty} \frac{(2m+1)!}{(m!)^2} x^m = (1-4x)^{-\frac{3}{2}}$$

Proof.

$$\sum_{m=0}^{\infty} \frac{(2m+1)!}{(m!)^2} x^m = \sum_{m=0}^{\infty} \frac{(2m)!(2m+1)}{(m!)^2} (\sqrt{x})^{2m}$$

Let $y = \sqrt{x}$, then

$$\begin{aligned} \sum_{m=0}^{\infty} \frac{(2m+1)!}{(m!)^2} x^m &= \sum_{m=0}^{\infty} \frac{(2m)!(2m+1)}{(m!)^2} y^{2m} \\ &= \sum_{m=0}^{\infty} \frac{(2m)!}{(m!)^2} \frac{dy^{2m+1}}{dy} \\ &= \frac{d}{dy} \left[\sum_{m=0}^{\infty} \frac{(2m)!}{(m!)^2} y^{2m+1} \right] \\ &= \frac{d}{dy} \left[y \sum_{m=0}^{\infty} \frac{(2m)!}{(m!)^2} (y^2)^m \right] \end{aligned} \tag{B.12}$$

From the power series expansion we have

$$\frac{1}{\sqrt{1-4z}} = \sum_{m=0}^{\infty} \binom{2m}{m} z^m = \sum_{m=0}^{\infty} \frac{2m!}{(m!)^2} z^m .$$

Thus,

$$\begin{aligned} \sum_{m=0}^{\infty} \frac{(2m+1)!}{(m!)^2} x^m &= \frac{d}{dy} \left[\frac{y}{\sqrt{1-4y^2}} \right] \\ &= (1-4y^2)^{-\frac{3}{2}} \\ &= (1-4x)^{-\frac{3}{2}} \end{aligned} \tag{B.13}$$

□

From Lemma 2, the closed form of the power series in $f_Z(z)$ is $(1-4B)^{-\frac{3}{2}}$. Therefore,

$$\begin{aligned}
f_Z(z) &= \frac{2(1-r^2)\sigma_1^2\sigma_2^2z}{(\sigma_2^2 + \sigma_1^2z^2)^2} [1-4B]^{-\frac{3}{2}} \\
&= \frac{2(1-r^2)\sigma_1^2\sigma_2^2z}{(\sigma_2^2 + \sigma_1^2z^2)^2} \left[1 - 4 \frac{r^2z^2\sigma_1^2\sigma_2^2}{(\sigma_2^2 + \sigma_1^2z^2)^2} \right]^{-\frac{3}{2}} \\
&= \frac{2(1-r^2)\sigma_1^2\sigma_2^2z}{(\sigma_2^2 + \sigma_1^2z^2)^2} \frac{(\sigma_2^2 + \sigma_1^2z^2)^3}{[(\sigma_2^2 + \sigma_1^2z^2)^2 - 4r^2\sigma_1^2\sigma_2^2z^2]^{-\frac{3}{2}}} .
\end{aligned} \tag{B.14}$$

Finally,

$$f_Z(z) = \frac{2(1-r^2)\sigma_1^2\sigma_2^2(\sigma_2^2 + \sigma_1^2z^2)z}{[(\sigma_2^2 + \sigma_1^2z^2)^2 - 4r^2\sigma_1^2\sigma_2^2z^2]^{-\frac{3}{2}}} . \tag{B.15}$$

Note that, distributions of y_0 and y_T can be written

$$\begin{aligned}
f(y_0) &= \frac{y_0}{\sigma_0^2} e^{-\frac{y_0^2}{2\sigma_0^2}} \\
f(y_T) &= \frac{y_T}{\sigma^2} e^{-\frac{y_T^2}{2\sigma^2}} ,
\end{aligned}$$

where $\sigma_0^2 = 0.5\sigma_1^2$, $\sigma^2 = 0.5\sigma_2^2$, and σ_1^2 and σ_2^2 are the same as above. Then, the joint distribution becomes

$$f(y_0, y_T) = \frac{y_0y_T}{(1-r^2)\sigma_0^2\sigma^2} \exp \left[-\frac{1}{2(1-r^2)} \left(\frac{y_0^2}{\sigma_0^2} + \frac{y_T^2}{\sigma^2} \right) \right] I_0 \left(\frac{-ry_0y_T}{(1-r^2)\sigma_0\sigma} \right) . \tag{B.16}$$

However, if substitute $\sigma_0^2 = 0.5\sigma_1^2$, $\sigma^2 = 0.5\sigma_2^2$, for example, into Eq. B.15, the result does not change. That is, the form of ratio distribution does not change with the form of the marginal distributions of the denominator and numerator.

Appendix C

Estimation of Correlation Parameter in the Joint Rayleigh Distribution

Let y_0 and y_T be two dependent Rayleigh random variables representing ultrasound B-scans. Their marginal distributions are

$$f(y_0) = \frac{y_0}{\sigma_0^2} e^{-\frac{y_0^2}{2\sigma_0^2}}$$
$$f(y_T) = \frac{y_T}{\sigma^2} e^{-\frac{y_T^2}{2\sigma^2}} \quad ,$$

and their joint distribution is

$$f(y_0, y_T) = \frac{y_0 y_T}{(1-r^2)\sigma_1^2 \sigma_2^2} \exp \left[-\frac{1}{2(1-r^2)} \left(\frac{y_0^2}{\sigma_1^2} + \frac{y_T^2}{\sigma_2^2} \right) \right] I_0 \left(\frac{-r y_0 y_T}{(1-r^2)\sigma_1 \sigma_2} \right) \quad , \quad (\text{C.1})$$

where $I_0(\cdot)$ is a modified Bessel function of 0th order and r is a correlation parameter with $0 \leq r \leq 1$. r can be estimated as [91, 13]

$$\hat{r} = \sqrt{\frac{\text{Cov}(y_0^2, y_T^2)}{\sqrt{\text{Var}(y_0^2) \text{Var}(y_T^2)}}}$$

In reality, r needs to be estimated from noisy signals. Let \tilde{y}_0 and \tilde{y}_T denote noisy versions of y_0 and y_T , respectively. Noise is assumed to be additive Gaussian noise in the corresponding RF signals, x_0 and x_T . Let $n_0 \sim N(0, \sigma_{n_0}^2)$ and $n_T \sim N(0, \sigma_{n_T}^2)$ be

the noise in x_0 and x_T , respectively. The distributions of \widetilde{y}_0 and \widetilde{y}_T are then

$$f(\widetilde{y}_0) = \frac{y_0}{\widetilde{\sigma}_0^2} e^{-\frac{y_0^2}{2\widetilde{\sigma}_0^2}}$$

$$f(\widetilde{y}_T) = \frac{y_T}{\widetilde{\sigma}^2} e^{-\frac{y_T^2}{2\widetilde{\sigma}^2}} \quad ,$$

where $\widetilde{\sigma}_0^2 = \sigma_0^2 + \sigma_{n_0}^2$ and $\widetilde{\sigma}^2 = \sigma^2 + \sigma_{n_T}^2$.

Below, we compute some useful raw moments of y_0 , y_T , \widetilde{y}_0 and \widetilde{y}_T . For a Rayleigh random variable with distribution $f(z) = \frac{z}{\sigma^2} e^{-\frac{z^2}{2\sigma^2}}$, the k th raw moment is $\mu_k = \sigma^k 2^{k/2} \Gamma(1 + k/2)$. Therefore, we have

$$E(y_0^2) = \sigma_0^2 2^{2/2} \Gamma(1 + 2/2) = 2\sigma_0^2 \quad (\text{C.2})$$

$$E(y_0^4) = \sigma_0^4 2^{4/2} \Gamma(1 + 4/2) = 8\sigma_0^4 \quad (\text{C.3})$$

$$E(y_T^2) = \sigma^2 2^{2/2} \Gamma(1 + 2/2) = 2\sigma^2 \quad (\text{C.4})$$

$$E(y_T^4) = \sigma^4 2^{4/2} \Gamma(1 + 4/2) = 8\sigma^4 \quad (\text{C.5})$$

$$E(\widetilde{y}_0^2) = \widetilde{\sigma}_0^2 2^{2/2} \Gamma(1 + 2/2) = 2\widetilde{\sigma}_0^2 \quad (\text{C.6})$$

$$E(\widetilde{y}_0^4) = \widetilde{\sigma}_0^4 2^{4/2} \Gamma(1 + 4/2) = 8\widetilde{\sigma}_0^4 \quad (\text{C.7})$$

$$E(\widetilde{y}_T^2) = \widetilde{\sigma}^2 2^{2/2} \Gamma(1 + 2/2) = 2\widetilde{\sigma}^2 \quad (\text{C.8})$$

$$E(\widetilde{y}_T^4) = \widetilde{\sigma}^4 2^{4/2} \Gamma(1 + 4/2) = 8\widetilde{\sigma}^4 \quad (\text{C.9})$$

Now, we compute the variance of y_0^2 and y_T^2 .

$$\begin{aligned} \text{Var}(\widetilde{y}_0^2) &= E(\widetilde{y}_0^4) - E^2(\widetilde{y}_0^2) = 8\widetilde{\sigma}_0^4 - (2\widetilde{\sigma}_0^2)^2 \\ &= 4\widetilde{\sigma}_0^4 = 4(\sigma_0^2 + \sigma_{n_0}^2)^2 = 4\sigma_0^4 + 8\sigma_0^2\sigma_{n_0}^2 + 4\sigma_{n_0}^4 \quad (\text{C.10}) \\ &= \text{Var}(y_0^2) + 8\sigma_0^2\sigma_{n_0}^2 + 4\sigma_{n_0}^4 \quad . \end{aligned}$$

Therefore,

$$\text{Var}(y_0^2) = \text{Var}(\widetilde{y}_0^2) - 8\sigma_0^2\sigma_{n_0}^2 - 4\sigma_{n_0}^4 \quad . \quad (\text{C.11})$$

Similarly,

$$\text{Var}(y_T^2) = \text{Var}(\widetilde{y}_T^2) - 8\sigma^2\sigma_{n_T}^2 - 4\sigma_{n_T}^4 \quad . \quad (\text{C.12})$$

Now, we prove that

$$\text{Cov}(y_0^2 y_T^2) = \text{Cov}(\tilde{y}_0^2 \tilde{y}_T^2) \quad .$$

$\text{Cov}(\tilde{y}_0^2 \tilde{y}_T^2)$ can be estimated from \tilde{y}_0^2 and \tilde{y}_T^2

$$\text{Cov}(\tilde{y}_0^2 \tilde{y}_T^2) = E(\tilde{y}_0^2 \tilde{y}_T^2) - E(\tilde{y}_0^2)E(\tilde{y}_T^2) \quad . \quad (\text{C.13})$$

We first write y_0^2 and y_T^2 in the form of the square magnitude of the random phasor sum as in Eq. 6.10

$$\begin{aligned} y_0^2 &= R_0^2 + I_0^2 \quad , \\ y_T^2 &= R^2 + I^2 \quad , \end{aligned}$$

where $R_0 \perp I_0$, $R \perp I$, $R_0, I_0 \sim N(0, \sigma_0^2)$ and $R, I \sim N(0, \sigma^2)$. The corresponding representations for \tilde{y}_0 and \tilde{y}_T are

$$\begin{aligned} \tilde{y}_0^2 &= (R_0 + n_1)^2 + (I_0 + n_2)^2 \quad , \\ \tilde{y}_T^2 &= (R + n_3)^2 + (I + n_4)^2 \quad , \end{aligned}$$

where R_0 , I_0 , R and I are the same as above. $n_i, i = 1, 2, 3, 4$ are noise in random phasor sums corresponding to the noise in the RF signals and $n_1, n_2 \sim N(0, \sigma_{n_0}^2)$ and $n_3, n_4 \sim N(0, \sigma_{n_T}^2)$. $n_i, i = 1, 2, 3, 4$ are independent of the signals and each other. Then,

$$\begin{aligned} E(\tilde{y}_0^2 \tilde{y}_T^2) &= E \left[((R_0 + n_1)^2 + (I_0 + n_2)^2) ((R + n_3)^2 + (I + n_4)^2) \right] \\ &= E \left[(R_0^2 + 2R_0 n_1 + n_1^2 + I_0^2 + 2I_0 n_2 + n_2^2) (R^2 + 2R n_3 + n_3^2 + I^2 + 2I n_4 + n_4^2) \right] \\ &= E \left[R_0^2 R^2 + 2R_0^2 R n_3 + R_0^2 n_3^2 + R_0^2 I^2 + 2R_0^2 I n_4 + R_0^2 n_4^2 + \right. \\ &\quad 2R_0 n_1 R^2 + 4R_0 n_1 R n_3 + 2R_0 n_1 n_3^2 + 2R_0 n_1 I^2 + 4R_0 n_1 I n_4 + 2R_0 n_1 n_4^2 + \\ &\quad R^2 n_1^2 + 2R n_3 n_1^2 + n_3^2 n_1^2 + I^2 n_1^2 + 2I n_4 n_1^2 + n_4^2 n_1^2 + \\ &\quad I_0^2 R^2 + 2I_0^2 R n_3 + I_0^2 n_3^2 + I_0^2 I^2 + 2I_0^2 I n_4 + I_0^2 n_4^2 + \\ &\quad 2I_0 n_2 R^2 + 4I_0 n_2 R n_3 + 2I_0 n_2 n_3^2 + 2I^2 I_0 n_2 + 4I_0 n_2 I n_4 + 2I_0 n_2 n_4^2 + \\ &\quad \left. R^2 n_2^2 + 2R n_3 n_2^2 + n_3^2 n_2^2 + I^2 n_2^2 + 2I n_4 n_2^2 + n_4^2 n_2^2 \right] \end{aligned} \quad (\text{C.14})$$

Notice that because $E(R_0^2) = E(I_0^2) = \sigma_0^2$, $E(R^2) = E(I^2) = \sigma^2$, $E(n_i) = 0, i = 1, 2, 3, 4$, $E(n_1^2) = E(n_2^2) = \sigma_{n_0}^2$ and $E(n_3^2) = E(n_4^2) = \sigma_{n_T}^2$, the above equation becomes

$$\begin{aligned}
E(\tilde{y}_0^2 \tilde{y}_T^2) &= E(R_0^2 R^2) + 0 + \sigma_0^2 \sigma_{n_T}^2 + E(R_0^2 I^2) + 0 + \sigma_0^2 \sigma_{n_T}^2 + \\
&\quad 0 + 0 + 0 + 0 + 0 + 0 + \\
&\quad \sigma^2 \sigma_{n_0}^2 + 0 + \sigma_{n_0}^2 \sigma_{n_T}^2 + \sigma^2 \sigma_{n_0}^2 + 0 + \sigma_{n_0}^2 \sigma_{n_T}^2 + \\
&\quad E(I_0^2 R^2) + 0 + \sigma_0^2 \sigma_{n_T}^2 + E(I_0^2 I^2) + 0 + \sigma_0^2 \sigma_{n_T}^2 + \\
&\quad 0 + 0 + 0 + 0 + 0 + 0 + \\
&\quad \sigma^2 \sigma_{n_0}^2 + 0 + \sigma_{n_0}^2 \sigma_{n_T}^2 + \sigma^2 \sigma_{n_0}^2 + 0 + \sigma_{n_0}^2 \sigma_{n_T}^2 \\
&= E(R_0^2 R^2 + R_0^2 I^2 + I_0^2 R^2 + I_0^2 I^2) + 4(\sigma_0^2 \sigma_{n_T}^2 + \sigma^2 \sigma_{n_0}^2 + \sigma_{n_0}^2 \sigma_{n_T}^2) \\
&= E[(R_0^2 + I_0^2)(R + I)] + 4(\sigma_0^2 \sigma_{n_T}^2 + \sigma^2 \sigma_{n_0}^2 + \sigma_{n_0}^2 \sigma_{n_T}^2) \\
&= E[y_0^2 y_T^2] + 4(\sigma_0^2 \sigma_{n_T}^2 + \sigma^2 \sigma_{n_0}^2 + \sigma_{n_0}^2 \sigma_{n_T}^2) \quad .
\end{aligned} \tag{C.15}$$

To compute $E(\tilde{y}_0^2)E(\tilde{y}_T^2)$, we use

$$\begin{aligned}
E(\tilde{y}_0^2)E(\tilde{y}_T^2) &= (2\tilde{\sigma}_0^2)(2\tilde{\sigma}^2) \\
&= 4(\sigma_0^2 + \sigma_{n_0}^2)(\sigma^2 + \sigma_{n_T}^2) \\
&= 4\sigma_0^2 \sigma^2 + 4(\sigma_0^2 \sigma_{n_T}^2 + \sigma_{n_0}^2 \sigma^2 + \sigma_{n_0}^2 \sigma_{n_T}^2) \\
&= E(y_0^2)E(y_T^2) + 4(\sigma_0^2 \sigma_{n_T}^2 + \sigma_{n_0}^2 \sigma^2 + \sigma_{n_0}^2 \sigma_{n_T}^2) \quad .
\end{aligned} \tag{C.16}$$

Substituting this result into Eq. C.13:

$$\begin{aligned}
Cov(\tilde{y}_0^2 \tilde{y}_T^2) &= E(\tilde{y}_0^2 \tilde{y}_T^2) - E(\tilde{y}_0^2)E(\tilde{y}_T^2) \\
&= E[y_0^2 y_T^2] + 4(\sigma_0^2 \sigma_{n_T}^2 + \sigma^2 \sigma_{n_0}^2 + \sigma_{n_0}^2 \sigma_{n_T}^2) - (E(y_0^2)E(y_T^2) + \\
&\quad 4(\sigma_0^2 \sigma_{n_T}^2 + \sigma_{n_0}^2 \sigma^2 + \sigma_{n_0}^2 \sigma_{n_T}^2)) \\
&= E[y_0^2 y_T^2] - E(y_0^2)E(y_T^2) \\
&= Cov(y_0^2 y_T^2) \quad .
\end{aligned} \tag{C.17}$$

Eqs.C.11, C.12 and C.17 give estimates of the correlation parameter, r , in the joint Rayleigh distribution.

Appendix D

Dependence of the Ratio PDF on SNR

In the discussion below, we show, analytically, how the ratio PDF depends on SNR when the change in signals is caused only by noise. Scatterers are assumed to be uniformly distributed. Suppose s_1 and s_2 are two RF images of the same tissue sample with noise:

$$s_1 = i_{rf} + n_1 \quad , \quad (D.1)$$

$$s_2 = i_{rf} + n_2 \quad , \quad (D.2)$$

where $i_{rf} \sim N(0, \sigma_r^2)$, $n_1, n_2 \sim N(0, \sigma_n^2)$, $i_{rf} \perp n_1, n_2$ and $n_1 \perp n_2$. Therefore, s_1 and s_2 are dependent identically distributed random variables, with $s_1, s_2 \sim N(0, \sigma_s^2)$ and $\sigma_s^2 = \sigma_r^2 + \sigma_n^2$.

Denote the envelope detected images corresponding to s_1, s_2 by y_1 and y_2 respectively. Because scatterers are uniformly distributed, y_1 and y_2 are Rayleigh random variables with parameter σ_s^2 . As discussed in the framework (Chapter 6), the ratio computation is modeled as

$$z = \frac{y_2}{y_1} \quad ,$$

where y_1 and y_2 are Rayleigh variables with parameters $\sigma_{y1}^2 = \sigma_{y2}^2 = \sigma_y^2 = \sigma_s^2$. Distribution of z can be determined using Eq.6.24 by setting $\sigma^2 = \sigma_0^2 = \sigma_y^2$:

$$f_Z(z) = \frac{2(1-r^2)(1+z^2)z}{[(1+z^2)^2 - 4r^2z^2]^{\frac{3}{2}}} \quad (D.3)$$

From Eq.B.3 and 6.25, it can be proved that

$$\begin{aligned} r^2 &= \frac{4\sigma_r^4}{4(\sigma_r^2 + \sigma_n^2)} \\ &= \frac{\frac{\sigma_r^4}{\sigma_n^4}}{\frac{\sigma_r^4}{\sigma_n^4} + 2\frac{\sigma_r^2}{\sigma_n^2} + 1} \end{aligned} \quad (\text{D.4})$$

Note that the ratio $\frac{\sigma_r^2}{\sigma_n^2}$ is in fact a representation of signal-to-noise ratio. Denoting it by μ , we have

$$r^2 = \left(\frac{\mu}{\mu + 1} \right)^2. \quad (\text{D.5})$$

Therefore, distribution of the ratio z becomes

$$f_Z(z) = \frac{2 \left(1 - \left(\frac{\mu}{\mu+1} \right)^2 \right) (1 + z^2) z}{\left[(1 + z^2)^2 - 4 \left(\frac{\mu}{\mu+1} \right)^2 z^2 \right]^{\frac{3}{2}}}. \quad (\text{D.6})$$

More generally, suppose the noise in s_1 and s_2 is at different levels, i.e., $n_1 \sim N(0, \sigma_{n1}^2)$ and $n_2 \sim N(0, \sigma_{n2}^2)$, $\sigma_{n1}^2 \neq \sigma_{n2}^2$. The Rayleigh parameters of y_1 and y_2 then become $\sigma_{y1}^2 = \sigma_r^2 + \sigma_{n1}^2$ and $\sigma_{y2}^2 = \sigma_r^2 + \sigma_{n2}^2$. The distribution of z is then

$$f_Z(z) = \frac{2(1 - r^2)\sigma_{y1}^2\sigma_{y2}^2(\sigma_{y2}^2 + \sigma_{y1}^2 z^2)z}{\left[(\sigma_{y2}^2 + \sigma_{y1}^2 z^2)^2 - 4r^2 z^2 \sigma_{y1}^2 \sigma_{y2}^2 \right]^{\frac{3}{2}}}, \quad (\text{D.7})$$

where

$$r^2 = \frac{\mu_1 \mu_2}{(\mu_1 + 1)(\mu_2 + 1)}$$

and $\mu_1 = \frac{\sigma_r^2}{\sigma_{n1}^2}$ and $\mu_2 = \frac{\sigma_r^2}{\sigma_{n2}^2}$. $f_Z(z)$ can be further modified

$$f_Z(z) = \frac{2 \frac{(\mu_1+1)(\mu_2+1)}{\mu_1 \mu_2} \left(1 - \frac{\mu_1 \mu_2}{(\mu_1+1)(\mu_2+1)} \right) \left(\frac{\mu_2+1}{\mu_2} + \frac{\mu_1+1}{\mu_1} z^2 \right) z}{\left[\left(\frac{\mu_2+1}{\mu_2} + \frac{\mu_1+1}{\mu_1} z^2 \right)^2 - 4z^2 \right]^{\frac{3}{2}}}, \quad (\text{D.8})$$

where μ_1 and μ_2 represent signal-to-noise ratio of s_1 and s_2 , respectively. When $\mu_1 = \mu_2 = \mu$, Eq. D.8 reduces to Eq. D.6.

Eqs. D.6 and D.8 show that, when there is no change in backscattered signals, the distribution of ratio z between two noise corrupted signals depends only on SNR in original RF images. Therefore, PCBE and NCBE are functions of the signal-to-noise ratio since z disappears after integration. When SNR is very low, $r = \frac{\mu}{\mu+1}$ is less than 1, y_1 and y_2 are less correlated. CBE will be determined by μ . When SNR is very high, $r = \frac{\mu}{\mu+1}$ is close to 1 and $f_Z(z)$ is close to zero, indicating y_1 and y_2 are highly correlated. Because the backscattered signals are assumed to be same, CBE without noise is $0dB$, as expected.

Appendix E

CBE Due to Motion-Induced De-correlation

When CBE is computed from two images with a rigid motion-induced shift, we can assume the two RF images are in form of

$$s_1 = i_{rf1} + n_1 \quad , \quad (\text{E.1})$$

$$s_2 = i_{rf2} + n_2 \quad , \quad (\text{E.2})$$

where $i_{rf1}, i_{rf2} \sim N(0, \sigma^2)$, $n_1, n_2 \sim N(0, \sigma_n^2)$ assuming uniformly distributed scatterers. Therefore, the corresponding envelope detected signals, y_1 and y_2 are Rayleigh with same parameter $\sigma_{y1} = \sigma_{y2} = \sigma_y$. The ratio distribution is the same as in Eq. D.3, from which we see that CBE is a function of the correlation parameter r^2 only. Fig. 3.11 shows the prediction of CBE variation with r^2 using Eq. D.3 and the definitions of PCBE and NCBE in Eq. 6.18 and 6.19, respectively. Notice that, r^2 here depends on both SNR and motion and does not follow Eq. D.4 any more, because Eq. D.4 is valid only when $i_{rf1} = i_{rf2}$, which is not satisfied due to the motion.

When motion is large enough such that the two signals are completely uncorrelated, PCBE and NCBE can be computed using Eq. 6.22 with $\sigma = \sigma_0$:

$$PCBE = \frac{\frac{\sigma^2}{\sigma_0^2 + \sigma^2} + \frac{\sigma}{\sigma_0} [\frac{\pi}{2} - \arctan(\frac{\sigma_0}{\sigma})]}{\frac{\sigma^2}{\sigma_0^2 + \sigma^2}} \quad , \quad (E.3)$$

$$NCBE = \frac{\frac{\sigma}{\sigma_0} \arctan(\frac{\sigma_0}{\sigma}) - \frac{\sigma^2}{\sigma_0^2 + \sigma^2}}{\frac{\sigma_0^2}{\sigma_0^2 + \sigma^2}} \quad . \quad (E.4)$$

The resulting PCBE and NCBE values for large motion, i.e., with $\sigma = \sigma_0$ are

$$PCBE = 1 + \frac{\pi}{2} \text{ or } 8.2\text{dB}$$

$$NCBE = \frac{\pi}{2} - 1 \text{ or } -4.87\text{dB}.$$

These values match the simulations in Fig. 3.10 and the prediction in Fig. 3.11.

References

- [1] AN Amini, ES Ebbini, and TT Georgiou. Noninvasive estimation of tissue temperature via high-resolution spectral analysis techniques. *Biomed. Eng., IEEE Transactions on*, 52(2):221 – 228, 2005.
- [2] A Anand, D Savery, and C Hall. Three-dimensional spatial and temporal temperature imaging in gel phantoms using backscattered ultrasound. *UFFC, IEEE Trans on*, 54(1):23–31, 2007.
- [3] RM Arthur, WL Straube, JD Starman, and EG Moros. Noninvasive temperature estimation based on the energy of backscattered ultrasound. *Medical Physics*, 30:1021–1029, 2003.
- [4] RM Arthur, WL Straube, JW Trobaugh, and EG Moros. Non-invasive estimation of hyperthermia temperatures with ultrasound. *Int. J. Hyperthermia*, 21(6):589–600, 2005.
- [5] RM Arthur, WL Straube, JW Trobaugh, J Parry, Y Guo, and EG Moros. In vivo change in ultrasonic backscattered energy with temperature in motion-compensated images(abtract). *J of Ultrtrasound in Med*, 25:S75, 2006.
- [6] RM Arthur, JW Trobaugh, Y Guo, WL Straube, and EG Moros. Change in ultrasonic backscattered energy for temperature imaging: Factors affecting temperature accuracy and spatial resolution(abtract). *Ultrasound Imaging*, 29:47–48, 2007.
- [7] RM Arthur, JW Trobaugh, WL Straube, and EG Moros. Temperature dependence of ultrasonic backscattered energy in motion-compensated images. *Ultrasonics, Ferroelectrics and Frequency Control, IEEE Transactions on*, 52(10):1644–1652, 2005.
- [8] RM Arthur, JW Trobaugh, WL Straube, J Parry, Y Guo, and EG Moros. Change in ultrasonic backscattered energy for temperature imaging: Factors affecting temperature accuracy and spatial resolution(abtract). *Ultrasound Imaging*, 28:4–5, 2006.
- [9] JC Bamber and CR Hill. Ultrasonic attenuation and propagation speed in mammalian tissues as a function of temperature. *Ultrasound in Med & Biol*, 5(2):149–157, 1979.

- [10] P Beckmann and A Spizzichino. *The scattering of electromagnetic waves from rough surfaces*. The MacMillan Company,, New York, 1963.
- [11] ZE Begui. Acoustic properties of the refractive media of the eye. *J Acoust Soc Am*, 26:365–368, 1954.
- [12] J Bercoff, M Tanter, L Sandrin, S Catheline, and M Fink. Ultrafast compound imaging for 2d displacement vector measurements: application to transient elastography and color flow mapping. *Ultrasonics Symposium, IEEE*, 2:1619–1622, 2001.
- [13] PS Bithas, NC Sagias, TA Tsiftsis, and GK Karagiannidis. Products and ratios of two gaussian class correlated weibull random variables. In *the 12th International conference on applied stochastic models and data analysis (ASMDA)*, May 2007.
- [14] PS Bithas and TA Tsiftsis. Statistics of correlated generalized gamma variates. In *the 12th International conference on applied stochastic models and data analysis (ASMDA)*, May 2007.
- [15] LN Bohs and GE Trahey. A novel method for angle independent ultrasonic imaging of blood flow and tissue motion. *Biomed Eng, IEEE Trans on*, 38(3):280–286, 1991.
- [16] N Bouhlef, S Sevestre-Ghalila, and C Graffigne. Markov random field model based on nakagami distribution for modeling ultrasound rf envelope. In *14th European Signal Processing Conference, 2006*, pages II–1124 – II–1127, France, September 2006.
- [17] N Bouhlef, S Sevestre-Ghalila, M Jaidane, and C Graffigne. Ultrasound backscatter characterization by using markov random field model. In *IEEE International Conference on Accoustic, Speech and Signal Processing. ICASSP 2006*, volume 2, pages II–1124 – II–1127, May 2006.
- [18] T Bowen, WG Connor, RL Nasoni, AE Pifer, and RR Sholes. Measurement of the temperature dependence of the velocity. In *Ultrasonic Tissue Characterization II, M Linzer, Ed, National Bureau of Standards*, volume Spec Publ 525, pages 57–61. US Government Printing Office, Washington D.C., 1979.
- [19] DL Carter, JR MacFall, ST Clegg, X Wan, DM Prescott, HC Charles, and TV Samulski. Magnetic resonance thermometry during hyperthermia for human high-grade sarcoma. *Int J Radiat Oncol Biol Phys*, 40:815–822, 1998.
- [20] R Chellappa and S Chatterjee. Classification of textures using gaussian markov random field. *Acoustics, speech and signal processing, IEEE Trans. on*, ASSP-33(4):959–963, Aug. 1985.

- [21] X Chen, MJ Zohdy, SY Emelianov, and M O'Donnell. Lateral speckle tracking using synthetic lateral phase. *UFFC, IEEE Trans on*, 51(5):540–550, 2004.
- [22] HK Chiang, CK Liao, YH Chou, TT Pan, and SC Pan. In-vitro ultrasound temperature monitoring in bovine liver during rf ablation therapy using auto-correlation. *Ultrasonics Symposium, IEEE*, 2:1439–1442, 2002.
- [23] RL Clarke, NL Bush, and GR Ter Haar. The changes in acoustic attenuation due to in vitro heating. *Ultrasound in Med & Biol*, 29(1):127–135, 2003.
- [24] TM Cover and JA Thomas. *Elements of Information Theory*. John Wiley Sons, Inc, 1991.
- [25] CA Damianou, NT Sanghvi, FJ Fry, and R Maass-Moreno. Dependence of ultrasonic attenuation and absorption in dog soft tissues on temperature and thermal dose. *J Acoust Soc Am*, 102(10):628–634, 1997.
- [26] DATAQ Instruments, 241 Springside Drive, Akron, Ohio 44333, USA. *DI-1000TC User's Manual*, manual revision h, software release level 1 edition.
- [27] BD de Senneville, P Desbarats, R Salomir, B Quesson, and CTW Moonen. Correction of accidental patient motion for online mr thermometry. In C Barillot, DR Haynor, and P Hellier, editors, *7th International conference on medical image computing and computer assisted intervention. MICCAI 2004*, volume 3217, pages 637–644, Saint Malo, France, September 2004.
- [28] BD de Senneville, B Quesson, and CTW Moonen. Magnetic resonance temperature imaging. *Int. J. Hyperthermia*, 21(6):515–531, 2005.
- [29] V Dutt and JF Greenleaf. Ultrasound echo envelope analysis using homodyned k distribution signal model. *Ultrasound Imaging*, 16:265–287, 1994.
- [30] ES Ebbini. Phase-coupled two-dimensional speckle tracking algorithm. *UFFC, IEEE Trans on*, 53(5):972–990, 2006.
- [31] Tobjørn Eltoft. The rician inverse gaussian distribution: A new model for non-rayleigh signal amplitude statistics. *Image Processing, IEEE Trans on*, 14(11):1722–1735, 2005.
- [32] Tobjørn Eltoft. Modeling the amplitude statistics of ultrasonic images. *Med. Imag., IEEE Trans on*, 25(2):229–240, 2006.
- [33] PM Embree and WD O'Brien Jr. Volumetric blood flow via time-domain correlation: experimental verification. *UFFC, IEEE Trans on*, 37(2):176–189, 1990.
- [34] PM Embree and WD O'Brien. The accurate ultrasonic measurement of the volume flow of blood by time domain correlation. *UFFC, IEEE Trans on*, 53(11):2026–2035, 2006.

- [35] KW Ferrara and VR Algazi. A new wideband spread target maximum likelihood estimator for blood velocity estimation-part i: theory. *UFFC, IEEE Trans on*, 38(1):1–16, 1991.
- [36] SG Forster, PM Embree, and WD O’Brien. Flow velocity profile via time-domain correlation: Error analysis and computer simulation. *UFFC, IEEE Trans on*, 37(2):164–175, 1990.
- [37] SA Goss, RL Johnston, and F Dunn. Comprehensive compilation of empirical ultrasonic properties of mammalian tissues. *J Acoust Soc Am*, 64(2):423–457, 1978.
- [38] S. Haykin. *Communication Systems*. John Wiley & Sons, Inc, 1994.
- [39] IA Hein, JT Chen, WK Jenkins, and WD O’Brien Jr. A real-time ultrasound time-domain correlation blood flowmeter: Part i - theory and design. *UFFC, IEEE Trans on*, 40(6):768–775, 1993.
- [40] IA Hein and WD O’Brien Jr. A real-time ultrasound time-domain correlation blood flowmeter: Part ii - performance and experimental verification. *UFFC, IEEE Trans on*, 40(6):776–785, 1993.
- [41] IA Hein and WD O’Brien. Current time-domain methods for assessing tissue motion by analysis from reflected ultrasound echoes. *UFFC, IEEE Trans on*, 40(2):84–102, 1993.
- [42] M Hentschel, W Dreher, P Wust, S Röhl, D Leibfritz, and R Felix. Fast spectroscopic imaging for non-invasive thermometry using the pr[moe-do3a] complex. *Phys Med Biol*, 44:2397–2408, 1999.
- [43] K Hynynen, A Chung, T Fjield, M Buchanan, D Daum, V Colucci, P Lopath, and F Jolesz. Feasibility of using ultrasound phased arrays for mri monitored noninvasive surgery. *UFFC, Transactions on*, 43(6):1043–1053, 1996.
- [44] de Zwart JA, FC Vimeux, J Palussière, R Salomir, B Quesson, C Delalande, and CTW Moonen. On-line correction and visualization of motion during mri-controlled hyperthermia. *Magnetic Resonance in Medicine*, 45:128–137, 2001.
- [45] E Jakeman and RJA Tough. Generalized k distribution: a statistical model for weak scattering. *J. Opt. Soc. Am. A*, 4(9):1764–1772, 1987.
- [46] SA Johnson, DA Christensen, CC Johnson, JF Greenleaf, and B Rajagopalan. Non-intrusive measurement of microwave and ultrasound-induced hyperthermia by acoustic temperature tomography. *Proceedings of IEEE Symposium on Ultrasonics*, 77Ch1264-1SU:977–982, 1977.

- [47] PJ Kaczkowski and A Anand. Temperature rise measured noninvasively during thermal therapy using backscattered ultrasound. *Ultrasonics Symposium, IEEE*, 1:720–723, 2004.
- [48] C Kasai, K Namekawa, A Koyano, and R Omoto. Real-time two-dimensional blood flow imaging using an autocorrelation technique. *Sonics and Ultrasonics, IEEE Trans on*, SU-32:458–464, 1985.
- [49] S Kotz, TJ Kozubowski, and K Podgorski. *The Laplace distribution and generalizations: a revisit with applications to communications, economics, engineering and finance*. Birkhauser Boston, 1 edition, May 2001.
- [50] S Kotz, TJ Kozubowski, and K Podgorski. *Medical image processing, reconstruction and restoration: concepts and methods*. Birkhauser Boston, 1 edition, Nov 2005.
- [51] E Kreyszig. *Advanced engineering mathematics*. John Wiley & Sons, Inc, 9 edition, 2006.
- [52] V Krishnan. *Probability and Random Processes*. Wiley-Interscience, 2006.
- [53] J Kybic and M Unser. Fast parametric elastic image registration. *Image Processing, IEEE Trans on*, 12(11):1427–1441, 2003.
- [54] X Lai and H Torp. Interpolation methods for time-delay estimation using cross-correlation method for blood velocity measurement. *UFFC, IEEE Trans on*, 46(2):277–290, 1999.
- [55] MJ Ledesma-Carbayo, J Kybic, M Desco, A Santo, M Suhling, P Hunziker, and M Unser. Spatio-temporal nonrigid registration for ultrasound cardiac motion estimation. *Medical Imaging, IEEE Trans on*, 24(9):1113–1126, 2005.
- [56] JS Lim and AV Oppenheim. *Advanced topics in signal processing*. Prentice Hall, 1988.
- [57] T Loupas, JT Powers, and RW Gill. An axial velocity estimator for ultrasound blood flow imaging, based on a full evaluation of the doppler equation by means of a two-dimensional autocorrelation approach. *UFFC, IEEE Trans on*, 42(4):672–688, 1995.
- [58] J Lu, H Ying, Z Sun, M Motanmedi, B Bell, and LC Sheppard. In vitro measurement of speed of sound during coagulate tissue heating. In *Ultrasonics Symposium, IEEE*, pages 1299–1302, 1996.
- [59] MA Lubinski, SY Emelianov, and M O’Donnell. Speckle tracking methods for ultrasonic elasticity imaging using short-time correlation. *Ultrasonics, Ferroelectrics and Frequency Control, IEEE Transactions on*, 46(1):82–96, 1999.

- [60] R Maass-Moreno and N. Sanghvi CA Damianou. Noninvasive temperature estimation in tissue via ultrasound echo-shifts. part ii: in-vitro study. *J Acoust Soc Am.*, 100(4):2522 – 2530, 1996.
- [61] R Maass-Moreno and CA Damianou. Noninvasive temperature estimation in tissue via ultrasound echo-shifts. part i: analytical model. *J Acoust Soc Am.*, 100(4):2514 – 2521, 1996.
- [62] R Maass-Moreno, CA Damianou, and N. Sanghvi. Tissue temperature estimation in-vivo with pulse-echo. In *Ultrasonics Symposium, IEEE*, pages 1225–1229, 1995.
- [63] N Mcdannold. Quantitative mri-based temperature mapping based on the proton resonant frequency shift: Review of validation studies. *Int. J. Hyperthermia*, 21(6):533–546, 2005.
- [64] PM Meaney, KD Paulsen, A Hartov, and RK Crane. Microwave imaging for tissue assessment: initial evaluation in multitarget tissue-equivalent phantoms. *Biomed. Eng., IEEE Trans on*, 43(9):878–890, 1996.
- [65] NR Miller and JC Bamber. Ultrasonic measurement of the temperature distribution due to absorption of diagnostic ultrasound: potential and limitations. In *J. Physics: Conference Series 1*, pages 128–133, 2004.
- [66] JW Mimbs, M O’Donnell, and JG Miller. Changes in ultrasonic attenuation indicative of early myocardial ischemic injury. *Am J Physiol*, 236(2):H340–4, 1979.
- [67] RC Molthen, PM Shankar, and JM Reid. Characterization of ultrasound b-scans using non-rayleigh statistics. *J. Acoust. Soc. Am.*, 89(6):2992–2995, 1991.
- [68] RJ Myerson, WL Straube, EG Moros, BN Emami, HK Lee, CA Perez, and ME Taylor. Simultaneous superficial hyperthermia and external radiotherapy: report of thermal dosimetry and tolerance to treatment. *Journal of Hyperthermia*, 15:251–266, 1999.
- [69] VM Narayanan, PM Shankar, and JM Reid. Non-rayleigh statistics of ultrasonic backscattered signals. *UFFC, IEEE Trans on*, 41(6):845–852, 1994.
- [70] RL Nasoni, T Bowen, MW Bewhirst, HB Roth, and R Premovich. The speed of sound as a function of temperature in mammalian tissue. In *Ultrasonics Symposium, IEEE*, pages 1077–1082, 1980.
- [71] J Ophir. Estimation of the speed of ultrasound propagation in biological tissues: a beam-tracking method. *UFFC, IEEE Trans On*, 33(4):359–368, 1986.

- [72] J Overgaard, D Gonzalez Gonzalez, MCCH Hulshoe, G Arcangeli, O Dahl, and O Mella. Hyperthermia as an adjuvant to radiation therapy of recurrent or metastatic malignant melanoma. a multicentre randomized trial by the european society for hyperthermic oncology. *Journal of Hyperthermia*, 12:3–20, 1996.
- [73] KD Paulsen, MJ Moskowitz, TP Ryan, SE Mitchell, and PJ Hoopes. Initial *in vivo* experience with eit as a thermal estimator during hyperthermia. *Int. J. Hyperthermia*, 12(5):573–591, 1996.
- [74] M Pernot, M Tanter, J Bercoff, KR Waters, and M Fink. Temperature estimation using ultrasonic spatial compound imaging. *UFFC, IEEE Trans on*, 51(5):606–615, 2004.
- [75] T Piboongunon, VA Aalo, C-D Iskander, and GP Efthymoglou. Bivariate generalised gamma distribution with arbitrary fading parameters. *IEE Electronics Letters*, 41(12):49–50, 2005.
- [76] B Rajagopalan, JF Greenleaf, PJ Thomas, SA Johnson, and RC Bahn. Variation of acoustic speed with temperature in various excised human tissues studied by ultrasound computerized tomography. In *Ultrasonic Tissue Characterization II, M Linzer, Ed, National Bureau of Standards*, volume Spec Publ 525, pages 227–233. US Government Printing Office, Washington D.C., 1979.
- [77] R Seip and ES Ebbini. Noninvasive estimation of tissue temperature response to heating fields using diagnostic ultrasound. *Biomed. Eng., IEEE Trans on*, 42(8):828 – 839, 1995.
- [78] R Seip, P VanBaren, CA Cain, and ES Ebbini. Noninvasive real-time multipoint temperature control for ultrasound phased array treatments. *UFFC, IEEE Trans on*, 43(6):1063 – 1073, 1996.
- [79] R Seip, P VanBaren, C Simon, and ES Ebbini. Noninvasive real-time spatio-temporal temperature estimation using diagnostic ultrasound. In *Ultrasonics Symposium, IEEE*, pages 1613 – 1616, 1995.
- [80] PM Shankar. A model for ultrasonic scattering from tissues based on the k distribution. *Phys. Med. Biol.*, 40:1633–1649, 1995.
- [81] PM Shankar. A general statistical model for ultrasonic backscattering from tissues. *UFFC, IEEE Trans on*, 47(3):727–736, 2000.
- [82] PM Shankar. Ultrasonic tissue characterization using a generalized nakagami model. *UFFC, IEEE Trans on*, 48(6):1716–1720, 2001.

- [83] PM Shankar, VA Dumane, JM Reid, V Genis, F Forsberg, CW Piccoli, and BB Goldberg. Classification of ultrasonic b-mode images of breast masses using nakagami distribution. *UFFC, IEEE Trans on*, 48(2):569–580, 2001.
- [84] PM Shankar, JM Reid, CW Piccoli, and BB Goldberg. Use of non-rayleigh statistics for the identification of tumors in ultrasonic b-scans of the breast. *Med. Imag., IEEE Trans on*, 12(4):687–692, 1993.
- [85] RA Sigelmann and JM Reid. Analysis and measurement of ultrasound backscattering from an ensemble of scatterers excited by sine-wave bursts. *J. Acoust Soc Am*, 53:1351–1355, 1973.
- [86] C Simon, P VanBaren, and ES Ebbini. Quantitative analysis and application of non-invasive temperature estimation using diagnostic ultrasound. In *Ultrasound Symposium, IEEE*, pages 1319–1322, 1997.
- [87] C Simon, P VanBaren, and ES Ebbini. Two-dimensional temperature estimation using diagnostic ultrasound. *UFFC, IEEE Trans on*, 45(4):1088 – 1099, 1998.
- [88] MK Simon. *Probability distributions involving Gaussian random variables: A handbook for engineers and scientists*. Kluwer Academic Publishers, 2002.
- [89] M Sonka and JM Fitzpatrick, editors. *Handbook of medical imaging*, volume 2. Spie Press, 2000.
- [90] EW Stacy and GA Mihram. Parameter estimation for a generalized gamma distribution. *Technometrics*, 7(3):349–358, 1965.
- [91] P Stansell, J Wolfram, and B Linfoot. Statistics of wave groups measured in the northern north sea: comparisons between time series and spectral predictions. *Applied Ocean Research*, 24:91–106, 2002.
- [92] WL Straube and RM Arthur. Theoretical estimation of the temperature dependence of backscattered ultrasonic power for noninvasive thermometry. *Ultrasound in Med. and Biol*, 20(9):915–922, 1994.
- [93] Z Sun and H Ying. A multi-gate time-of-flight technique for estimation of temperature distribution in heated tissue: theory and computer simulation. *Ultrasonics*, 37:107–122, 1999.
- [94] S Suprijanto, MW Vogel, FM Vos, HA Vrooman, and AM Vossepoel. Displacement correction scheme for mr-guided interstitial laser therapy. In RE Ellis and TM Peters, editors, *MICCAI(2)*, volume 2879 of *Lecture Notes in Computer Science*, pages 399–407, Montréal, Canada, November 2003. Springer.

- [95] M Tanter, J Bercoff, L Sandrin, and M Fink. Ultrafast compound imaging for 2-d motion vector estimation: application to transient elastography. *UFFC, IEEE Trans on*, 49(10):1363–1374, 2002.
- [96] U Techavipoo, T Varghese, Q Chen, TA Stiles, JA Zagzebski, and GR Frank. Temperature dependence of ultrasonic propagation speed and attenuation in excised canine liver tissue measured using transmitted and reflected pulses. *J Acoust Soc Am*, 115(5):2859–2865, 2004.
- [97] Terason, division of Teratech Corp., Burlington, MA 01803. *Terason ultrasound COM automation and streaming video reference*, 4 edition, July 2006.
- [98] RT Towa, RJ Miller, LA Frizzell, JF Zachary, and WD O’Brien Jr. Attenuation coefficient and propagation speed estimates of rat and pig intercostal tissue as a function of temperature. *UFFC, IEEE Trans on*, 49(10):1411–1420, 2002.
- [99] HL Van Trees. *Detection, estimation, and modulation theory*. Wiley-Interscience, 2001.
- [100] JW Trobaugh. *An image model for ultrasound incorporating surface shape and microstructure and characteristics of the imaging system*. D.sc., Washington University in St. Louis, 2000.
- [101] JW Trobaugh and RM Arthur. A discrete-scatterer model for ultrasonic images of rough surfaces. *UFFC, IEEE Trans on*, 47(6):1520–1529, 2000.
- [102] JW Trobaugh and RM Arthur. A physically-based, probabilistic model for ultrasonic images incorporating shape, microstructure and system characteristics. *UFFC, IEEE Trans on*, 48(6):1594–1605, 2001.
- [103] JW Trobaugh, RM Arthur, WL Straube, and EG Moros. A simulation model for ultrasonic temperature imaging using change in backscattered energy. *Ultrasound in Med.&Biol.*, 34(2):289–298, 2008.
- [104] H Tsuda, M Tanka, T Manabe, H Ikeda, S Negoro, O Ishiko, and K Yamamoto. Phase i study of combined radiation, hyperthermia and intra-arterial carboplatin for local recurrence of cervical cancer. *Annals of Oncology*, 14:298–303, 2003.
- [105] TA Tuthill, RH Sperry, and KJ Parker. Deviations from rayleigh statistics in ultrasonic speckle. *Ultrasonic Imaging*, 10:81–89, 1988.
- [106] PD Tyreus and C Diederich. Two-dimensional acoustic attenuation mapping of high-temperature interstitial ultrasound lesions. *Phys. Med. Biol.*, 49:533–546, 2004.

- [107] J van der Zee. Heating the patient: A promising approach? *Annals of Oncology*, 13:1173–1184, 2002.
- [108] T Varghese, JA Zagzebski, Q Chen, U Techavipoo, G Frank, C Johnson, A Wright, and FT Lee Jr. Ultrasound monitoring of temperature change during radiofrequency ablation: preliminary in-vivo results. *Ultrasound in Med. & Biol.*, 28(3):321–329, 2002.
- [109] RF Wagner, MF Insana, and DG Brown. Statistical properties of radio-frequency and envelope-detected signals with applications to medical ultrasound. *J. Opt. Soc. Am.*, 4(5):910–922, 1987.
- [110] RF Wagner, SW Smith, JM Sandrik, and H Lopez. Statistics of speckle in ultrasound b-scans. *Sonics and Ultrasonics, IEEE Trans. on*, 30(3):156–163, 1983.
- [111] LM Wang and KK Shung. Adaptive pattern correlation for two-dimensional blood flow measurements. *UFFC, IEEE Trans on*, 43(5):881–887, 1996.
- [112] L Weng, JM Reid, PM Shankar, and K Soetanto. Ultrasound speckle analysis based on the k distribution. *J. Acoust. Soc. Am.*, 89(6):2992–2995, 1991.
- [113] AE Worthington, J Trachtenberg, and MD Sherar. Ultrasound properties of human prostate tissue during heating. *Ultrasound in Med & Biol*, 28(10):1311–1318, 2002.
- [114] F Yeung, SF Levinson, D Fu, and KJ Parker. Feature-adaptive motion tracking of ultrasound image sequences using a deformable mesh. *Medical Imaging, IEEE Trans on*, 17:945–956, 1998.

Vita

Yuzheng Guo

Date of Birth March 18, 1971

Place of Birth China

Degrees B.S. Electrical Engineering, August 1992
M.S. Biomedical Engineering, August 1998
M.S. Electrical Engineering, May 2002
Ph.D. Electrical Engineering, December 2009

**Professional
Societies** IEEE

Publications R.M. Arthur, D Basu, Y Guo, J.W. Trobaugh, E. Moros,
(2009). 3D *In Vitro* Estimation of Temperature Using the
Change in Backscattered Ultrasonic Energy *IEEE Trans. on
UFFC, Submitted in June 2009.*

Y. Guo, J.W. Trobaugh, R.M. Arthur (2009). A Framework
for Temperature Imaging using the Change in Backscattered
Ultrasonic Signals. *34nd International Symposium on Ul-
trasonic Imaging and Tissue Characterization, Washington,
D.C., 10-12 June 2009. Ultrasonic Imaging. 31: 74 - 75(ab-
stract), 2009.*

D. Basu, R. M. Arthur, J. W. Trobaugh, Y. Guo, W.L. Straube
(2009). 3D Temperature Imaging using Change in Ultrasonic
Backscattered Energy: Estimation of Temperature during Non-
Uniform Heating. *34nd International Symposium on Ultra-
sonic Imaging and Tissue Characterization, Washington, D.C.,
10-12 June 2009. Ultrasonic Imaging. 31: 75 - 77(abstract),
2009.*

Y. Guo, J.W. Trobaugh and R.M. Arthur(2007). Motion Compensation for Temperature Imaging using the Change in Ultrasonic Backscattered Energy. *Memphis Biomedical Imaging Symposium 2007*. Memphis, Tennessee, 1-2 November 2007.

R.M. Arthur, J.W. Trobaugh, Y. Guo, W.L. Straube, and E.G. Moros (2007). Change in Ultrasonic Backscattered Energy for Temperature Imaging: Factors Affecting Temperature Accuracy and Spatial Resolution. *32nd International Symposium on Ultrasonic Imaging and Tissue Characterization, Washington, D.C., 16 May 2007. Ultrasonic Imaging*. **29**:47 - 48(abstract), 2009.

Y. Guo and P.Y. Woo (2003). Adaptive fuzzy sliding mode control for robotic manipulators. *Proceedings of 42nd IEEE Conference on Decision & Control*. **3**: 2174 - 2179. 2003.

Y. Guo and P.Y. Woo (2003). An adaptive fuzzy sliding mode controller for robotic manipulators, *Systems, Man and Cybernetics, Part A, IEEE Transactions on*. **33**(2): 149-159.

Y. Guo and P.Y. Woo (2000). Mobile Robot Control by Fuzzy Method. *Proceedings of ANNIE 2000*. **3**: 2174 - 2179. Nov.2000.

December 2009

Framework for Temperature Imaging with CBE, Guo, Ph.D. 2009